HIGHLY INTEGRATED SENSORS BASED ON MICROSTRUCTURED OPTICAL FIBERS

ZHENG YU

School of Electrical & Electronic Engineering

A thesis submitted to the Nanyang Technological University
in partial fulfillment of the requirement for the degree of
Doctor of Philosophy

2020

Statement of Originality

I hereby certify that the work embodied in this thesis is the result of original research, is free of plagiarised materials, and has not been submitted for a higher degree to any other University or Institution.

23-07-2020
. . . .
Date

. . . .
Zheng Yu

Supervisor Declaration Statement

I have reviewed the content and presentation style of this thesis and declare it is free of plagiarism and of sufficient grammatical clarity to be examined. To the best of my knowledge, the research and writing are those of the candidate except as acknowledged in the Author Attribution Statement. I confirm that the investigations were conducted in accord with the ethics policies and integrity standards of Nanyang Technological University and that the research data are presented honestly and without prejudice.

23-07-2020
. . . .
Date

YuLuo
. . . .
Luo Yu

Authorship Attribution Statement

This thesis contains material from 4 paper(s) published in the following peer-reviewed journal(s) / from papers accepted at conferences in which I am listed as an author.

Chapter 3 is published as Y. Zheng, P. P. Shum, S. Liu, B. Li, Y. Xiang, Y. Luo, Y. Zhang, W. Ni, Z. Wu, X. Q. Dinh, S. Zeng, J. Auguste and G. Humbert. "Experimental and numerical investigation on hollow core photonic crystal fiber based bending sensor," *Opt. Express* 27(21): 30629-30638 (2019). DOI: 10.1364/OE.27.030629.

The contributions of the co-authors are as follows:

- Prof. Shum and Dr. Humbert provided the initial project direction and edited the manuscript drafts.
- I prepared the manuscript drafts. The manuscript was revised by Dr. Humbert, Dr. Luo, Prof. Zhang, Dr. Zeng and Prof. Dinh.
- I designed the optical fiber. I fabricated the optical fiber with Dr. Humbert and Dr. Auguste.
- I co-designed the experiments with Prof. Liu and performed all the laboratory work. I also did the simulation and analyzed the data.
- Dr. Xiang, Dr. Ni, Dr. Wu and Mr. Li provided suggestions for the manuscript preparation.

Chapter 4 is published as Y. Zheng, P. P. Shum, S. Liu, B. Li, J. Auguste, G. Humbert and Y. Luo. "Strain Sensitivity Enhancement Based on Periodic Deformation in Hollow Core Fiber," Opt. Lett. 45(14): 3997-4000 (2020). DOI: 10.1364/OL.396638.

The contributions of the co-authors are as follows:

- I provided the initial idea and experiment scheme. Prof. Shum and Prof. Liu provided suggestions for the project direction.
- I prepared the manuscript drafts. The manuscript was revised by Prof. Luo, Dr. Humbert, Prof. Liu and Mr. Li.
- I designed the optical fiber. I fabricated the optical fiber with Dr. Humbert and Dr. Auguste.
- I performed all the laboratory work, did the simulation and analyzed the data.

Chapter 5 is published as Y. Zheng, P. P. Shum, Y. Luo, Y. Zhang, W. Ni, G. Wang, Z. Wu, X. Q. Dinh, J. Auguste and G. Humbert. "High-resolution, large-dynamic-range multimode interferometer sensor based on a suspended-core microstructured optical fiber," Opt. Lett. 45(4): 1017-1020 (2020). DOI: 10.1364/OL.386296.

The contributions of the co-authors are as follows:

- Prof. Shum and Dr. Luo suggested the initial project direction and edited the manuscript drafts.
- I prepared the manuscript drafts. The manuscript was revised by Dr. Humbert, Prof. Wang, Dr. Wu, Dr. Ni and Prof. Dinh.
- I designed the optical fiber. I fabricated the optical fiber with Dr. Humbert and Dr. Auguste.
- I co-designed the experiments with Dr. Luo and performed all the laboratory work. I also did the simulation and analyzed the data.
- Prof. Zhang provided suggestions for the manuscript preparation.

And

Y. Zheng, P. P. Shum, Y. Luo, Y. Zhang, Z. Wu, J. Auguste and G. Humbert. "Suspended-core fiber based Sagnac interferometer device and sensing applications," In CLEO: Science and Innovations (JW2A.108), 2019. DOI: 10.1364/CLEO_AT.2019.JW2A.108.

The contributions of the co-authors are as follows:

- Prof. Shum and Prof. Zhang suggested the initial project direction and edited the manuscript drafts.
- I prepared the manuscript drafts. The manuscript was revised by Dr. Humbert, Dr. Wu, and Dr. Luo.
- I designed the optical fiber. I fabricated the optical fiber with Dr. Humbert and Dr. Auguste.
- I co-designed the experiments with Prof. Zhang and performed all the laboratory work. I also analyzed the data.

23-07-2020
. . . .
Date

. . . .
Zheng Yu

Acknowledgement

During my Ph.D. journey, I received so much kind help and support from my supervisors, collaborators, colleagues and beloved ones. I would like to express my deepest appreciation to them.

First and foremost, I would like to express my sincere gratitude to my supervisors, Prof. Shum Ping, Prof. Luo Yu and Dr. Georges Humbert. Prof. Shum created the opportunity for my Ph.D. study at Nanyang Technological University and provided me an excellent research platform and invaluable collaborations with other top researchers throughout the years. Besides, he always shares his valuable experiences which are helpful to my career and life. Prof. Luo inspired me with innovative research ideas. The professional attitude and research skills he taught will benefit me in the future work. Dr. Humbert took me into the field of microstructured optical fiber, offered me a valuable chance to exchange and study in Xlim Institute in France and guided me with experimental and analytical skills.

I would like to extend my sincere gratefulness to Dr. Wu Zhifang, Dr. Luo Yiyang, Prof. Liu Shuhui and Prof. Zhang Yanan. They provided lots of guidance and suggestions for my study and unreservedly shared their extensive knowledge and research experiences on optical fiber sensors.

Besides, I would like to thank Prof. Wei Lei and Prof. Liu Linbo for the great support and generosity in sharing facilities. Thanks to Dr. Dinh Xuan Quyen for his resources and suggestions.

My thanks also go to my wonderful colleagues Dr. Li Kaiwei, Dr. Xu Zhilin, Dr. Zhang Nan, Dr. Zhang Hailiang, Dr. Zhang Mengying, Dr. Wu Tingting, Dr. Ni Wenjun, Teo Huei, Yang Jiao, Wang Zhe, Wang Zhixun, Qi Miao, Wan Ying, Wang Chenlu, Li Baocheng and Chen Shi. They provided me a lot of support to my research work and enriched my life experience.

I would like to thank our lab staffs Ms. Wu Junying, Ms. Yang Xin and Mr. Seah You Gin for their support for the administrative issues.

Last but not least, I wish to express special thanks to my family who always support my decisions and share important moments. Their love and concern encourages me to cope with any challenge.

Table of Contents

Abstract

Microstructured optical fibers (MOFs) have been widely studied in terms of the fabrications, properties and applications in the past few years, since a silica fiber with a complex holey cladding structure was firstly fabricated in 1996. Due to the inherent properties such as immunity to electromagnetic interference, light weight, versatile designs and diverse optical and mechanical performances, MOFs possess an enormous potential in the field of sensing applications. In this thesis, we investigate several approaches to improve the performance of fiber sensors based on the proper design and fabrication of MOFs and post-processing techniques.

Firstly, we design and fabricate a novel hollow core microstructured optical fiber (HCMOF) by stack-and-draw process. The HCMOF consists of a large hollow core surrounded by twelve crown-like air holes. Due to the special structure, the HCMOF allows the multiple-mode propagation in the hollow fiber core. In addition, it is easy to obtain a robust integration with single mode fibers (SMFs) since the diameter of the fiber and the thickness of the silica cladding are around 125 μm and 30 μm, respectively.

Secondly, we develop an in-line Mach–Zehnder interferometer (MZI) sensor for bending measurement based on the specially designed HCMOF. Optical fiber bending sensors have been broadly applied in the fields of mechanical engineering and health monitoring. Among all specifications of fiber bending sensors, bending sensitivity is a critical performance indicator. Hence, we theoretically and experimentally investigate the relationship between the bending sensitivity and the hollow core size, and prove that the bending sensitivity is positively dependent on the hollow core size. Specifically, the bending sensitivity of our sensor at small bending angle is improved 10 times by increasing the hollow core size compared with the sensor consisting of a small-size hollow core.

Thirdly, we explore a method to enhance the strain sensitivity of the in-line MZI sensor by fabricating periodical structures on the specially designed HCMOF. Introducing periodical structures via electric arc discharge alters the power ratio of guided modes in the hollow core. External tension is further to change the power ratio of guided modes, which leads to the variation of the extinction ratio in the transmission spectrum.

Fourthly, the performance of optical fiber sensors is generally limited by either their dynamic range or resolution, which is a trade-off existing in almost all kinds of sensors. We theoretically and experimentally demonstrate a multimode interferometer sensor based on a suspended core microstructured optical fiber (SCMOF) to improve the dynamic range and resolution simultaneously. The multimode interferometer sensor is fabricated only by splicing a section of SCMOF between two segments of SMFs with central alignment. The transmission spectrum of the SMF–SCMOF–SMF structure features dense fringes modulated by a lower envelope, which is induced by the multimode interference. Strain sensing is applied to validate the characteristics of the sensor.

Based on the researches we conducted, it reveals that our designed and fabricated MOFs possess the potential in developing MZI-based highly integrated and high-performance sensors for physical parameter measurements. Further applications in the fields of gas sensing and biochemical sensing will be carried out in the near future.

List of Figures

List of Tables

Abbreviations

ANN	Artificial neural network
ARROW	Anti-resonant reflecting optical waveguide
ERI	Effective refractive index
FBG	Fiber Bragg grating
FFT	Fast Fourier Transform
FPI	Fabry-Pérot interferometer
FSR	Free spectral range
HCMOF	Hollow core microstructured optical fiber
HCPBF	Hollow core photonic bandgap fiber
Hi-Bi	Highly birefringent
LPFG	Long period fiber grating
MOF	Microstructured optical fiber
MZI	Mach-Zehnder interferometer
OSA	Optical Spectrum Analyzer
PCF	Photonic crystal fiber
SCMOF	Suspended core microstructured optical fiber
SEM	Scanning electron microscope
SI	Sagnac interferometer
SMF	Single mode fiber
WGM	Whispering gallery mode

Chapter 1 Introduction

The first chapter presents the development of optical fibers, MOFs and MOF based sensors. Then, the motivation and objectives of the thesis are stated. After that, the major contributions of this thesis are introduced. In the last section, the thesis organization is clarified.

1.1 Background

In the early 1840s, Daniel Colladon and Jacques Babinet found that light could be confined and propagated by reflection [1]. Then in 1854, John Tyndall demonstrated that light could be propagated in a downward-curving water stream (a "light pipe") in his public lectures [2]. Tyndall also introduced the principle of total internal reflection in a book in 1870, which built the theoretical foundation of optical fiber [3]. In the late 19th century, glass rods were applied to guide light for illuminating body cavities. The next milestone appeared in 1953. Dutch scientist Abraham van Heel and British scientist Harold Hopkins and Narinder Kapany almost simultaneously demonstrated an image transmission with bundles of optical fibers for medical applications [4, 5]. In 1956, the first glass-clad fiber was fabricated by Lawrence Curtiss, an undergraduate student at the University of Michigan. In previous optical fibers, the low-index cladding material was air, oils or waxes. Then, Elias Snitzer theoretically proposed that light could propagate in a kind of SMF with only one waveguide mode in 1961[6]. However, at that time, the optical fiber had a loss of around 1 dB/m. Although the idea of optical communication has again been paid attention with the invention of laser in 1960, optical fiber based communication was limited by the large loss. In 1965, Charles Kao theoretically demonstrated that optical fibers could possess a low loss less than 20 dB/km by removing impurities in materials and also pointed out that silica glass with high purity was an excellent material for fabricating optical fibers [7]. This discovery was identified as the footstone of the optical fiber development. Charles Kao was awarded the Nobel Prize in Physics in 2009 due to his contribution to optical fiber communication. Then, Robert Maurer, Donald Keck and Peter Schultz from Corning experimentally fabricated the first optical fiber with the loss less than 20 dB/km in 1970. A few years later, due to the development of optical fiber fabrication technology, the loss of optical fiber has been reduced to 0.2 dB/km for light with a wavelength of 1.55 μm in 1979 [8]. In the following decades, optical fibers promoted the realization of the information revolution. Besides, optical fibers also had widespread applications in other fields, such as optical fiber lasers and optical fiber sensors.

The basic optical fiber structure is composed of a core, a cladding and a polymer coating, as illustrated in Fig. 1.1. The refractive index of the doped silica core is slightly higher (typically less than 1%) than that of the pure silica cladding so that the light can be confined in the core based on the total internal reflection, as illustrated in Fig. 1.2. The function of polymer coating is to mechanically protect the fiber core and cladding. As an optical waveguide, optical fibers support the propagation of one or more transverse modes in the core. For each mode, there is a cut-off value of V (normalized frequency) below which the mode cannot be guided [9]:

$$V = \frac{2\pi a}{\lambda} \sqrt{n_{core}^2 - n_{cladding}^2} \tag{1.1}$$

where λ is the wavelength of light, a is the radius of fiber core, and n_{core} and $n_{cladding}$ are the refractive index of the fiber core and cladding, respectively. Once the fiber is fabricated, the V number will be fixed. When V is smaller than 2.405, the fiber only supports one mode, which is called SMF.

Figure 1.1 Schematic of a basic optical fiber structure.

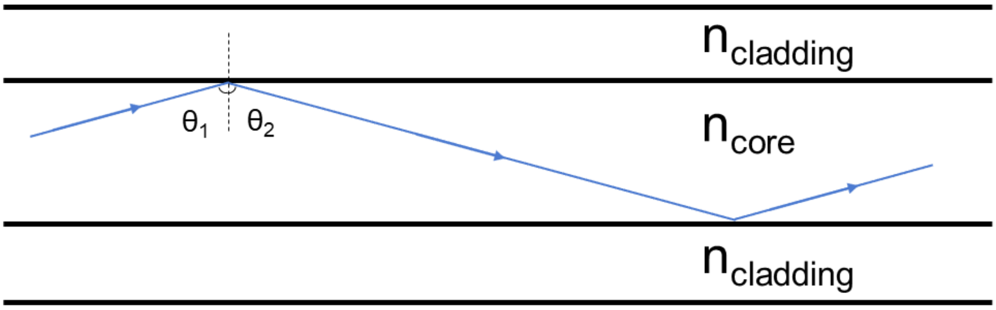

Figure 1.2 Schematic of light propagation in the optical fiber based on the total internal reflection.

In the early 1970s, in order to realize long-distance optical data transmission based on the optical fiber, researchers developed a kind of microstructured fiber for decreasing the transmission loss [10]. The fiber core was suspended in air by using thin glass struts. However, research interest in microstructured fibers was soon overtaken by the successful fabrication of low-loss solid fibers. Until 1996, MOFs regained attention with the first fabrication of a silica fiber that could demonstrate optical guidance with a complex holey cladding structure [11]. Since then, MOFs were widely studied due to many characteristics and advantages obtained from modifying the cross-sectional structure of MOFs. Until now, a variety of MOFs have been proposed and fabricated, including photonic crystal fiber (PCF), SCMOF, side-channel MOF and HCMOF etc. Typically, these fibers can guide light through three mechanisms, index-guiding mechanism, photonic bandgap mechanism and anti-resonant reflecting guidance mechanism [12]. The representative structure of index-guiding MOFs is composed of a solid core and a microstructured cladding, as shown in Fig. 1.3 (a). Due to the existence of air holes in the cladding, the effective refractive index (ERI) of microstructured cladding is smaller than that of fiber core. Hence, light is confined in fiber core based on the effect of total internal reflection. Photonic bandgap MOFs are also called as PCFs consisting of a hollow core and surrounding microstructured cladding, as illustrated in Fig. 1.3 (b). Due to photonic bandgap effect in the cladding area, the hollow core can guide light along the fiber in a limited range of wavelengths. The photonic bandgap effect can be explained as: periodically distributed air holes form a 2D photonic crystal structure and can be treated as multilayer mirrors. Certain wavelengths of light are reflected by these mirrors, and strongly confined in the hollow core (a defect in the photonic crystal). In 1986, anti-resonant reflecting optical waveguides was firstly proposed in a SiO_2-Si multilayer structure [13]. Then the origination of anti-resonant fiber was from the Kagome-type broadband hollow core fiber in 2002 [14]. In the past ten years, Anti-resonant MOF has been widely studied and developed. Unlike the Photonic bandgap MOFs that required a periodic cladding material, the anti-resonant MOFs had a simpler structure. The typical structure was shown in Fig. 1.3 (c). Since the refractive index of the hollow core was less than the cladding, the guiding modes would leak out of the core and radiate into the cladding. The cladding acted as a multilayer Fabry-Pérot etalon, where the light wavelengths met the anti-resonant condition would be reflected back to the hollow core by the Fabry-Pérot etalon and the light wavelengths matched the resonant condition of the Fabry-Pérot etalon would transmit through the etalon and leak out of the cladding.

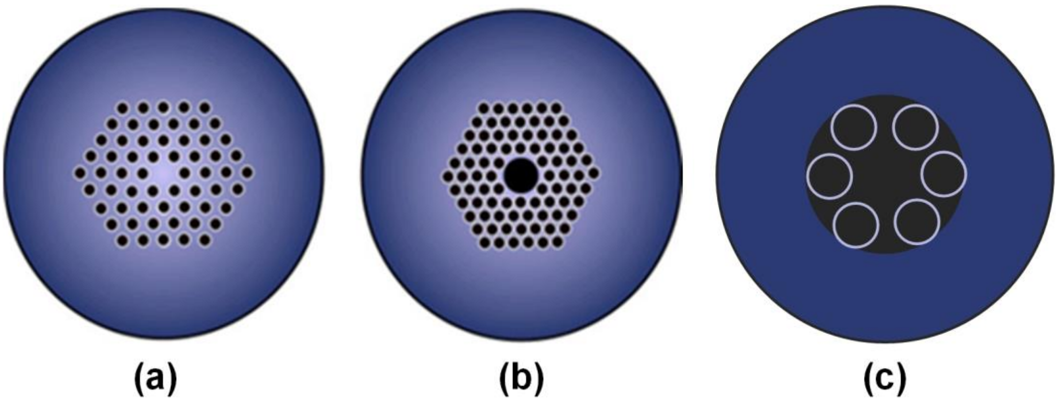

Figure 1.3 Schematic diagram of three main classes of MOFs, (a) index-guiding MOF; (b) photonic bandgap MOF; (c) anti-resonant MOF [12].

MOFs have been widely applied in many fields. One of the applications is fiber lasers. MOFs with a large doped core can provide a high-power generation with a high damage threshold, a low nonlinear effect, and a broadband single mode laser output. On the other hand, when MOFs with a high nonlinearity are applied to construct fiber lasers, a high gain efficiency can be achieved. The second one is high-power transmission [15-18]. Some passive MOFs with a large mode area dramatically improve the performance of high-power transmission based on optical fibers. The third one is optical sensors. Optical fibers have a number of advantages in sensing applications, such as compact size, high stability, easy integration, repeatability, remote sensing and electromagnetic immunity. Besides, MOFs possess more advantages due to the convenience of modifying their optical and mechanical properties compared with solid core fibers.

MOFs are fabricated by the process of drawing preforms into fibers based on the use of fiber tower. Several methods can be applied to prepare preforms, such as stack-and-draw method, extrusion method, drilling method and injection moulding method [19]. The most used method is the stack-and-draw method. Basically, the first step of stack-and-draw method is to draw silica tubes into capillaries with designed sizes. Then these capillaries are stacked layer-by-layer based on the fiber design. After that, the preform is fabricated by placing and fixing the stack into a silica tube. Finally, the preform is drawn into the MOF by the fiber tower. A commonly accepted classification of MOF-based sensors includes two main classes: grating-based MOF sensors and interferometer-based MOF sensors. Grating-based MOF sensors contain the configurations of fiber Bragg grating (FBG), long period fiber grating (LPFG) or tilted fiber Bragg grating (TFBG). Interferometer-based MOF sensors are fabricated by building several famous interferometers based on MOFs, such as Mach-Zehnder interferometer (MZI), Fabry-Pérot interferometer (FPI), Sagnac interferometer (SI) and Michelson interferometer (MI).

MOF-based sensors have been developed in many schemes to measure physical parameters, biomedical signal and chemical signal. The measurement of physical parameters, including temperature, strain, bending, torsion, pressure and vibration, has large application markets, for example oil industry, mechanical engineering, earthquake monitoring and structural health monitoring on aircrafts, skyscrapers, bridges and railways. Compared with conventional solid fibers, MOFs can provide more flexibility in manipulating sensing properties in the field of physical sensing. The mediums of biomedical and chemical sensing are mainly liquid and gas. Due to the existence of air holes, MOFs possess an inherent capability of exploiting the interaction of light with liquid or gas. Meanwhile, the fiber geometry naturally provides an unprecedented length for the interaction in a compact way. Typically, the interaction between light and analytes can be introduced by two methods. One is to inject analytes into the hollow core of some MOFs, where the guided light can interact with analytes directly. The other one is to infiltrate analytes into air holes in the cladding of MOFs, where the principle of sensing is based on evanescent field effects.

1.2 Motivation and Objectives

HCMOF guides light by confining optical modes in the hollow core. The fraction of optical power in the hollow core can be higher than 95% [20]. Based on the principle of light propagation, HCMOFs can be classified into two types: photonic bandgap HCMOF and anti-resonant HCMOF. The photonic bandgap HCMOFs contain a periodic and multilayer air-silica cladding, which is a full photonic crystal structure. Light is confined in the hollow core by the photonic bandgap with a low transmission loss [21]. However, the fabrication process of multilayer air-silica structure is complicated. The anti-resonant HCMOFs only own a few layers of air-silica cladding, which confines light in the hollow core by the anti-resonant reflecting optical waveguide (ARROW) model. Meanwhile, the anti-resonant HCMOF reported by Jasion *et al.* in 2020 has an ultralow transmission loss of 0.28 dB/km [22]. Hence, anti-resonant HCMOFs are better candidates as optical fiber sensors due to the advantages of easy fabrication, low cost and low attenuation. Furthermore, compared with solid core fibers, HCMOFs possess the advantage of low temperature response thanks to the low thermo-optic coefficient of the air core, which can result in HCMOF-based sensors with a low temperature cross-sensitivity, such as bending sensors or strain sensors. An HCMOF-based bending sensor has been demonstrated by inserting a piece of HCMOF into two segments of SMFs [23]. An in-line MZI was developed based on the interference between the fundamental mode and the TE_{01} mode. The TE_{01} mode was excited by a lateral offset splicing between the HCMOF and SMFs. However, relations of the bending sensitivity and the hollow core size, and the bending sensitivity and the interference modes were rarely investigated. Moreover, due to the low elasto-optical coefficient of silica, the in-line MZIs based on HCMOFs generally have a low strain sensitivity. The scheme of an HCMOF based highly sensitive strain sensor has not been developed.

Besides the sensitivity, dynamic range and resolution are also critical parameters of optical fiber sensors. Dynamic range refers to the range of values that can be measured by a sensor. Resolution is the smallest change that a sensor can detect. Nevertheless, the performance of optical fiber sensors is limited by either their dynamic range or resolution, which is a trade-off existing in almost all kinds of sensors. An optical fiber thermometer with double cascaded cavities, one thin (10 µm) and one thick (200 µm), offers a solution to solve this problem [24]. The thin cavity provides the large dynamic range, and the thick cavity defines the high resolution. However, the fabrication of ultra-thin cavities is complex. More simplified structures should be further investigated.

In this thesis, we aim to investigate several approaches to improve the performance of fiber sensors based on the proper design and fabrication of MOFs and post-processing techniques. The main objectives of our work are:

1. To develop a bending sensor based on our designed and fabricated HCMOF for investigating the relations of the bending sensitivity and the hollow core size, and the bending sensitivity and the interference modes.
2. To explore a post-processing technique on our designed and fabricated HCMOF for enhancing the strain sensitivity of the in-line MZI sensor.
3. To demonstrate a multimode interferometer sensor based on our designed and fabricated SCMOF for improving the dynamic range and resolution of the sensor simultaneously.

1.3 Major Contributions

The major contributions of this thesis include:

1. *Develop a new HCMOF for improving the performance of in-line fiber sensor platforms.* The design and fabrication of an HCMOF with a large and approximately circular hollow core surrounded by 12 air holes are demonstrated. The fiber is fabricated by the stack-and-draw process with pure silica tubes. Thanks to the approximately circular core, the fiber enables the propagation of multiple guided modes in the core, which is an inherent platform for developing an in-line MZI.
2. *Explore the sensing performance of the HCMOF as a bending sensor.* In this work, firstly, relations of the bending sensitivity and the hollow core size, and

the bending sensitivity and the interference modes are simulated. Then, experimentally, a bending sensor is fabricated by sandwiching our designed and fabricated HCMOF into two segments of SMFs with central alignment. To validate the bending sensitivity improvement, the transmission spectra of the sensor are measured with the bending angle variation from -14° to 14°. Compared with previous work, the bending sensitivity of our sensor is improved by 10 times, which proves that the bending sensitivity of HCMOF is positively dependent on the hollow core size.

3. *Demonstrate a method to improve the strain sensitivity of the HCMOF-based sensor*. An MZI-based optical fiber sensor is developed by splicing our HCMOF into two sections of SMFs. However, due to the small elasto-optical coefficient of silica, the MZI-based sensor possesses a low strain sensitivity. An approach is demonstrated to enhance the strain sensitivity of the sensor by fabricating periodical deformations on the HCMOF. A theoretical model is built to explain the principle of the strain sensitivity improvement. Experimentally, the strain response is obtained from 0-1000 $\mu\varepsilon$ with a 5 times strain sensitivity enhancement compared with the sensor based on the identical HCMOF without deformation.
4. *Develop an in-line multimode interferometer based on an SCMOF with a large dynamic range and a high resolution.* Firstly, an SCMOF with a triangular core surrounded by three fan-shaped air holes is designed and fabricated by us. The multimode interferometer is developed only by sandwiching the SCMOF into two segments of SMFs with central alignment. The transmission spectra of the SMF-SCMOF-SMF structure are theoretically and experimentally investigated, which presents the characteristic of dense fringes modulated by a lower envelope. The lower envelope results in the large dynamic range, while the dense fringes lead to the high resolution. The multimode interferometer provides a scheme to solve the trade-off between the dynamic range and resolution in almost all kinds of sensors.

1.4 Thesis organization

This thesis consists of 6 chapters:

Chapter 1 presents the development of optical fibers, MOFs and MOF-based sensors, declares the motivation and objectives of our project, presents the main contributions of our works and outlines the thesis organization.

Chapter 2 explains the sensing principles of MOF-based sensors associated with the schemes including FBG, LPFG, FPI, SI and MZI. The state-of-the-art development of these MOF-based sensors has also been reviewed.

Chapter 3 starts with the design of our HCMOF and fabrication process, then numerically analyzes the relation of the bending sensitivity and the hollow core size, and the bending sensitivity and the interference modes. The bending performance and thermal response of our HCMOF are experimentally demonstrated.

Chapter 4 experimentally and theoretically demonstrates an approach to enhance the strain sensitivity of HCMOF-based MZI through constructing periodical deformations. The characterization of the deformations is presented.

Chapter 5 constructs a high-resolution, large-dynamic-range multimode interferometer based on our SCMOF. The fabrication method and feature of the SCMOF are introduced. The strain response of the sensor is investigated for validating the large dynamic range and the high resolution of the interferometer.

Chapter 6 concludes the thesis and presents future research plans.

Chapter 2 Literature review

MOFs have widespread applications in the field of optical sensors. The sensing units of MOF-based sensors include FBG, LPFG, FPI, SI, and MZI. This review chapter will present the working principles of these sensing units and the applications of these MOF-based sensors.

2.1 FBG sensors based on MOFs

An FBG is a series of periodic reflectors distributed in the fiber core. These reflectors are generated by altering periodically the refractive index of fiber core. The function of the reflectors is a wavelength-specific dielectric mirror, which can reflect certain wavelengths of light. In 1978, the Bragg grating was fabricated in fiber for the first time by Ken Hill [25]. A visible laser launched into the fiber core was used to fabricate a periodic structure in an SMF. In 1989, a more flexible technique, transverse holographic inscription method, was developed by Gerald Meltz [26]. This method utilized a phase mask to generate an interference pattern of ultraviolet laser from the side of the fiber for inscribing a periodic structure into the fiber, as shown in Fig. 2.1. This technique is still in use today for the FBG fabrication. The use of ultraviolet laser is due to the photosensitivity of Ge-doped fiber core to ultraviolet light.

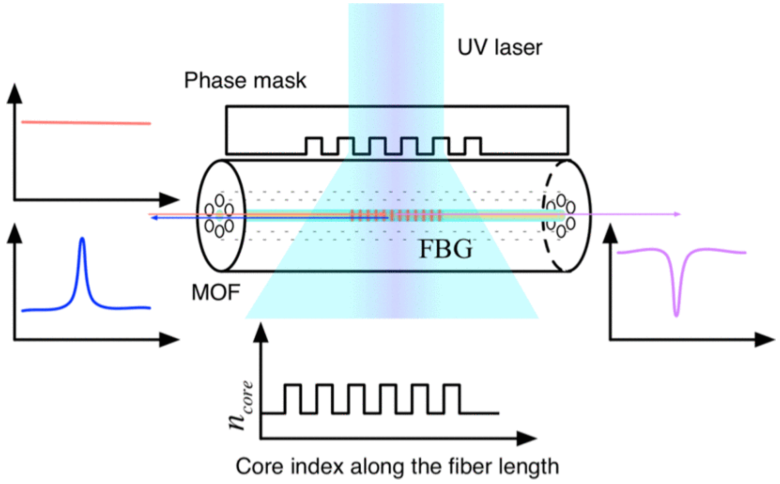

Figure 2.1 Schematic of phase mask technique for FBG inscription [27].

2.1.1 Operating principles of FBG sensors

The fundamental working principle of an FBG is Fresnel reflection, where light may both reflect and refract at the interface of media with different refractive indices. In an FBG, the relation of an incident mode and its reflected mode can be expressed as the following equation [28]:

$$\beta_2 = \beta_1 + m\frac{2\pi}{\Lambda} \tag{2.1}$$

where β_2 and β_1 are propagation constants of the reflected mode and the incident mode, respectively, m is the diffraction order, and Λ is the grating period. Since $\beta = 2\pi n_{eff}/\lambda$, where n_{eff} is the ERI of the guided mode and λ is the wavelength, and the first-order diffraction ($m = -1$) generally dominates in an FBG, the central wavelength of the reflected light in an FBG is:

$$\lambda = (n_{eff1} + n_{eff2})\Lambda. \tag{2.2}$$

When the incident mode is identical with the reflected mode, the central wavelength can be further calculated as:

$$\lambda_B = 2n_{eff}\Lambda \tag{2.3}$$

The Bragg reflection wavelength is determined by the ERI of guided mode and the grating period, which indicates that FBG can be used for the sensing applications since the ERI and the grating period are dependent on external parameters, such as strain, temperature, and bending. When an axial strain ε is applied to a segment of fiber inscribed with an FBG, the length of fiber l, the period of FBG Λ, and the ERI of guided mode will be varied. Since the axial strain is isotropic and homogeneous along the fiber, the relative change of grating period is same as that of the whole fiber. Hence, the axial strain $\varepsilon = \Delta l/l = \Delta\Lambda/\Lambda$. The functional dependence of the Bragg reflection wavelength on the axial strain ε can be calculated as [29]:

$$\frac{d\lambda_B}{d\varepsilon} = 2\frac{d}{d\varepsilon}\left(n_{eff}\Lambda\right) = 2\Lambda\frac{dn_{eff}}{d\varepsilon} + 2n_{eff}\frac{d\Lambda}{d\varepsilon} \tag{2.4}$$

$$\frac{1}{\lambda_B}\frac{d\lambda_B}{d\varepsilon} = \frac{1}{2n_{eff}\Lambda}\left(2\Lambda\frac{dn_{eff}}{d\varepsilon} + 2n_{eff}\frac{d\Lambda}{d\varepsilon}\right) = \frac{1}{n_{eff}}\frac{dn_{eff}}{d\varepsilon} + \frac{1}{\Lambda}\frac{d\Lambda}{d\varepsilon} \tag{2.5}$$

After the axial strain ε is applied to the fiber, the refractive index change of the fiber core can be obtained as [30-32]:

$$\Delta n_{co} = -\frac{n_{co}^3}{2}[(1-\nu)p_{12} - \nu p_{11}]\varepsilon = -p_\varepsilon n_{co}\varepsilon \tag{2.6}$$

where n_{co} is the original refractive index of the fiber core, ν is the Poisson ratio of the fiber core, p_{11} and p_{12} are the Pockel's coefficients, $p_\varepsilon = n_{co}^2[(1-\nu)p_{12} - \nu p_{11}]/2$ is the effective strain-optic coefficient. The ERI change of guided mode can be similarly calculated by:

$$\Delta n_{eff} = -p_\varepsilon n_{eff}\varepsilon. \tag{2.7}$$

Besides, the change of the grating period can be expressed by:

$$\Delta\Lambda = \Lambda\varepsilon. \tag{2.8}$$

Substituting Eq. (2.7) and Eq. (2.8) into Eq. (2.5), the shift of Bragg reflection wavelength induced by an axial strain will be:

$$\Delta\lambda_B = \lambda_B(1 - p_\varepsilon)\varepsilon \tag{2.9}$$

For temperature change, the Eq. (2.5) can be rewritten as:

$$\frac{1}{\lambda_B}\frac{d\lambda_B}{dT} = \frac{1}{n_{eff}}\frac{dn_{eff}}{dT} + \frac{1}{\Lambda}\frac{d\Lambda}{dT} = \alpha_n + \alpha_\Lambda \tag{2.10}$$

where α_n and α_Λ are the thermo-optic coefficient and the thermal expansion coefficient of the fiber core, respectively. The shift of Bragg reflection wavelength induced by a temperature variation can be further obtained as [33]:

$$\Delta\lambda_B = \lambda_B(\alpha_n + \alpha_\Lambda)\Delta T. \tag{2.11}$$

From Table 2.1, for a silica-based fiber, the thermo-optic coefficient α_n (~8.86×10^{-6} /°C) is one order of magnitude larger than the thermal expansion coefficient α_Λ (~0.55×10^{-6} /°C) which indicates that the thermo-optic effect is dominant.

When a fiber is bent, the outer side of the bent fiber will be stretched and the inner side will be compressed, which leads to the refractive index change of fiber material. However, for an FBG in the center of fiber, the refractive index changes from the stretched side and compressed side are offset by each other. Hence, the FBG located at the fiber center is almost insensitive to bending. Nevertheless, some bending sensors were demonstrated by inscribing FBGs into eccentric cores [34-36]. The shift of Bragg reflection wavelength with a curvature in the eccentric-core fiber can be calculated as:

$$\Delta\lambda_B = \lambda_B(1 - p_\varepsilon)dC \tag{2.12}$$

where *d* is the distance from the eccentric core to the neutral plane, *C* is the bending curvature.

Table 2.1 Physical parameters of fused silica [29, 37, 38]

Parameter	**Value**	**Units**
Density	2.2×10^6	kg/m^3
Melting point	1830	°C
Softening point	1600	°C
Annealing point	1120	°C
Maximum continuous service temperature	950	°C
Maximum transient service temperature	1200	°C
Specific heat capacity	703	J·kg^{-1}K^{-1}
Thermal expansion coefficient	0.55×10^{-6}	°C^{-1}
dn/dT	1.28×10^{-5}	°C^{-1}
Thermal conductivity	1.38	W·m^{-1}K^{-1}
Tensile strength	48.3	MPa
Compressive strength	1150	MPa
Poisson's ratio	0.17	
Modulus of elasticity (Young's modulus, 25 °C)	73	GPa
Permittivity (1 MHz, 25 °C)	3.8	
Resistivity	$>10^{18}$	Ω·m
Dielectric strength (20 °C)	$14\text{-}40 \times 10^6$	V·m^{-1}

2.1.2 Applications of FBG sensors based on MOFs

Based on the fabrication process of FBGs in MOFs, we divided FBGs into two types, photo-induced FBGs and physical deformation-induced FBGs, to introduce the sensing applications of FBGs in MOFs. FBGs could be inscribed into MOFs consisting of a Ge-doped solid core or other doping based on the same phase mask technique used for conventional SMFs. In 1999, Eggleton *et al.* demonstrated the first fabrication of FBG in an MOF with a Ge-doped solid core [39]. The FBG was inscribed via a phase mask with a 242-nm laser. Martelli *et al.* wrote an FBG into an MOF with an Er-doped solid core by utilizing an ArF laser (193 nm) and a phase mask [40]. Due to the existence of two guided modes in the fiber core, two distinct Bragg grating peaks were observed. The response of the FBG to strain and temperature was investigated. Distinct strain response and similar temperature sensitivity of two Bragg peaks resulted in the application of distinguishing strain and temperature. Frazão *et al.* developed a sensor by inscribing an FBG into a highly birefringent (Hi-Bi) MOF and a standard SMF, respectively, and then connecting them together [41]. Since the strain sensitivity and temperature sensitivity of the FBG in Hi-Bi MOF were different with that of the FBG in SMF, the application of simultaneous measurement of strain and temperature was realized with resolutions of ±10.7 με and ±1.5 °C and dynamic ranges of 2000 με and 1000 °C, respectively.

The refractive index measurement based on FBGs in MOFs has also been demonstrated, for example, Phan Huy *et al.* wrote an FBG into a six-hole MOF with a Ge-doped core to develop a refractive index sensor [42]. Calibrated oils were inserted into six holes for investigating the refractive index response. The refractive index of the cladding increased with the insertion of calibrated oils, which led to the increase of the ERI of guided mode. Hence, the Bragg wavelength would shift to a longer wavelength when oils reached the FBG. The resolution was 4×10^{-3} RIU for the refractive index close to 1.33. The other FBG based refractive index sensor in a SCMOF has also been demonstrated by Phan Huy *et al.* [43]. Since the SCMOF had a smaller core (9 μm^2) compared with the core of the six-hole fiber (130 μm^2), the more evanescent field would extend into the air holes of the SCMOF, which resulted in a larger ERI change of the guided mode with the refractive index liquids sucked into 3 air holes. The resolution was up 3×10^{-5} for the SCMOF with the liquid refractive index close to 1.33, which was an improvement of two orders of magnitude compared with the six-hole fiber, as illustrated in Fig. 2.2. Groothoff *et al.* inscribed an FBG into an MOF with a pure silica core based on the two-photon absorption at 193 nm [44]. The FBG in a pure silica core revealed a better thermal stability in comparison with those FBGs written in conventional solid core fibers by one-photon process at 244 nm.

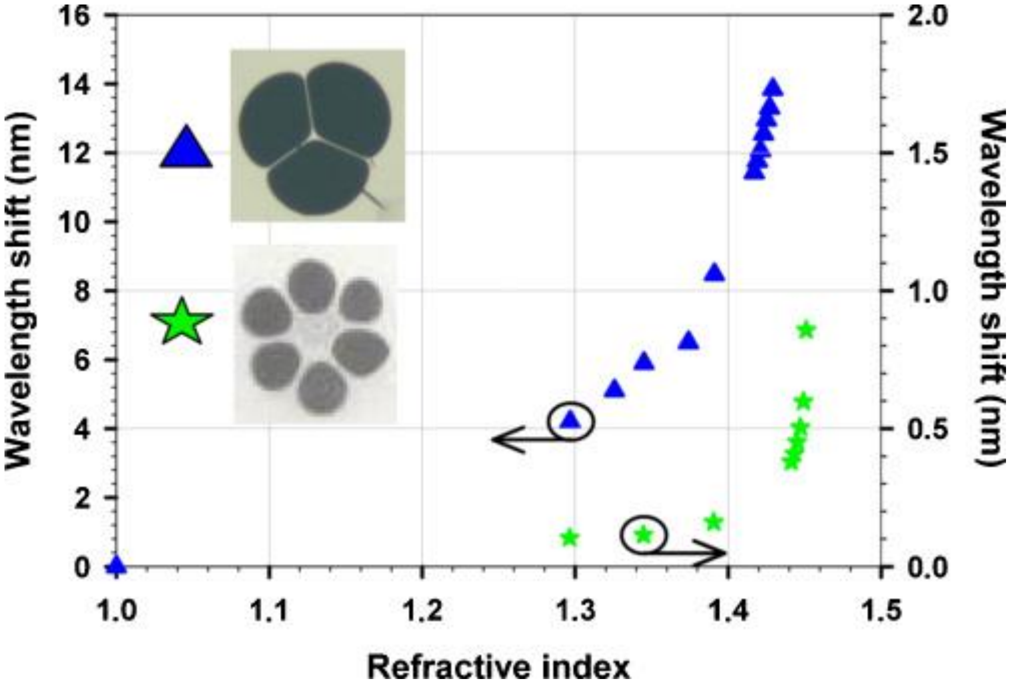

Figure 2.2 Shift of the Bragg wavelength versus the refractive index of the liquid filled into air holes for the SCMOF and for the six-hole MOF [43].

Besides the fabrication approaches based on the photo-induced refractive index variation of fiber core caused by UV lasers, there are several other methods to fabricate FBGs in MOFs. For example, high power femtosecond lasers are applied to introduce a periodical physical damage or deformation in fiber cores, which allows the FBG inscription in MOFs with non-photosensitive materials. Jewart *et al.* wrote an FBG in a two-hole fiber by utilizing a femtosecond laser at 800 nm with a 125 fs pulse and 1 mJ pulse energy [45, 46]. The laser was focused on the fiber core by a lens through a phase mask. The two-hole fiber with an FBG was used for pressure sensing with a high-temperature robustness at 800 °C. Compared with those written by ultraviolet light, FBGs inscribed by femtosecond lasers demonstrated a better temperature resistance, as shown in Fig. 2.3. Huang *et al.* wrote an FBG into a Butterfly MOF by the use of a femtosecond laser for pressure monitoring in high temperature and high pressure environments [47]. Several thermal treatments have been evaluated for developing a pressure sensor with a long-term stability. A pressure sensitivity of 3.3 pm/bar was obtained over a dynamic range of 0 to 1400 bar. Jewart *et al.* explored the bending response of an FBG in a SCMOF [48]. The fiber core of the SCMOF was surrounded by four air holes. A femtosecond laser was used to inscribe an FBG in the fiber core due to the non-photosensitive of the pure silica core. Since four thin silica struts reduced the bending-induced strain in the fiber core, the SCMOF integrated with the FBG revealed a bending insensitivity.

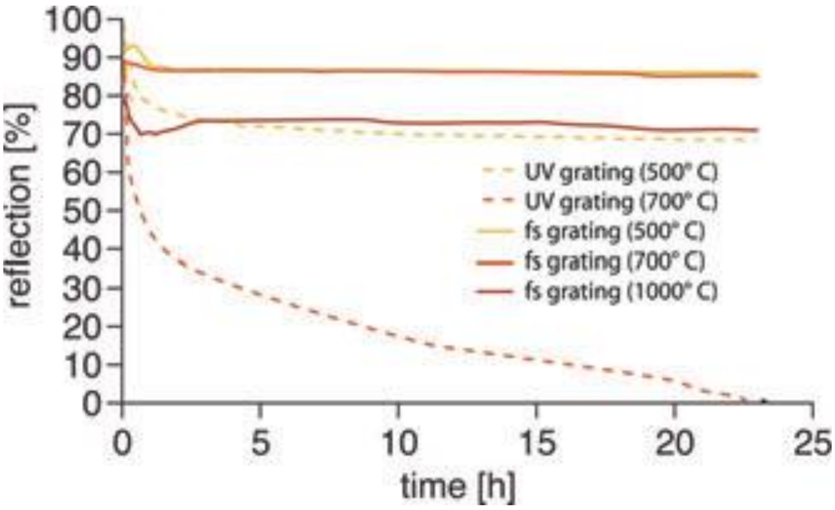

Figure 2.3 Annealing curves of UV-inscribed FBGs and femtosecond pulse-inscribed FBGs during 24 h [49].

2.2 LPFG sensors based on MOFs

An LPFG couples a propagating core mode into forward co-propagating cladding modes. Due to the high absorption and scattering of cladding modes, the transmission spectrum of LPFG contains a series of attenuation dips. Each dip corresponds to the coupling of the guided core mode and a different cladding mode. Unlike FBGs, since co-propagating cladding modes propagate forward, the attenuation dips are only observed in the transmission spectrum. The grating period of LPFG is typically from 100 µm and 1 mm [50], which is much larger than the grating period of FBG (~ 1 µm). Hence, LPFGs are relatively easier to fabricate. The wavelengths of attenuation dips are dependent on the grating period of LPFG and the ERI differences of core mode and cladding modes, which results in the sensitivity of LPFG to the local environment, such as temperature, strain, bending and refractive index of surrounding medium.

2.2.1 Operating principles of LPFG sensors

The resonant wavelengths of an LPFG are induced by the couplings between the core mode and cladding modes, which is similar with an FBG except the same propagation direction between core mode and cladding modes. Hence, similarly with Eq. 2.2, the resonant wavelengths can be calculated as [28, 51, 52]:

$$\lambda_i = (n_{eff,core} - n_{eff,cl}^{i})\Lambda \tag{2.13}$$

where $n_{eff,core}$ is the ERI of the guided core mode, and $n^{i}_{eff,cl}$ is the ERI of the i-th cladding mode and Λ is the grating period of the LPFG. From the comparison of Eq. 2.13 and Eq. 2.3, that LPFGs have the much larger grating period Λ than FBGs in the same wavelength band can also be found.

The minimum transmission value of the resonance dips can be expressed as [29, 53, 54]:

$$I_i = 1 - sin^2(\kappa_i L) \tag{2.14}$$

where κ_i is the coupling coefficient of the i-th cladding mode, which depends on the overlap integral between the core mode and the i-th cladding mode and the refractive index change induced by the periodic grating structure, and L is the length of the LPFG.

When the ambient temperature around an LPFG changes, the ERIs of core mode and cladding modes and the grating period will vary, which leads to the shift of resonant wavelengths. The process can be expressed mathematically as [52]:

$$\frac{d\lambda_i}{dT} = \frac{d\lambda_i}{d\left(\delta n_{eff}^{i}\right)}\left(\frac{dn_{eff,core}}{dT} - \frac{dn_{eff,cl}^{i}}{dT}\right) + \Lambda\frac{d\lambda_i}{d\Lambda}\frac{1}{L}\frac{dL}{dT} \tag{2.15}$$

where λ_i is the i-th resonant wavelength, T is the ambient temperature, $\delta n^{i}_{eff}=n_{eff,core}-n^{i}_{eff,cl}$, the first term represents the fiber material contribution, namely, the ERI changes of core mode and i-th cladding mode with temperature (the thermo-optic effect). The second term is the contribution from the grating structure, since it comes from the variation of the grating period with temperature. The sign of the second term is positive when the core mode couples to a low-order cladding mode, while it is negative with the core mode coupling to a higher-order cladding mode [50]. Hence, a temperature-insensitive sensor can be developed by designing a proper grating period for offsetting the contributions of two terms to temperature sensitivity, and a sensor with a positive or negative temperature sensitivity also can be realized.

Based on the similar calculation method, the shift of resonant wavelengths with an axial strain can be expressed as [52]:

$$\frac{d\lambda_i}{d\varepsilon} = \frac{d\lambda_i}{d\left(\delta n_{eff}^{i}\right)}\left(\frac{dn_{eff,core}}{d\varepsilon} - \frac{dn_{eff,cl}^{i}}{d\varepsilon}\right) + \Lambda\frac{d\lambda_i}{d\Lambda} \tag{2.16}$$

where $\varepsilon=\Delta l/l=\Delta\Lambda/\Lambda$ is the axial strain. The strain sensitivity also depends on two terms consisting of material and grating structure contributions. The material contribution is induced by the change of refractive index (strain-optic effect) and the deformation of transverse dimension (Poisson’s effect), and the grating structure contribution is determined by the change rate of resonant wavelengths with the grating period. For LPFGs with a grating period $\Lambda>100$ μm, the material contribution is typically negative, while the grating structure contribution is positive. Hence, by adjusting the fiber composition and the grating period, LPFGs with a positive, zero or negative strain sensitivity can be obtained.

The operation principle of LPFG-based refractive index sensors is that the ERIs of cladding modes depend on the refractive index of surrounding medium. Based on the Eq. 2.13, when the ERIs of cladding modes change with the variation of surrounding medium, the resonant wavelengths will shift. Since the ERI of a higher-order cladding mode change more with the surrounding medium, the resonant wavelength induced by the coupling between the core mode and a higher-order cladding mode possesses a higher refractive index sensitivity.

When a fiber with an LPFG is bent, the outer side of LPFG would be stretched and the inner side would be compressed, which results in the change of the ERIs of cladding modes. The evolution of resonant wavelengths with the bending has two ways: firstly, resonant dips shift with the bending; secondly, resonant dips split into two dips and the wavelength interval between two split dips increases with the bending.

2.2.2 Applications of LPFG sensors based on MOFs

The fabrication approaches of LPFGs in MOFs are similar with the FBGs, such as ultraviolet inscription, femtosecond pulses inscription, CO_2 lasers inscription and electrical discharges. These MOFs inscribed with LPFGs have widespread sensing applications. Firstly, we introduced the applications of six-hole MOFs inscribed LPFGs. Westbrook *et al.* wrote an LPFG into a Ge-doped core of an MOF by the ultraviolet inscription [55]. The MOF contained six 40-μm-diameter air holes. Then, a polymer was infused into the six air holes. Because of the high temperature sensitivity of the polymer, the transmission spectrum of this device shifted with the temperature variation. Han *et al.* investigated bending responses of an LPFG in a six-hole MOF inscribed by a 244-nm laser through a metal mask [56]. The bending sensitivity of this device was dependent on an axial rotation angle of the fiber. The shifts of the resonant dip for $\theta=0°$ and $\theta=180°$ differed by an order of magnitude at the curvature of 6.3 m^{-1}. Xu *et al.* inscribed an LPFG into the joint of a six-hole MOF and a standard SMF by CO_2 laser pulses [57]. Since the transmission spectrum of the LPFG possessed two groups of attenuation bands with different sensitivities to temperature and strain, the simultaneous measurement of temperature and strain was demonstrated with a temperature sensitivity of 0.086 nm/°C and a strain sensitivity of -2.18 nm/N.

Zhu *et al.* wrote an ultrashort LPFG (2.8 mm long) based on a large-mode-area MOF through CO_2 laser irradiation with a point-by-point technique [58]. The LPFG was composed of 8 periodic deformations with a grating period of 350 μm, which led to an ultra-compact size. Subsequently, Zhu *et al.* utilized a periodic stress relaxation technique based on CO_2 laser pulses to inscribe an LPFG in an endlessly single-mode MOF, which resulted in the LPFG area without deformation and elongation [59]. Compared with the temperature sensitivity of LPFG in a standard SMF, the device possessed an application potential as a temperature sensor in high temperature environment (below 990 °C) with a sensitivity of 10.9 pm/°C, as shown in Fig. 2.4. Meanwhile, the device had a negligible strain sensitivity.

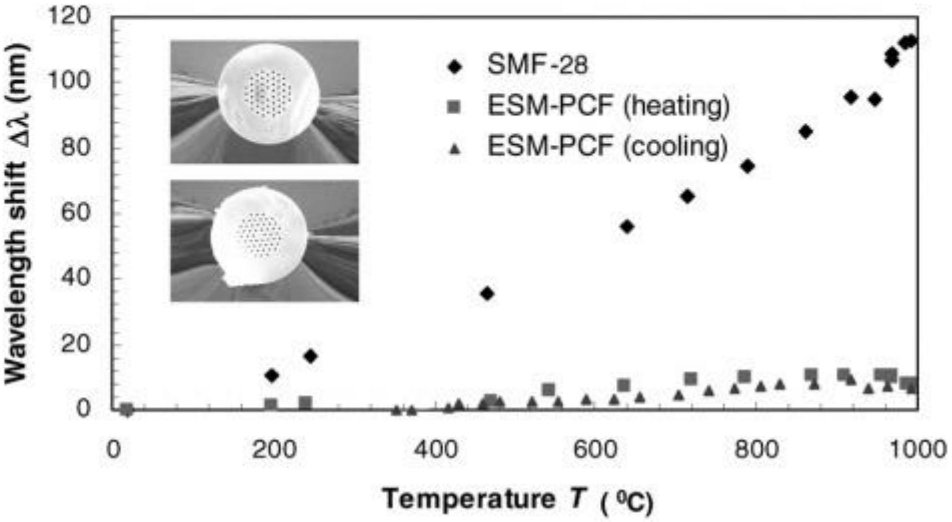

Figure 2.4 Resonance wavelength shift of LPFGs in the SMF and endlessly single-mode MOF with temperature [59].

Dobb *et al.* fabricated an LPFG in an endlessly single-mode MOF with a pure silica core by electrical discharges based on a commercial splicer [60]. This device presented the characteristic of temperature insensitivity with a strain sensitivity of -2.0 pm/$\mu\varepsilon$ and a bending sensitivity of 3.7 nm/m^{-1}. Subsequently, Petrovic *et al.* theoretically built a model to comprehensively explain the sensing characteristics of the LPFG reported in [60], including the insensitivity to temperature, and the sensitivity to external refractive index and strain [61]. Han *et al.* wrote LPFGs in Ge-doped cores of six-hole MOFs with different air-hole diameters [62]. These LPFGs presented similar temperature sensitivities. However, the strain sensitivities of these LPFGs improved with the air-hole diameter increase.

Rindorf *et al.* developed a refractometer by inscribing an LPFG in a large-mode-area MOF with methanol in cladding air holes [63]. The refractive index sensitivities of resonant dips were different and increased with the wavelength increase. The maximum sensitivity was up to 1500 nm/RIU at the refractive index of ~1.33. Zhang *et al.* wrote an LPFG into a side-channel MOF with a large air hole in the cladding for refractive index sensing [64]. A real-time refractive index sensing was realized by using two segments of side-polished SMFs to splice with the side-channel MOF.

The side-polished SMFs were applied to keep the side channel open, as shown in Fig 2.5. A linear sensitivity of 1145 nm/RIU was obtained in the refractive index range of 1.333-1.378.

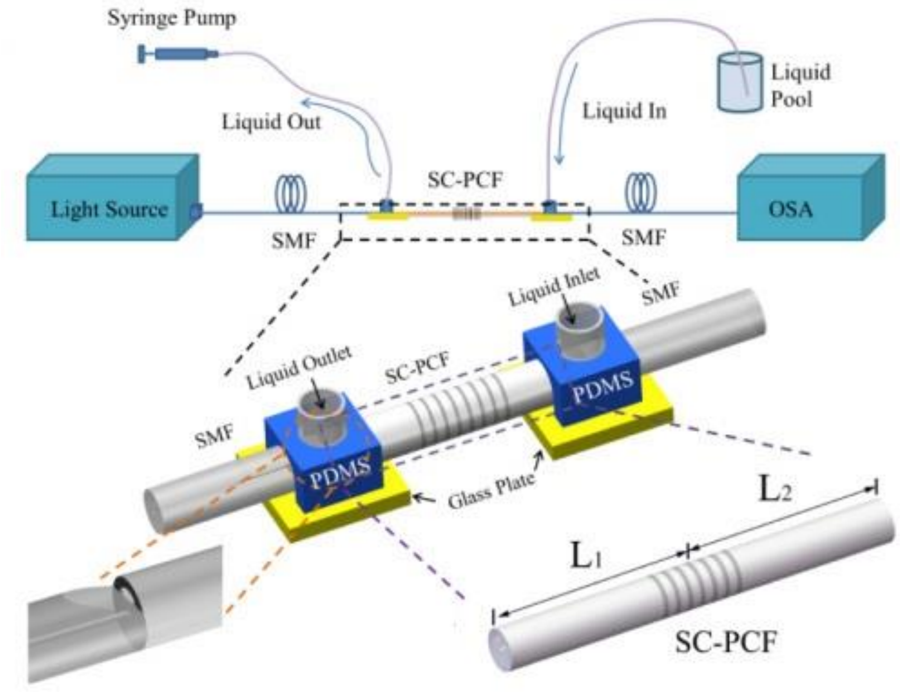

Figure 2.5 Scheme of the real-time refractive index sensing platform [64].

Lim *et al.* developed a pressure sensor by inscribing an LPFG in a single-mode MOF with mechanical pressure technique [65]. Later, Bock *et al.* wrote an LPFG in an endless single-mode MOF by computer-assisted electric arc discharge for pressure sensing [66]. The sensitivity of hydrostatic pressure reached 11.2 pm/bar with a negligible temperature sensitivity. Sun *et al.* theoretically simulated the simultaneous measurement of temperature and strain by utilizing an artificial neural network (ANN) based on an LPFG in a six-hole fiber [67]. The ANN approach was more suitable for sensors that suffered from nonlinearity and cross sensitivity in comparison of the conventional matrix inversion approach.

2.3 FPI sensors based on MOFs

An FPI is an optical cavity that consists of two parallel reflecting surfaces, where light at resonant wavelengths can only pass through. The instrument was developed by physicists Charles Fabry and Alfred Perot in 1899 [68]. Interference is induced by the multiple superposition between transmitted and reflected lights at two parallel reflecting surfaces [69]. For an optical fiber, since light is confined and guided in the fiber core, an FPI can be developed by building reflecting surfaces perpendicular to the direction of light propagation. Optical fiber based FPIs can be classified into two types: extrinsic FPIs and intrinsic FPIs, as shown in Fig. 2.6. In extrinsic FPIs, light will propagate outside the fiber and interfere in an external cavity. In intrinsic FPIs, light is always confined in the fiber and reflecting surfaces are located inside the fiber for building an intrinsic cavity.

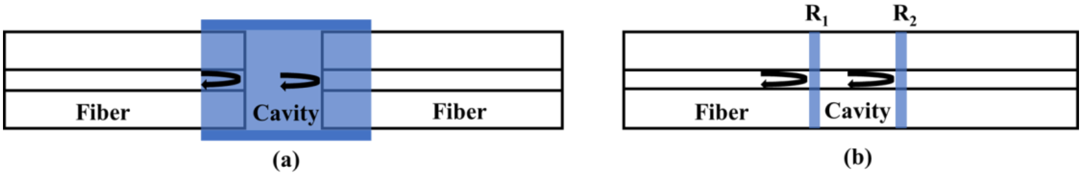

Figure 2.6 Schematic of extrinsic FPIs (a) and intrinsic FPIs (b).

2.3.1 Operating principles of FPI sensors

In an optical fiber based FPI, the interference is induced by the phase difference of transmitted and reflected beams at reflecting surfaces. The phase difference of an FPI can be expressed as [70]:

$$\phi_{FPI} = \frac{2\pi}{\lambda} n_{FPI} 2L_{FPI} \tag{2.17}$$

where λ is the light wavelength, n_{FPI} is the refractive index of the cavity material and L_{FPI} is the physical length of the cavity. When the phase difference is $\phi_{FPI}=(2m+1)\pi$, where m is a positive integer, the minimum peaks of interference spectrum appear at:

$$\lambda_{FPI} = \frac{4n_{FPI}L_{FPI}}{2m+1} \tag{2.18}$$

For theoretically understanding the sensing principle of FPI, a variate X is designated as an external parameter, such as temperature T, axial stain ε, hydrostatic pressure P, or refractive index of cavity material n_{FPI}. The dependence of resonant peaks on these external parameters can be expressed as:

$$\frac{d\lambda_{FPI}}{dX} = \frac{d}{dX}\left(\frac{4n_{FPI}L_{FPI}}{2m+1}\right) = \frac{4}{2m+1}\left(L_{FPI}\frac{dn_{FPI}}{dX} + n_{FPI}\frac{dL_{FPI}}{dX}\right) \quad (2.19)$$

The sensing sensitivity depends on two parts, including the variation of the refractive index of cavity material and the variation of cavity length with external parameters. Both of two parts can be concluded as the optical path difference variation of the interferometer.

2.3.2 Applications of FPI sensors based on MOFs

In past few years, the fabrication methods of MOF-based FPIs have been widely studied, such as micromachining technique, special splicing technique, chemical etching technique and thin film reflection technique. The FPI sensors based on MOFs will be reviewed roughly according to the category of external variates. Rao *et al.* fabricated an FPI by sandwiching a 2.1-mm-long HCMOF into two segments of SMFs, one of which, the lead-out fiber, was coated a reflecting film (Ti_2O_3) for enhancing the fringe visibility of reflection spectrum [71]. The accuracy of strain measurement of the device was up to ±5 με. Later, Wu *et al.* developed an FPI with a high fringe visibility without a coating film [72]. A short solid core MOF was first spliced with an SMF, then the other end-face of MOF was collapsed by an arc discharge to improve the reflectivity. The pressure sensitivity and temperature sensitivity of this sensor were around -5.8 pm/MPa and 13.7 pm/°C, respectively. Aref *et al.* developed a hydrostatic pressure sensor based on an FPI composed of a segment of SCMOF spliced into an SMF and HCMOF [73]. The reflecting surfaces of the FPI included the splice region of SCMOF and SMF and the interface of silica and air at the side of HCMOF. The pressure sensitivity of -4.68×10^{-5} nm/psi (-6.79×10^{-3} nm/MPa) was measured. Jin *et al.* experimentally and theoretically compared the sensing characteristics of hydrostatic pressure sensors based on two different FPIs, which were fabricated by splicing a segment of simplified HCMOF and hollow core photonic bandgap fiber (HCPBF) with two SMFs, respectively [74]. The simulation results indicated that the variation of cavity length dominantly determined the pressure sensitivity. The pressure sensitivities of the devices based on the simplified HCMOF and HCPBF were measured as -17.3 and -23.4 pm/MPa, respectively. The larger sensitivity was induced by the more easily deformable holey structure of the HCPBF. Since the hollow core could easily form a cavity and photonic bandgap fiber had a low transmission loss, HCPBFs were widely applied to fabricate various FPIs for sensing applications. Jauregui-Vazquez *et al.* developed a magnetic field sensor by filling a magnetic fluid into an FPI [75]. The magnetic fluid was composed of $Mn_{0.75}Zn_{0.25}Fe_2O_4$ nanoparticles dispersed in oleic acid with a coercive field of 10.7 mT. The FPI, including multiple reflections, was fabricated by splicing an SMF and a HCPBF with a special arc discharge method. The sensitivity of the magnetic field sensor was 0.11 dB/mT. Liu *et al.* demonstrated an FPI for microorganism growth detection [76]. The FPI was composed of a 20.8-um-long HCPBF sandwiched into two SMFs. The refractive index sensitivity of the device was -136 dB/RIU by tracing the fringe contrast of reflection spectra. Then, the detection of yeast growth was demonstrated in liquid. Yu *et al.* developed a vibration sensor based on an FPI that was formed by sandwiching an 18.5-mm-long Kagomé HCMOF into two segments of SMFs [77]. Through collecting reflected signals by a photodetector and converting them into electrical singals, a single-frequency vibration with a dynamic range from 1 to 20000 Hz could be accurately detected, and a dual-frequency vibration could also be measured. In addition, an ultralow temperature sensitivity of 0.57 pm/°C was observed in the range of 30 to 100 °C. Villatoro *et al.* fabricated an FPI by a simple arc discharge technique [78]. A micro-air-bubble with a diameter of 58 μm was formed as a cavity when a hexagonal lattice MOF was spliced with a conventional SMF. The FPI exhibited a strain sensitivity of 2.7 pm/με with a low temperature sensitivity of 0.95 pm/°C.

Besides, open-cavity FPIs were developed for refractive index sensing. Wu *et al.* developed a refractive index sensor by inserting a C-shaped fiber into two SMFs for building an open-cavity FPI, which allowed liquid or gas samples to enter the cavity [79]. The refractive index sensitivity reached 1368 nm/RIU in the range of 1.33 to 1.36. This device provided potential applications in the fields of label-free chemical and biological sensing. Tian *et al.* demonstrated another kind of refractive index sensor based on an open-cavity FPI formed by a concave-core MOF [80]. The refractive index sensitivity was measured to be 1636 nm/RIU with a low temperature cross-sensitivity. Wang *et al.* fabricated an intrinsic FPI based on an etched solid core MOF for refractive index sensing [81]. After splicing with an SMF, the solid core

MOF with a 7-µm-diameter fiber core was placed in 49% hydrofluoric acid for 120 s, then a suspended core structure was obtained. Although, a low refractive index sensitivity of 79.3 nm/RIU was measured, a simple method was provided to fabricate an open-cavity FPI.

Since gas could be used as the medium material of an FPI cavity, FPI-based gas sensors were also proposed and demonstrated. Yang *et al.* demonstrated a gas sensor by sandwiching an HCMOF into two SMFs, where the HCMOF was drilled holes on the side by a femtosecond laser, as shown in Fig. 2.7 [82]. The noise equivalent concentration for C_2H_2 gas could go down to 117 parts-per-billion (ppb) under 77 s averaging time. Wang *et al.* developed a gas refractometer based on an open-cavity FPI [83]. The FPI was constructed by cascading SMF, multimode fiber and two HCMOFs with different core diameters. The multimode fiber could help to collect more diverged light from the cavity and improve the fringe visibility. Nitrogen with gradually increase pressures was applied to investigate the gas refractive index sensitivity of the sensor and 1127.5 nm/RIU was achieved. López-Torres *et al.* demonstrated an ammonia gas sensor based on an FPI with a coated SnO_2 film [84]. The FPI was fabricated by splicing MOF with a double-Y-shape core to an SMF. The SnO_2 films with different thickness were deposited on the top of the FPI sensing head by a sputtering machine from 200 to 850 nm, respectively. The gas sensor with an optimal 625-nm-thickness SnO_2 could detect the ammonia with a concentration of 10 ppm. Aldaba *et al.* developed a relative humidity sensor based on a similar FPI head with a SnO_2 film [85]. The SnO_2 was deposited on the inner wall of air holes of a double-Y-shape-core MOF and the top of the sensor head. Instead of monitoring the change of peaks or valleys in optical spectra, the sensor was to trace the Fast Fourier Transform (FFT) phase variation of the interference frequency. The maximum sensitivity was 0.14 rad/% RH within a relative humidity range from 20%-90% RH. Meanwhile, the potential of the device as a breathing sensor was investigated experimentally.

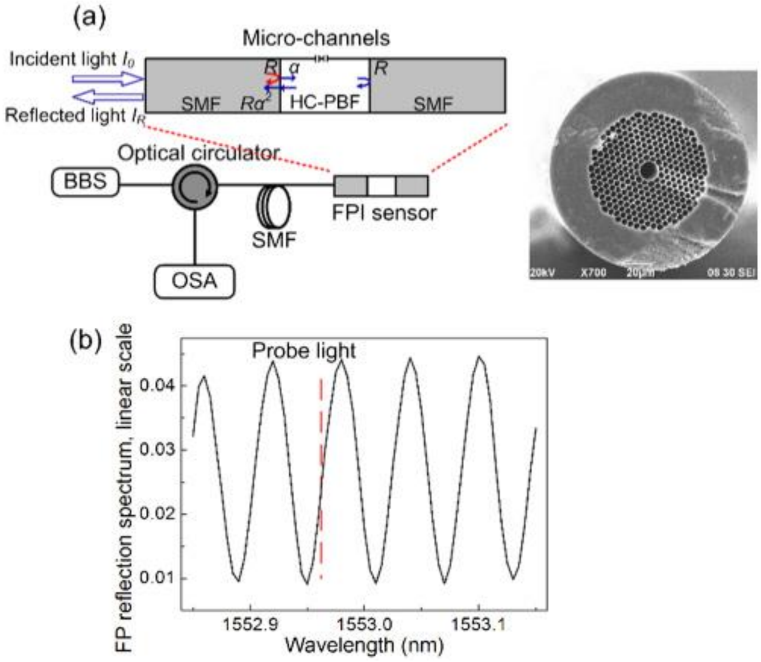

Figure 2.7 (a) Setup schematic for monitoring the reflection spectrum of FPI and the cross section of the HCMOF with a microchannel; (b) Measured refection spectrum [82].

Choi *et al.* fabricated a high temperature sensor based on two cascaded FPIs [86]. A 70-µm-long HCMOF and a 510-µm-long SMF were spliced to a commercial solid core MOF for constructing FPIs, where the solid core MOF was used to guide light into FPIs from a light source. The reflection spectra with the temperature variation from 50 to 1000 °C were measured and analyzed. The results indicated that the thermal-optic effect of the cavity material was dominant compared with the thermal expansion of the cavity length. Lee *et al.* developed a novel optical fiber-based level meter based on a micro-air-bubble in an HCMOF filled with liquid [70]. The air bubble would stay at the middle of the HCMOF when the device was at the horizontal level and would drift to left side or right side when the device was tilted, as shown in Fig. 2.8. The tilted directions (clockwise and counterclockwise) could be distinguished from the evolution of free spectral range (FSR) of the liquid cavity.

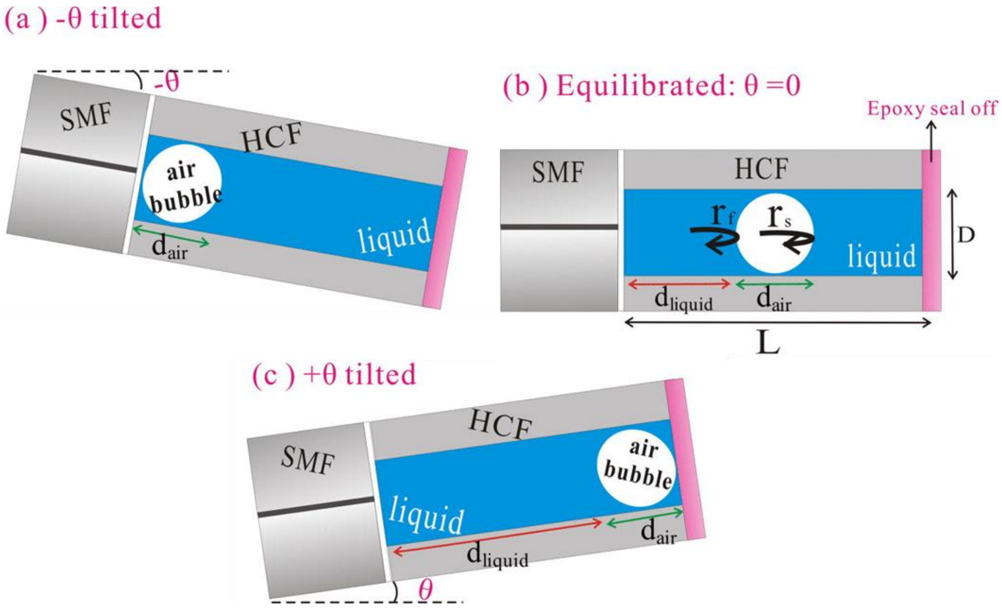

Figure 2.8 Schematic of eventual positions of the air bubble in the fiber-based level meter with the conditions of (a) clockwise inclination, (b) equilibration, and (c) counterclockwise inclination, respectively [70].

2.4 SI sensors based on MOFs

SI, also called a ring interferometer, was proposed and demonstrated by French physicist Georges Sagnac in 1913 [87]. A beam of light is split into two beams and then the two beams propagate along a same path but in opposite directions. After returning the entry point, the two beams of light will exit the ring and take place interference. When the optical path difference of the two beams of light changes, the interference fringe will shift. The optical fiber based SI was first demonstrated as a gyroscope by Vali and Shorthill in 1976 [88]. In the past few years, besides the application as an optical gyroscope, optical fiber based SIs have been widely applied in the fields of physical parameter sensing, biomedical sensing and chemical sensing due to the advantages of simple structure, easy fabrication and environmental robustness.

2.4.1 Operating principles of SI sensors

Nowadays, for most of optical fiber based SIs, a 3 dB fiber coupler is utilized to split the input light into two counter-propagating beams with a same power. For maximizing the optical path difference governed by polarization-dependent propagation speeds of guided modes in the fiber loop, birefringent optical fibers are typically used as a sensing unit [69]. The output spectrum of the 3 dB coupler is determined by the interference between the two counter-propagating beams that are polarized along the fast axis and slow axis of the birefringent optical fiber, respectively. The phase difference of the two orthogonal guided modes is given by:

$$\delta_{SI} = \frac{2\pi}{\lambda} B L_B \tag{2.20}$$

$$B = \left| n_f - n_s \right| \tag{2.21}$$

where B is the birefringent coefficient of the fiber in the Sagnac loop, L_B is the length of the birefringent fiber, and n_f and n_s are the ERI of the fast and slow modes, respectively [89]. Further, the output spectrum of the fiber loop can be approximately expressed as:

$$T = [1 - \cos(\delta_{SI})]/2 \tag{2.22}$$

Hence, in the interference spectrum, when $\delta_{SI} = 2m\pi$ (m is an integer), dips will appear and can be simply calculated as:

$$\lambda_{SI} = B L_B / m \tag{2.23}$$

When an external variate X, such as temperature T, axial stain ε, hydrostatic pressure P, or magnetic field H, is applied to an SI, the dependence of resonant dips on these external parameters can be expressed as:

$$\frac{d\lambda_{SI}}{dX} = \frac{d}{dX}\left(\frac{BL_B}{m}\right) = \frac{1}{m}\left(L_B \frac{dB}{dX} + B \frac{dL_B}{dX}\right) \tag{2.24}$$

The sensing sensitivity is determined by two parts, which include the variation of birefringent coefficient of the fiber and the variation of the length of birefringent fiber with external parameters.

2.4.2 Applications of SI sensors based on MOFs

To date, many MOFs with the characteristic of high birefringence or polarization maintaining were applied in the SIs as sensing units for obtaining a high sensitivity. In this section, we will introduce MOF based SIs from the category of external variates. Moon *et al.* investigated the temperature response of SIs based on three kinds of polarization-maintaining MOFs [90]. These MOFs had side holes and Ge-doped cores with different doping amounts, respectively, which led to different thermal expansion coefficients of fiber cores. In these MOFs, the maximum dB/dT was up to -2.72×10^{-7} /°C that was higher than the dB/dT of the standard polarization-maintaining MOFs ($\sim 10^{-8}$ /°C). Han *et al.* developed a highly sensitive temperature sensor by inserting a selective-filling MOF into a Sagnac loop [91]. A liquid with a refractive index of 1.52 and a thermal-optic coefficient of -0.000407 /°C was selectively infiltrated into two adjacent air holes at the layer closest to the fiber core. The temperature sensitivity of the sensor was highly dependent on the actual temperature, and an ultrahigh sensitivity of -26.0 nm/°C at 50.0 °C was experimentally obtained. Reyes-Vera *et al.* developed a highly sensitive temperature sensor by building an SI based on a metal filled side-hole MOF [92]. Indium with an expansion coefficient of 32.1×10^{-3} /K was infiltrated into the two side holes of the MOF. Due to the expansion of indium with the temperature variation, the birefringence of the MOF would be modified by the temperature change. A high temperature sensitivity of -9.0 nm/°C was observed.

Frazão *et al.* demonstrated a temperature-independent strain sensor by building an SI based on a four-hole SCMOF [93]. A relatively large strain sensitivity of 1.94 pm/με and a low temperature sensitivity of 0.29 pm/°C were investigated. Dong *et al.* demonstrated a strain sensor based on a Sagnac loop integrated with a standard polarization-maintaining MOF [94]. An 86-mm-long polarization-maintaining MOF with a non-circular core surrounded by different-diameter air holes at two orthogonal axes was used as the sensing unit in the SI. The group birefringence of the MOF was 8.7×10^{-4} at 1550 nm and a sensitivity of 0.23 pm/με was obtained with a large dynamic range from 0 to 32 mε. Liu *et al.* designed and fabricated a high-birefringence SCMOF with an elliptical core surrounded by six air holes [95]. The group modal birefringence of the SCMOF were experimentally investigated to be 4.84×10^{-4} based on the Sagnac loop, which was consistent with the theoretical result. This SI sensor had a hydrostatic pressure sensitivity of 2.82 nm/MPa, a strain sensitivity of 0.43 pm/με, a normalized torsion sensitivity of 0.0157 /° (an extinction ratio variation), and a low temperature sensitivity of 1 pm/°C. Subsequently, Liu *et* *al.* fabricated another large dynamic range pressure sensor based on an SI composed of a novel birefringence MOF [96]. The MOF possessed an elliptical Ge-doped core surrounded by two large semicircle holes (with a radius of 40 μm). The theoretical and experimental group birefringence of the MOF at 1550 nm were 1.49×10^{-4} and 1.23×10^{-4}, respectively. A pressure sensitivity of 45 nm/MPa was measured in the range of 0-4000 kPa. Fu *et al.* demonstrated a pressure sensor by inserting a polarization-maintaining MOF into a Sagnac loop, as illustrated in the Fig. 2.9 [89]. The cross section of the classical polarization-maintaining MOF was also shown in Fig. 2.9. The mode field diameters of two orthogonal polarization modes were experimentally measured to be 3.6 and 3.1 μm, respectively. A pressure sensitivity of 3.42 nm/MPa was investigated using a 58.4-cm-length polarization-maintaining MOF.

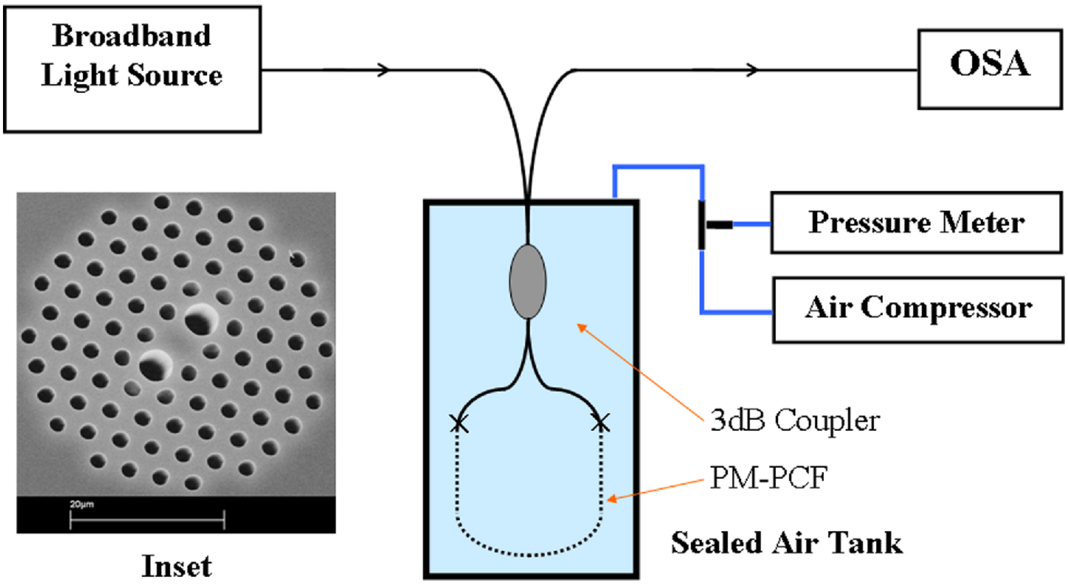

Figure 2.9 Schematic of the pressure sensor and the cross section of the polarization-maintaining MOF [89].

Frazão *et al.* developed a curvature sensor by inserting a Hi-Bi MOF into an SI [97]. The MOF was designed and fabricated with a special cladding structure, in which a half was composed of large diameter holes (3.3 μm) and the other half was small diameter holes (1.6 μm). Due to the geometry, the fiber core was not located at the center of the fiber and the fiber had a high birefringence. Meanwhile, the sensor also exhibited a direction-dependent curvature sensitivity. Zu *et al.* demonstrated a transverse mechanical load sensor by inserting a solid core MOF into an SI [98].

Since the solid core MOF possessed a circular symmetrical core with a diameter 10 µm, the MOF was almost non-birefringent. For introducing the birefringence, an initial transverse force was mechanically applied on the MOF. A load sensitivity of 0.519 $nm \cdot N^{-1} \cdot mm^{-1}$ was obtained with a resolution of 0.048 $mN \cdot mm^{-1}$ and a dynamic range from 0 to 20 N. Bravo *et al.* developed a high precision micro-displacement sensor based on an SCMOF in a Sagnac loop [99]. Although the 3-hole SCMOF had multimode interference behaviour, the response to micro-displacement was only induced by the birefringence. A high precision of 0.45 µm was measured with a high stability and an insensitivity to temperature.

Zhao *et al.* developed a magnetic field sensor by inserting a ferrofluid-filled high birefringence MOF into an SI as a sensing unit [100]. The water-based ferrofluid was infiltrated into all air holes of the MOF by using a syringe. Since the refractive index of the ferrofluid would change with the external magnetic field, the birefringence of the MOF would vary accordingly, which led to the shift of the interference spectrum. A magnetic field sensitivity of 0.073 nm/mT was measure in the range of 10 to 40 mT with a resolution of 0.001 mT.

Li *et al.* developed a high sensitivity SI biosensor based on an exposed core MOF, as shown in Fig. 2.10 [101]. Since the exposed core was noncircular symmetry, the fiber possessed the characteristic of birefringence. The exposed core MOF allowed analytes to directly access the evanescent field without post-processing methods. A bulk refractive index measurement revealed a high refractive index sensitivity (-3137 nm/RIU) of this device. A label-free biological molecule (molecule streptavidin) sensing was also demonstrated by immobilizing biotin on the exposed core.

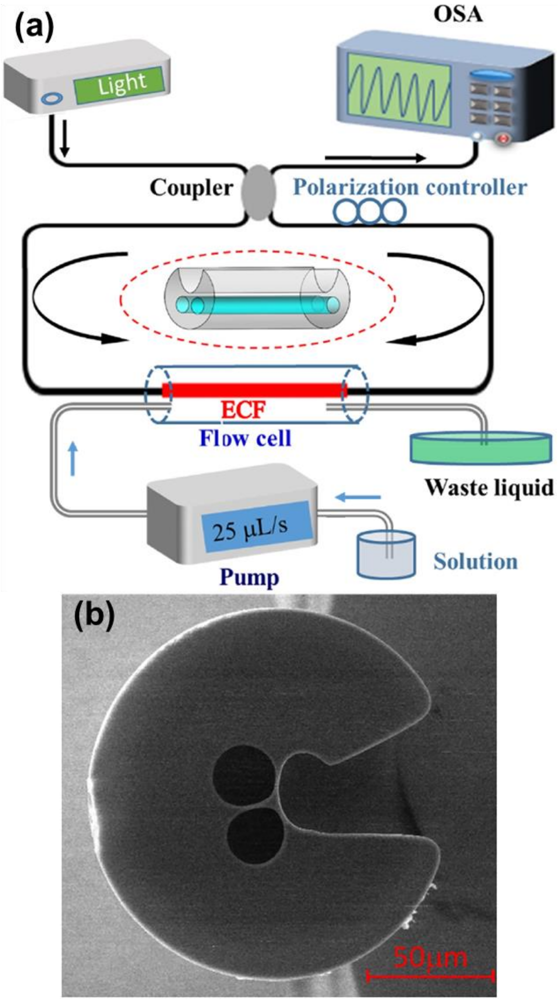

Figure 2.10 (a) Schematic of the SI biosensor based on the exposed core MOF; (b) Scanning electron microscope (SEM) image of the cross section of the exposed core MOF [101].

2.5 MZI sensors based on MOFs

MZI was proposed by Ludwig Zehnder in 1891 and was refined by Ludwig Mach in 1892 [102, 103]. Initially, the operation mechanism of the MZI is to split light into two collimated beams, then after propagating along two different paths, the two beams recombine together and interfere with each other, as shown in Fig. 2.11. The shift of the phase difference between the two beams, which is induced by a variation of the path length or a sample in the path, can be measured by monitoring the change of the interference pattern or interference spectrum. Early optical fiber based MZIs also possess two independent arms. One of them, the reference arm, is isolated from external variations. The other one is treated as the sensing arm and affected by the variation of external environment, such as temperature, strain, or bending, which can be detected by monitoring the interference spectrum. However, the scheme of two independent arms may cause some disadvantages, for instance, it is challenging to isolate the reference arm from the external environment all the time. Hence some in-line optical fiber based MZIs have been proposed and demonstrated, where their reference arms and sensing arms are the same fiber. Since a lot of in-line MZIs are applied in the sensing field recently, in-line MZIs will be mainly discussed in next sections.

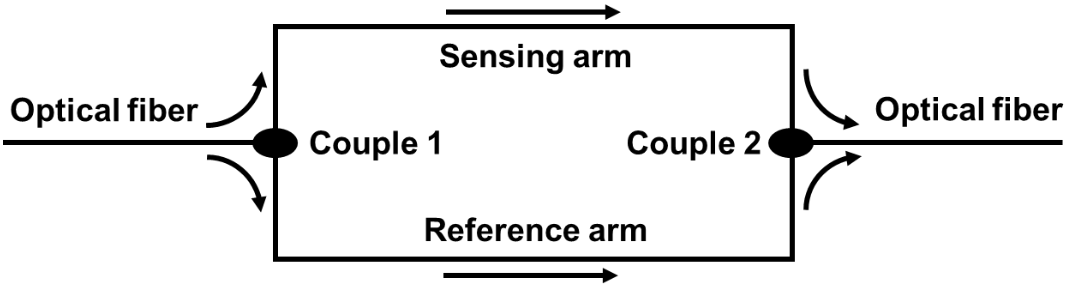

Figure 2.11 Schematic of a classic fiber-based MZI with a reference arm and a sensing arm.

2.5.1 Operating principles of MZI sensors

In an in-line optical fiber based MZI, although interference modes propagate along a same fiber, these modes have different optical path lengths due to the modal disperison. The intensity of the interference spectrum can be calculated as:

$$I_{MZI} = I_1 + I_2 + 2\sqrt{I_1 I_2}\cos\left(\varphi_{MZI}\right) \tag{2.25}$$

where I_1 and I_2 are the light intensities of two interference modes, respectively, φ_{MZI} is the phase difference of two interference modes and can be calculated as:

$$\varphi_{MZI} = \frac{2\pi}{\lambda}\Delta n_{eff} L_{MZI} \tag{2.26}$$

where λ is the wavelength, Δn_{eff} is the ERI difference of two interference modes, L_{MZI} is the length of the interference region. From Eq. 2.25, when $\varphi_{MZI} = (2m+1)\pi$, ($m$ is an integer), the interference spectrum will present dips at the wavelengths:

$$\lambda_{MZI} = \frac{2\Delta n_{eff} L_{MZI}}{2m+1} \tag{2.27}$$

The resonant wavelengths are dependent on the ERI difference of interference modes and the length of the interference region. Since the variation of external environment can lead to the change of the ERI of interference modes or the length of interference region, optical fiber based MZIs can be used to sensing external parameters, such as strain, temperature, bending and pressure. For example, when an axial strain ε is applied to an MZI, the dependence of resonant dips on the strain ε can be expressed as

$$\frac{d\lambda_{MZI}}{d\varepsilon} = \frac{2}{2m+1}\frac{d}{d\varepsilon}\left(\Delta n_{eff}L_{MZI}\right) = \frac{2}{2m+1}\left(L_{MZI}\frac{d\Delta n_{eff}}{d\varepsilon} + \Delta n_{eff}\frac{dL_{MZI}}{d\varepsilon}\right) \quad (2.28)$$

where the axial strain $\varepsilon=\Delta L_{MZI}/L_{MZI}$, ΔL_{MZI} is the length change of the interference region. The shift of resonant dips with the strain is determined by two terms. The first term represents the change of ERI (strain-optic effect) and the deformation of transverse dimension (Poisson's effect). The second term is determined by the length change with the axial strain. For other external parameters, a similar derivation method can be applied to explain the sensing principles.

2.5.2 Applications of MZI sensors based on MOFs

In past few years, many MOF based MZIs have been proposed and developed for sensing applications. The schemes of the MOF based MZIs include the use of multimode MOF, selectively infiltrated MOF, and lateral offset splicing etc. In this section, MOF based MZIs will be reviewed based on the category of sensing applications. Gerosa *et al.* developed an MZI for temperature sensing based on a solid core MOF [104]. The cladding of the solid core MOF was hexagonal-pattern air holes. Through applying differential pressure in the cladding holes, one hole closest to the fiber core was collapsed by the arc discharge produced from a fiber splicer. When light reached the local elliptical core, more than one mode would be excited, which led to a robust in-line MZI. The temperature sensitivity of the sensor was measured to be -53.4 pm/°C. Yang *et al.* demonstrated a highly sensitive temperature sensor based on an in-line MZI that was fabricated by selectively infiltrating a solid core MOF [105]. The cladding holes of the MOF were arranged in a hexagonal pattern. A liquid with a higher refractive index than silica was selectively infiltrated into two adjacent cladding air holes based on a femtosecond laser. The interference was generated between the fundamental core mode and the guided mode in the area filled with liquid. A high temperature sensitivity of 7.3 nm/°C was measured with a MOF length of 3.4 cm. Deng *et al.* demonstrated a temperature sensor based on an MZI with a side-opened channel [106]. The in-line MZI was composed of a segment of solid core MOF sandwiched into two SMFs with a lateral-offset splicing, as illustrated in Fig. 2.12. The solid core MOF consisted of a 14-μm-diameter fiber core surrounded by six air holes. Isopropanol was infiltrated into one of six air holes through two side-opened holes drilled by a femtosecond laser. Due to the high thermo-optic coefficient of the isopropanol, a high temperature sensitivity of 3.8 nm/°C was obtained in the range of 22 to 34 °C. Geng *et al.* developed a highly sensitive temperature sensor based on a fully liquid-filled MOF [107]. The MOF was composed of a solid core and five-layer air holes in a hexagonal pattern. Through splicing the fully liquid-filled (refractive-index-matching oil) MOF into two SMFs with a lateral offset, an in-line MZI was fabricated for temperature sensing. A high temperature sensitivity of -1.83 nm/°C was measured. Liang *et al.* demonstrated an in-line MZI based on a selectively infiltrated MOF for highly sensitive temperature and strain sensing [108]. The MOF possessed a solid core and 5-layer air holes. A liquid with a thermal-optic coefficient of -3.9×10^{-4} RIU/°C was selectively infiltrated into an air hole closest to the fiber core, as shown in Fig. 2.13. A 2.5-cm-length liquid-filled MOF was inserted into two SMFs to form an in-line MZI. The Fourier transform spectrum of the device indicated that one fundamental mode and three higher-order modes formed the interference spectrum. An ultrahigh temperature sensitivity of 16.49 nm/°C and a strain sensitivity of -14.595 nm/N were measured.

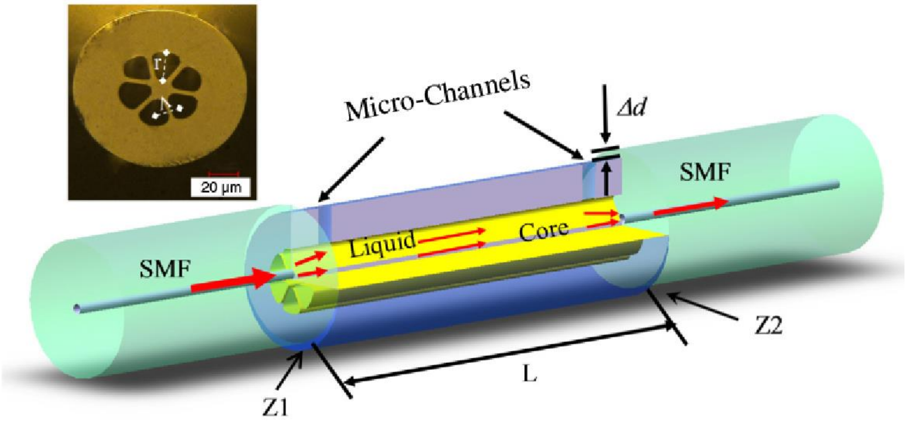

Figure 2.12 Schematic of the proposed temperature sensor based on the MZI. Inset: SEM image of the cross section of the MOF [106].

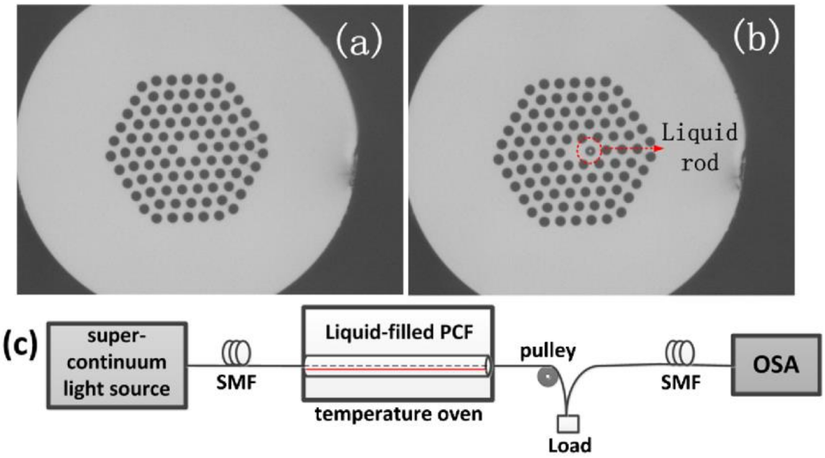

Figure 2.13 SEM images of the cross section of (a) the MOF and (b) the liquid-filled MOF; (c) Schematic of the temperature measurement setup [108].

Kim *et al.* developed an MZI based on a twin core MOF for strain sensing [109]. The twin core MOF was spliced with two segments of SMFs to build the MZI. Two elliptical solid cores with a small difference of ERIs led to a multimode interference. The strain sensitivities were measured to be -1.8 pm/με, -2.0 pm/με and -2.18 pm/με at three wavelength ranges of 1450 nm, 1500 nm and 1550 nm, respectively, which indicated that the strain sensitivity was dependent on the wavelength. Hu *et al.* fabricated a strain sensor based on a modified MZI [110]. A solid core MOF with four-layer air holes in a hexagonal pattern was applied to build a normal MZI by sandwiching it into two SMFs, then the modified MZI was realized by fabricating a collapsed region at the middle of the MOF. The modified MZI possessed a much larger extinction ration of 27.88 dB compared with the normal MZI (4.05 dB). An intensity-modulated strain sensitivity of 11.22 dB/mε was obtained with a resolution of 0.89 με. Zheng *et al.* developed a refractive index insensitive strain sensor based on a multimode MOF [111]. The MOF was composed of a 6-µm-diameter solid core and two-layer air holes in a hexagon pattern. The ratio between the size of air holes and the pitch of air holes was around 93%, which led to a multimode propagation in the fiber core. Hence, an MZI was fabricated by splicing the multimode MOF into two SMFs. The independence of the device on refractive index has been investigated and a strain sensitivity of 2.1 pm/με was obtained. Bai *et al.* fabricated a strain sensor by integrating an in-line MZI into a fiber ring cavity laser [112]. The MZI was constructed by sandwiching a segment of photonic crystal MOF into two SMFs with two collapsing areas at two spliced joints. The MZI was inserted into the ring cavity of a fiber laser as an optical band-pass filter and a strain sensing unit. A strain sensitivity of 2.1 pm/με was measured by tracing the central wavelength of the laser output in the dynamic range of 0 to 2100 με.

Wong *et al.* demonstrated a refractive index sensor by integrating an MOF-based MZI into a cavity ring-down loop [113]. The MZI was built by sandwiching a short segment of common photonic crystal MOF into two SMFs with collapsed air holes at two splicing points. Through utilizing the cavity ring-down technique, a refractive index detection limit of 7.8×10^{-5} RIU was obtained. Shavrin *et al.* developed a gas refractometer based on a two-arm MZI, which could measure both real and imaginary parts of the complex refractive index [114]. The two arms of the MZI included an HCMOF and a standard SMF, respectively. Light from a tunable laser was split into two beams by a 50/50 beam splitter, and then was focused into each arm by lens. The interference pattern was monitored by a CCD behind a window of a gas chamber. The resolution of the gas refractometer was measured to be 4×10^{-7}. Andrews *et al.* developed a gas refractive index sensor by utilizing an HCMOF based in-line MZI [115]. The HCMOF consisted of a hollow core with a diameter of 9.6 µm and surrounding 8-layer air holes with a diameter of 3.4 µm and a pitch of 3.8 µm. The MZI was fabricated by using two ceramic ferrules to connect the HCMOF with two SMFs, which allowed the gas to flow in and out from the HCMOF. A gas refractive index sensitivity of 1233 nm/RIU was achieved. Minkovich *et al.* fabricated a gas sensor based on an MZI coated with a thin film [116]. A large-mode-area MOF with a four-layer air holes in a hexagonal pattern was tapered to build an in-line MZI. The collapsing of the holes located at the waist of the taper generated a multimode region. An 8-nm palladium film was deposited on the multimode region, where the evanescent field could interact with the film. The concentrations of hydrogen (mixed with nitrogen) from 0 to 5.6% were effectively detected.

Nguyen *et al.* demonstrated a biosensor by utilizing an exposed core MOF based MZI [117]. Due to the triangular core of the MOF, multiple modes were excited when light was irradiated into the MOF from a lead-in SMF. An interference spectrum was observed from a lead-out SMF. By immobilizing biotin molecules onto the exposed core as a capturing probe, streptavidin with a concentration of 0.029 mM was detected by the biosensor.

Frazão *et al.* demonstrated an in-line MZI by sandwiching a suspended twin-core MOF into two SMFs [118]. The MOF contained two suspended triangle cores with a diameter of 1.5 µm, two big and two small air holes with diameters of 10 and 5 µm, respectively. Since the fiber cores had the characteristic of birefringence, two MZIs were obtained by irradiating lights with two orthogonal polarizations into the device. Hence, the MZI sensor could discriminate bending from temperature based on the matrix method. However, the coupling efficiency between the SMF and the suspended twin-core MOF was low, which led to a large transmission loss of more than 30 dB. On the other hand, for only exciting an x-polarization state or y-polarization state in the twin cores, the cores should be in tension or in compression, respectively, which limited the practical application of the bending sensor. Sójka *et al.* developed an N-path MZI based on a multicore MOF [119]. The multicore MOF was composed of a core in the center surrounded by six cores and small air holes with a hexagon pattern in the cladding. The diameter of all cores was 5.15 µm and each core possessed the property of endlessly single-mode propagation. The light was coupled in and out from the multicore MOF by using conventional FC/PC fiber connectors. A bending sensitivity of -24.65 nm/m^{-1} and a low temperature sensitivity of 1.6 pm/°C were measured. But the FC/PC fiber connectors that was used to connect the multicore MOF and SMFs restricted the integration. Besides, the symmetric multicore structure resulted in the compensation of refractive index variation when the multicore MOF was bent, so the low bending sensitivity of -0.02465 nm/m^{-1} was obtained. Deng *et al.* developed a bending sensor based on an MZI, which was fabricated by splicing a section of photonic crystal MOF into two SMFs with a collapse of air holes at the first splice point and a small lateral offset at the second splice point [120]. Due to the collapse of air holes, cladding modes were excited and propagated in the MOF. Subsequently, cladding modes and core mode were coupled into the core of SMF because of the lateral offset splicing. A bending sensitivity of 3.046 nm/m^{-1} was obtained with a low temperature sensitivity of 0.0019 nm/°C. However, the collapsing and offset located at the splicing points increased the complexity of the fabrication and decreased the fabrication repeatability and the robustness of the sensor. Shin *et al.* demonstrated a highly sensitive bending sensor based on an in-line MZI, which was composed of two identical LPFGs separated by 55 mm in a solid-core large-mode-area MOF [121]. A cladding mode was excited at the first LPFG, then propagated along the MOF. The cladding mode would couple back to fiber core at the second LPFG, which resulted in the interference with the core mode. A high bending sensitivity of 36.16 nm/m^{-1} was obtained when the curvature was larger than 0.9 m^{-1}. But the fabrication of LPFGs required a CO_2 laser and alignment components. The curved fiber located in the middle of the two LPFGs led to a relatively low bending sensitivity of 3.05 nm/m^{-1} from 0 to 0.92 m^{-1}, which also limited the consistency of the bending sensitivity.

2.6 Summary

In this chapter, the MOF-based sensors have been introduced. The schemes of these MOF-based sensors contain two types. One type is to inscribe FBGs or LPFGs in the MOFs, and the other one is the type of interferometer, including FPIs, SIs or MZIs. The sensing principles of these schemes have been discussed. The applications of these MOF-based sensors have been reviewed.

Chapter 3 Experimental and numerical investigation on HCMOF based bending sensor

Optical fiber sensors have attracted widespread attention due to the rapid development of optical fibers from the middle of the last century [122-126]. Bending sensors have been used in many fields such as mechanical engineering, structural monitoring and astronautics. In the past few years, various specialty optical fibers have been developed for bending measurements such as tapered fibers [127-130], microfibers [131, 132], multicore optical fibers [133, 134], eccentric core fibers [34, 135, 136] and polymer optical fibers [137, 138]. However, tapered fibers or microfibers with a small size are fragile and easily deteriorate due to external airflow or dust. For multicore optical fibers, eccentric core fibers and polymer optical fibers, most of the schemes are to inscribe Bragg gratings in the fiber cores. However, these Bragg gratings exhibit a high sensitivity to temperature variation (for example, 50.1 pm/°C) [138]. HCMOF characterized by adjustable mode area and high integration can serve as an optimal platform for developing bending sensors with a low thermal sensitivity due to the low thermo-optic coefficient of the air core.

Liu *et al.* have developed a bending sensor with a low thermal sensitivity by inserting a piece of HCMOF into two segments of SMFs [23]. Bending was measured by monitoring the angle between two straight parts of HCMOF located at both sides of the bending area. The interference pattern induced by the multimode interference between HE_{11} and TE_{01} modes would shift when the sandwich-structured sensor was bent. It should be noted that lateral offset splicing was required for exciting the TE_{01} mode. The bending sensitivity was 0.28 nm/deg at 10° with a low temperature sensitivity of 0.5 pm/°C and high stability. However, compared with the highly sensitive fiber bending sensor (1.27 nm/deg) based on a hexagonal lattice MOF under a small angle range (±2°), the limited sensitivity of this device should be optimized for practical applications on small-angle measurement [139]. The basic principle of HCMOF bending sensors can be attributed to the stretched and compressed fiber material of the outer side and inner side, respectively. Hereby, the refractive index of the fiber will increase at the outer side and decrease at the inner side when the fiber is bent to a certain direction [140]. The effective optical paths of the guided modes are governed by the change of material refractive index, which results in a shift of the interference pattern. It is of great significance to improve the sensitivity of the bending measurement in terms of the advanced design of HCMOF [141, 142].

3.1 Geometry of HCMOF

The SEM cross-sectional image of the specially developed HCMOF is illustrated in Fig. 3.1. The fiber is made of pure silica via the stack-and-draw process. It is composed of a large hollow-core of 50 μm diameter surrounded by twelve crown-like air holes with a total diameter of 62.5 μm. This design is chosen for limiting the size of the cladding in order to obtain a fiber diameter (128 μm) compatible with standard SMFs in fiber-sensor configurations. The thicknesses of the strut between the hollow-core and crown-like air holes and the strut between two crown-like air holes are about 230 nm and 560 nm, respectively.

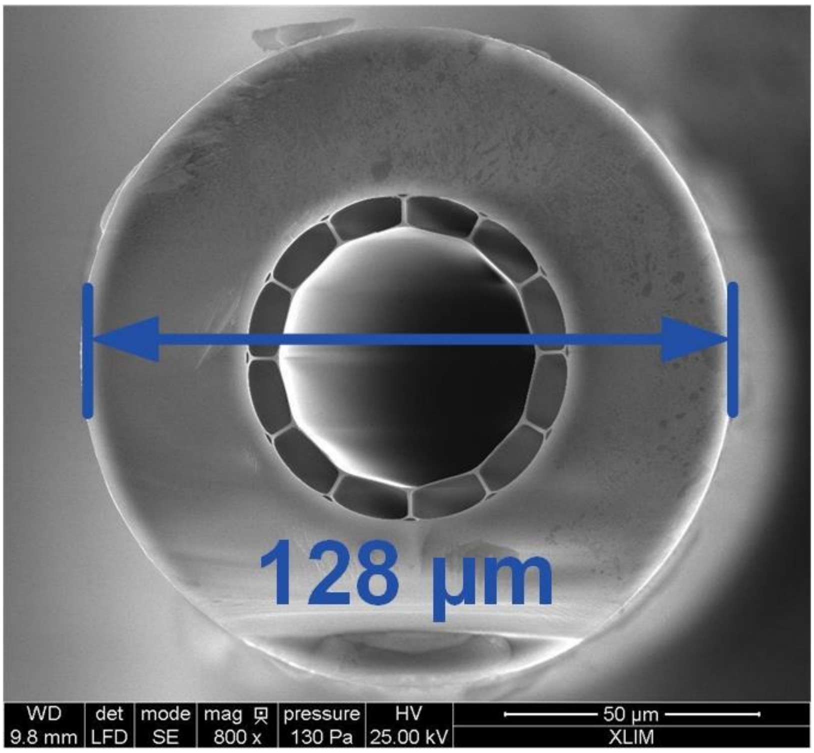

Figure 3.1 SEM image of the cross section of the HCMOF.

3.2 Fabrication of HCMOF

The HCMOF was fabricated by the stack-and-draw method in Xlim Research Institute, France, which is the commonest method for pure silica MOFs. The process could be classified into four steps.

Firstly, the silica tubes were chosen with suitable ratios of inner diameters to outer diameters based on the fiber design. Then, the silica tubes were draw into capillaries with a length of ~1 m by a fiber tower. A silica tube could be drawn into several capillaries, and these capillaries had the same ratio of inner diameter to outer diameter with the silica tube.

Secondly, all the capillaries were stacked together and placed into a large silica tube to make up the preform of our HCMOF. The schematic of the preform was shown in Fig. 3.2. The outer diameter and inner diameter of the large silica tube was 10 mm and 7 mm, respectively.

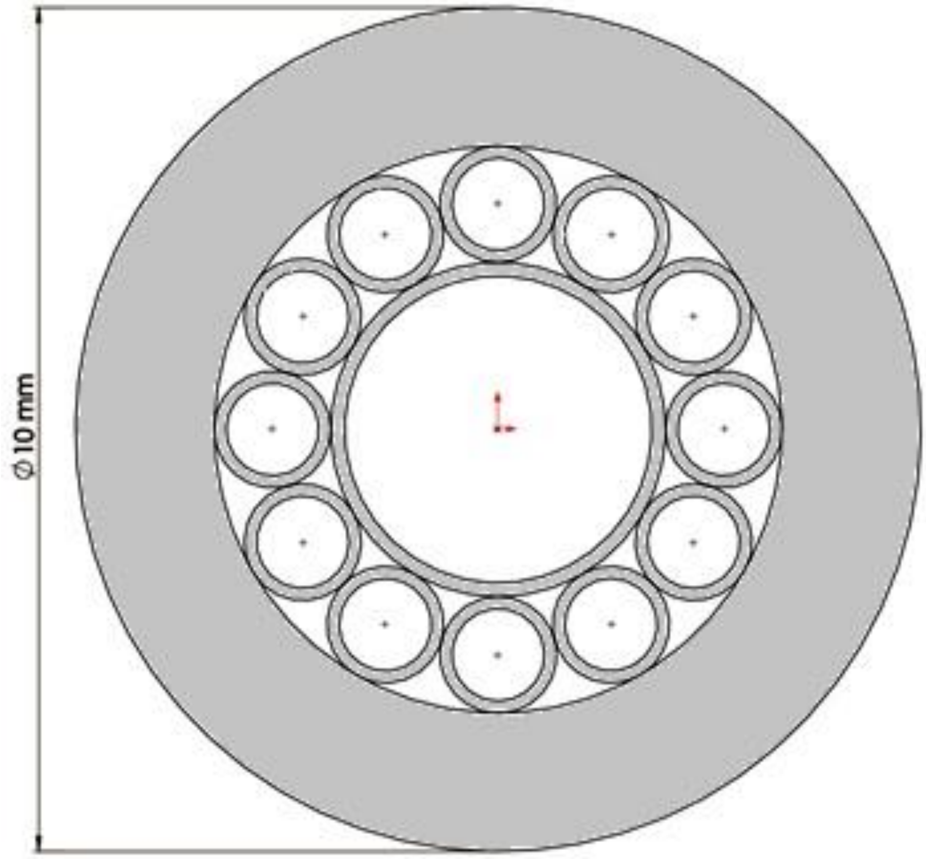

Figure 3.2 Schematic of HCMOF preform.

Thirdly, the preform was drawn into several canes with the diameter of 1.8 mm. The cross-section image of one of the canes was shown in Fig. 3.3.

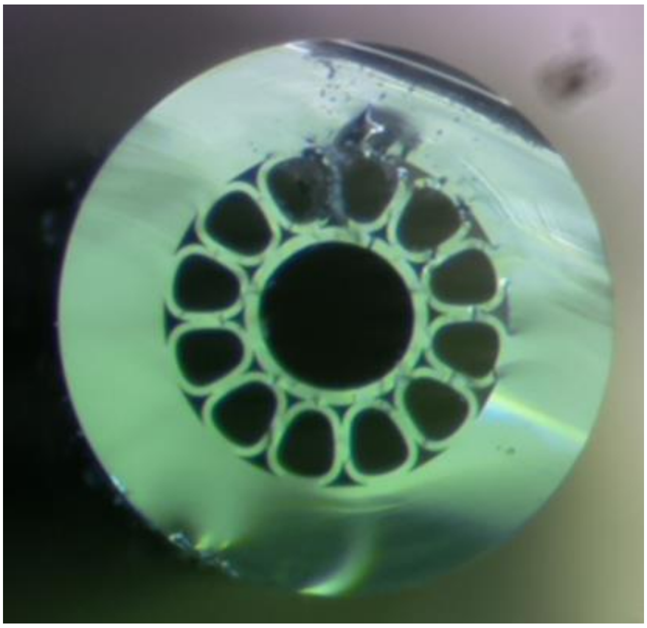

Figure 3.3 Microscope image of the cross section of a cane.

Finally, after placing the cane into a silica jacket tube with an inner and outer diameter of 2 mm and 6 mm, respectively, the cane was drawn into HCMOFs by the fiber tower.

In the third step, one end of the preform was fixed in a metal chamber with an air vent, as shown in Fig. 3.4. Then the metal chamber was placed into a holder above the high-temperature furnace. During the drawing process, vacuum was applied in the metal chamber for decreasing the gaps between capillaries. In the last step, both the cane and the jacket tube were fixed in a metal chamber with two air vents. During the process of drawing fiber, vacuum was applied to make the gap disappear between the cane and the jacket tube through one air vent, and pressure was forced into the cane for enlarging and controlling the diameter of the fiber core and further decreasing the gap between capillaries through the other air vent. Since the size of hollow core was larger than the sizes of outer 12 air holes and gaps, the pressure in the hollow core was greater than that in 12 air holes and gaps, which led to the decrease of the gaps and the increased size ratio of the hollow core to the 12 air holes.

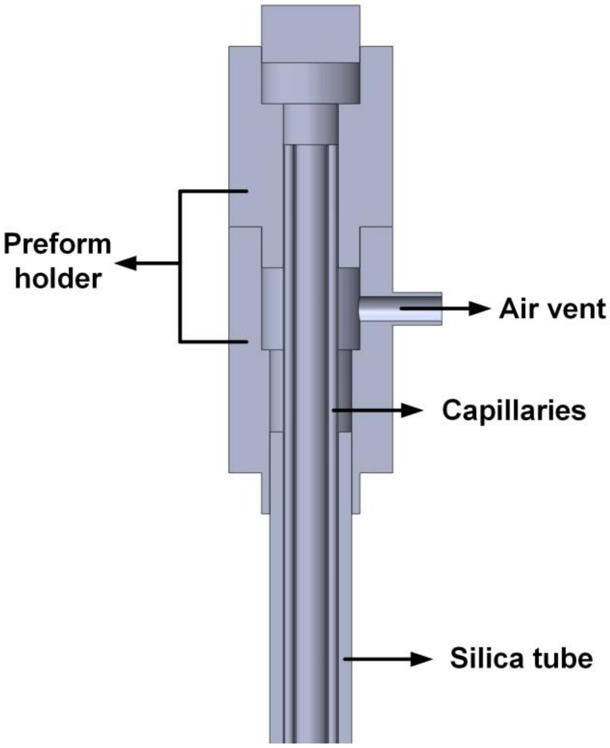

Figure 3.4 Schematic of the cross-section of the preform and holder.

During the drawing process, the capillary, cane or fiber with a proposed diameter was obtained by controlling the speed of the tube/preform/cane (feeding speed, V_{feed}) and the speed of the capillary/cane/fiber (drawing speed, V_{draw}). The corresponding speeds satisfied the following equation:

$$V_{feed}R_{seed}^{2} = V_{draw}R_{fiber}^{2} \tag{3.1}$$

where R_{seed} and R_{fiber} were the radii of the seed tube/preform/cane and the corresponding capillary/cane/fiber, respectively.

In summary, the fiber design determined the size of the silica tubes, preform, canes and fibers. The feeding speed V_{feed}, the drawing speed V_{draw}, the temperature in furnace, the vacuum and the pressure were the critical parameters during the drawing process.

3.3 Mode properties of HCMOF

The bending sensitivity of this HCMOF was analyzed by numerically simulating the ERIs of the modes propagating in the straight and bending configurations. More precisely, we have restrained our study on the interferences of the fundamental mode

(HE_{11}) to the first higher order mode TE_{01} and to mode HE_{12} which one was the first higher order mode with the same azimuthal symmetry as HE_{11} mode. The ERIs of these modes have been simulated by the finite element method (COMSOL Multiphysics 5.0) in the straight configuration. The fiber geometry was imported into the simulation model from the SEM image, and the dispersion of silica material was introduced by its Sellmeier equation. Within the wavelength range from 1350 nm to 1650 nm, these modes were propagated in the hollow-core, as illustrated by the distribution of their Poynting vector in Figs. 3.5(a)–3.5(c) and their ERIs below unity in Fig. 3.6.

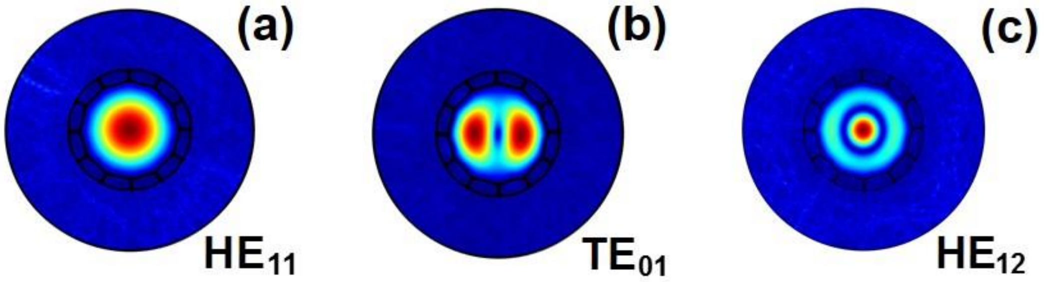

Figure 3.5 Simulated mode distributions of (a) HE_{11} mode, (b) TE_{01} mode and (c) HE_{12} mode at the wavelength of 1550 nm;

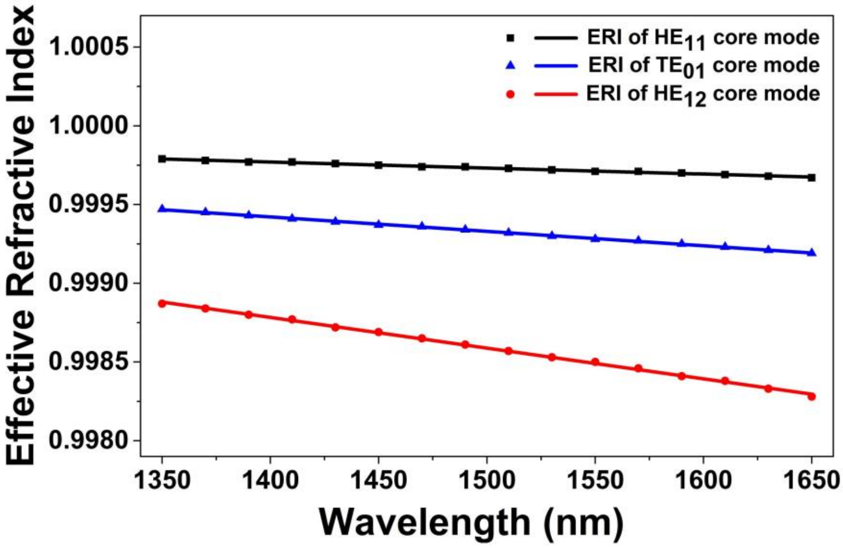

Figure 3.6 Simulated modal dispersion curves for HE_{11} mode, TE_{01} mode and HE_{12} mode.

3.4 Numerical investigation on the bending sensitivity of HCMOF based sensor

The theoretical sensing performance of this sensor (illustrated in Fig. 3.7) is obtained by simulating the interference of two modes, such as HE_{11} mode with TE_{01} or HE_{12} mode. The intensity at a given wavelength (λ) can be calculated with the following equation:

$$I = I_1 + I_2 + 2\sqrt{I_1 I_2}\cos(\Delta\varphi + \varphi_0) \tag{3.2}$$

$$\Delta\varphi = 2\pi\Delta n_{eff}L/\lambda \tag{3.3}$$

where I_1 and I_2 are the intensities of two interference modes; $\Delta\varphi$ is the phase difference between both modes; φ_0 is the initial phase difference; L is the length of the HCMOF for the proposed bending sensor and Δn_{eff} is the ERI difference between two modes. The transmission spectrum is characterized by a typical interference pattern. Transmission reaches the minimum when $\Delta\varphi+\varphi_0 = (2m+1)\pi$ (where m is an integer), which is fulfilled at specific wavelengths. These wavelength dips are calculated with the following equation:

$$\lambda = 2\pi\Delta n_{eff}L/((2m+1)\pi - \varphi_0) \tag{3.4}$$

The numerical bending sensitivity can be obtained by taking the derivative of Eq. (3.4) with respect to bending angle (θ):

$$\frac{d\lambda}{d\theta} = \frac{\lambda_0}{\Delta n_{eff0}}\frac{d(\Delta n_{eff})}{d\theta} \tag{3.5}$$

where $\lambda_0 = 2\pi\Delta n_{eff0}L/((2m+1)\pi - \varphi_0)$ is the wavelength of a minimum transmission before bending. This equation clearly emphasizes that the bending sensitivity of the sensor is only governed by the variation of the ERI difference (Δn_{eff}) between two modes.

Figure 3.7 Schematic diagram of the bending sensor.

The variation of ERI versus the bending angle was simulated starting from the conversion between the bending angle and the bending radius. The bending angle was applied on the HCMOF by keeping one-side straight and forcing the other straight part to deviate from the original line (Fig. 3.8). This deviation defined the bending angle (θ). The bending radius (R) was calculated based on the schematic shown in Fig. 3.8. We assumed that the length (L') between the intersection point of two straight lines (two parts of HCMOF) and the endpoint of the bending area was constant, 9 mm. Then the bending radius corresponded to the bending angle based on the triangle relation:

$$R = L'/tan\ (\theta/2) \tag{3.6}$$

For example, for a bending angle θ = 2º, the bending radius R was about 515.61 mm when L' = 9.00 mm. The ERIs of the mode HE_{11}, TE_{01} and HE_{12} were then calculated for different bending angles with the finite element method by applying the process of conformal mapping.

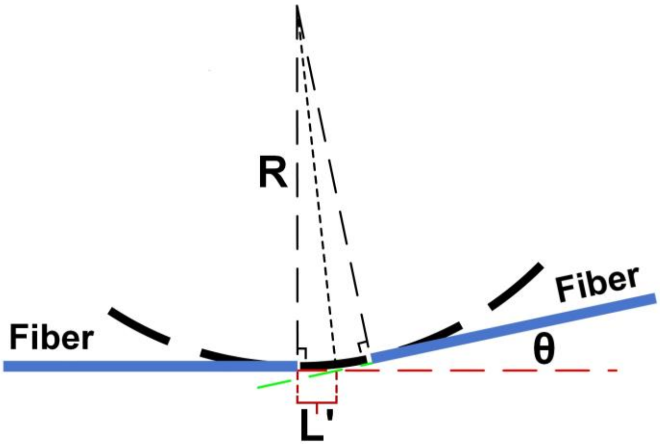

Figure 3.8 Schematic diagram of the relation between the bending radius R and the bending angle θ.

The process is to transform the circularly curved fiber into an equivalent straight fiber with modified refractive index distribution. The conformal mapping process can be expressed as follows [143-145]:

$$n'(x, y) = (1 + x/R_{eff})n(x, y) \tag{3.7}$$

where x and y axes are in the local transverse fiber plane; the fiber axis is located at $x = 0$. R_{eff} is the equivalent bending radius; $n(x,y)$ is the refractive index of the straight fiber cross-section. The silica cladding of the fiber is set as a rectangle surrounded by perfectly matched layers for absorbing the radiating modes in the simulation (Fig. 3.9). As expected, the mode field distribution shifts away from the core center when the fiber is bent.

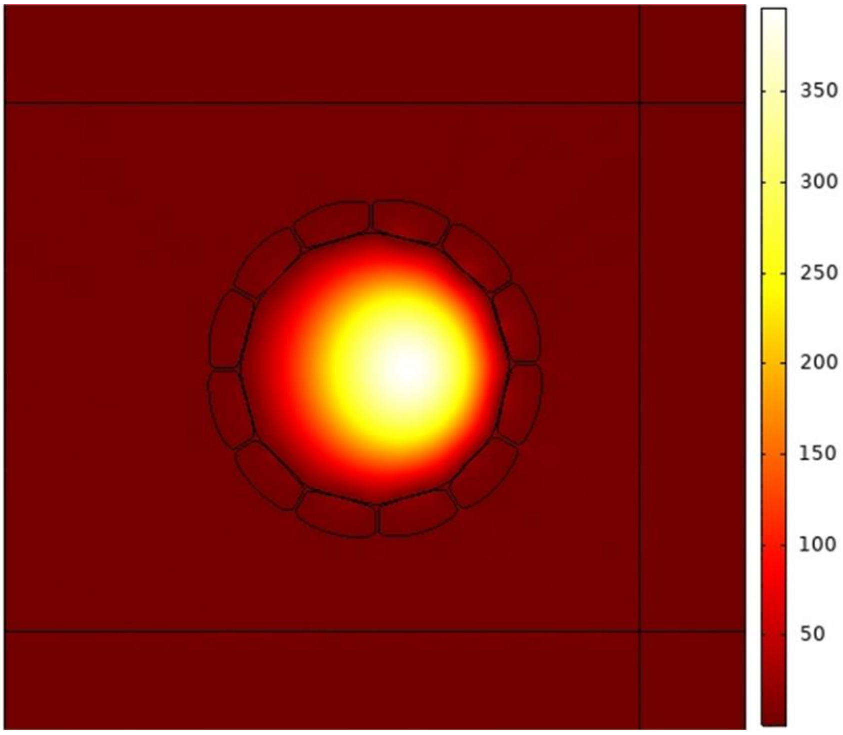

Figure 3.9 Schematic diagram of the simulation model.

We simulate the mode interference of our designed and fabricated HCMOF (with a core diameter of 50 µm) and an HCMOF with a core diameter of 35 µm similar to the one used by Liu *et al.* These simulations allow us to study the effects of the hollow core size and the coupled modes on the bending sensitivity and to compare our HCMOF with the one used by Liu *et al*.

The normalized interference spectra are calculated with the Eqs. (3.2) and (3.3), and by applying the assumption of $\varphi_0 = 0$, $I_1 = I_2 = 0.25$ (the input power was equally coupled to both modes). As illustrated in Figs. 3.10-3.12, the spectra shift to shorter wavelengths with the increase of the bending angle. This shift is not linear and increases with the bending angle. The wavelength shifts of the dip in the interference spectra are plotted in Fig. 3.13 versus the bending angle from 2º to 14º. The bending sensitivity of each wavelength dip (Fig. 3.14) is then obtained from the derivative of the wavelength shift. The shift of the interference spectrum of HE_{11}-TE_{01} modes is clearly larger for a hollow-core diameter of 50 µm than of

35 µm (Fig. 3.10 and Fig. 3.11) with a bending sensitivity slope of 0.168 and 0.024, respectively. For example, this leads to a bending sensitivity improvement of 5 times for the bending angle of 10º. The comparison of the interference spectra HE_{11}-TE_{01} and HE_{11}-HE_{12}, for a hollow-core diameter of 50 µm, reveals a higher bending sensitivity of the mode TE_{01} with a slope of 0.168 than the mode HE_{12} (with a slope of 0.112), corresponding to the bending sensitivity improvement of 1.5 times for the bending angle of 10°. The comparison of all these simulations demonstrates that the effect of the hollow core size on the bending sensitivity is larger than the difference between the coupled modes of HE_{11}-TE_{01} and HE_{11}-HE_{12}. These results emphasize the advantage of our fiber design that enables the fabrication of large hollow-core for improving the bending sensitivity of the HCMOF.

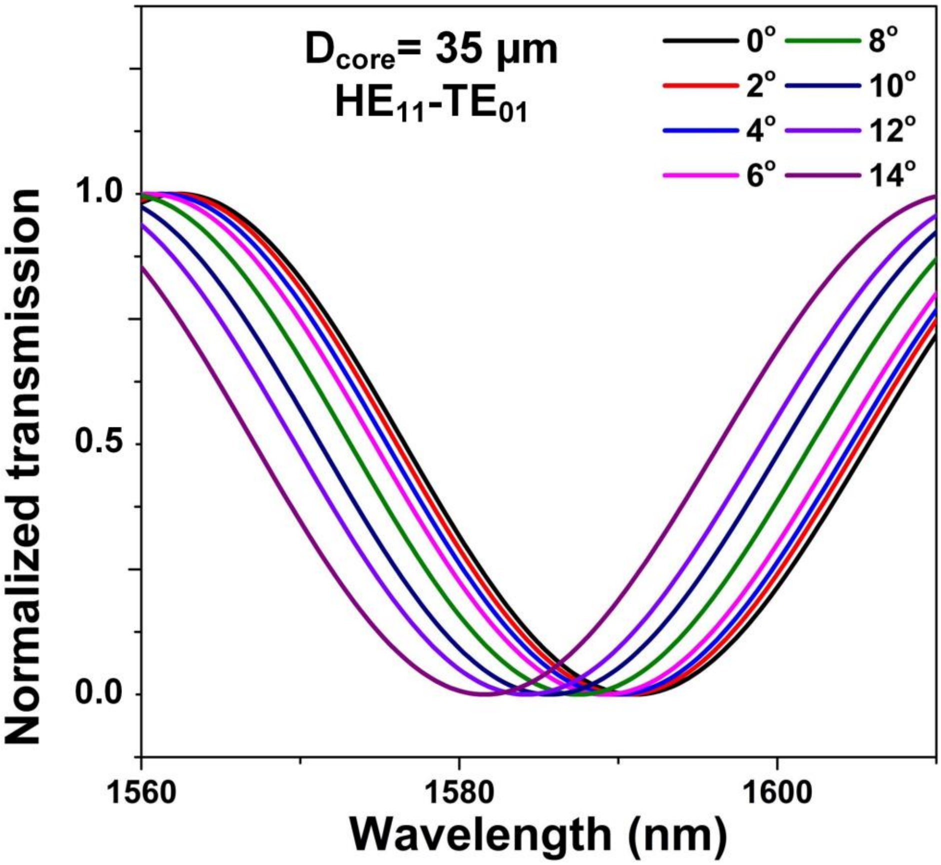

Figure 3.10 Simulated spectrum of HE_{11}-TE_{01} modes of 35-µm-diameter HCMOF.

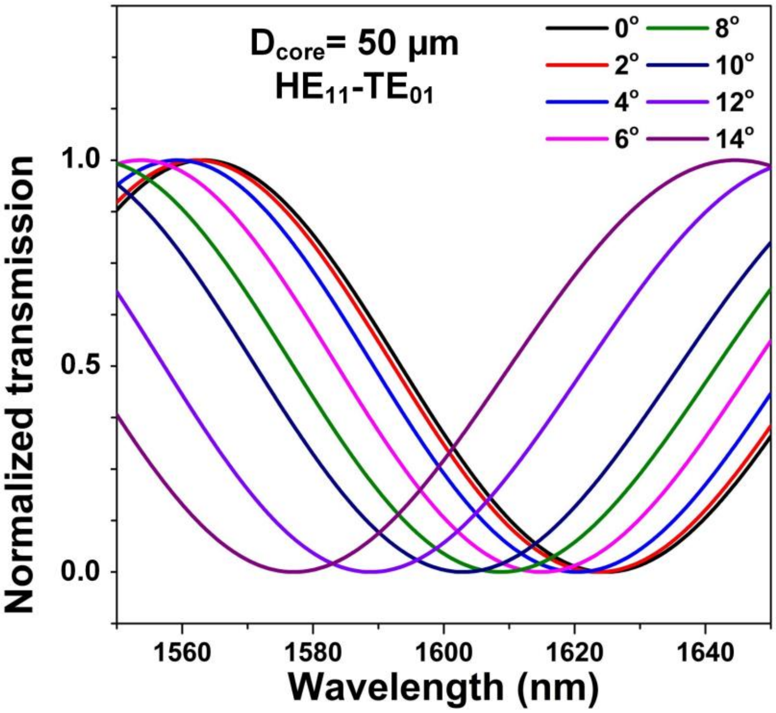

Figure 3.11 Simulated spectrum of HE_{11}-TE_{01} modes of 50-µm-diameter HCMOF.

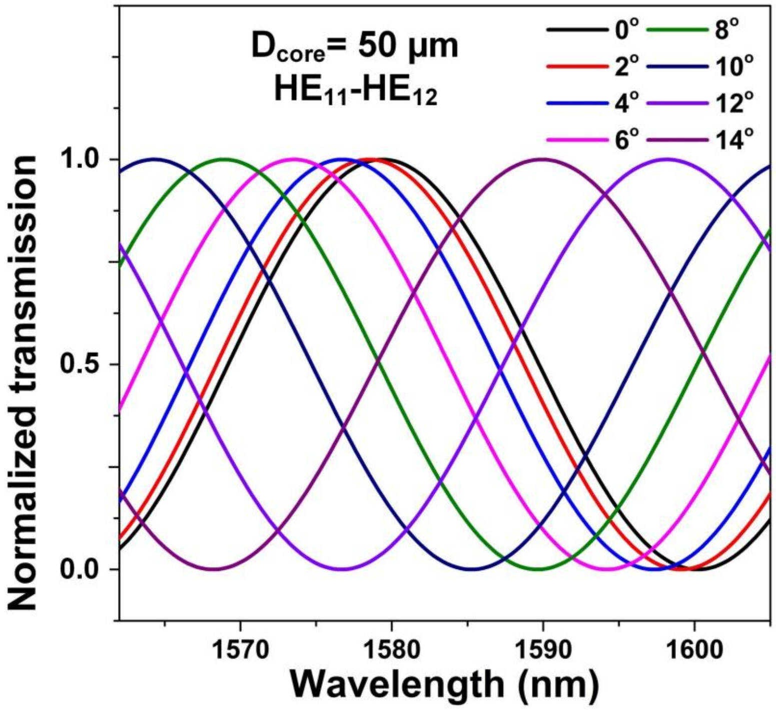

Figure 3.12 Simulated spectrum of HE_{11}-HE_{12} modes of 50-µm-diameter HCMOF.

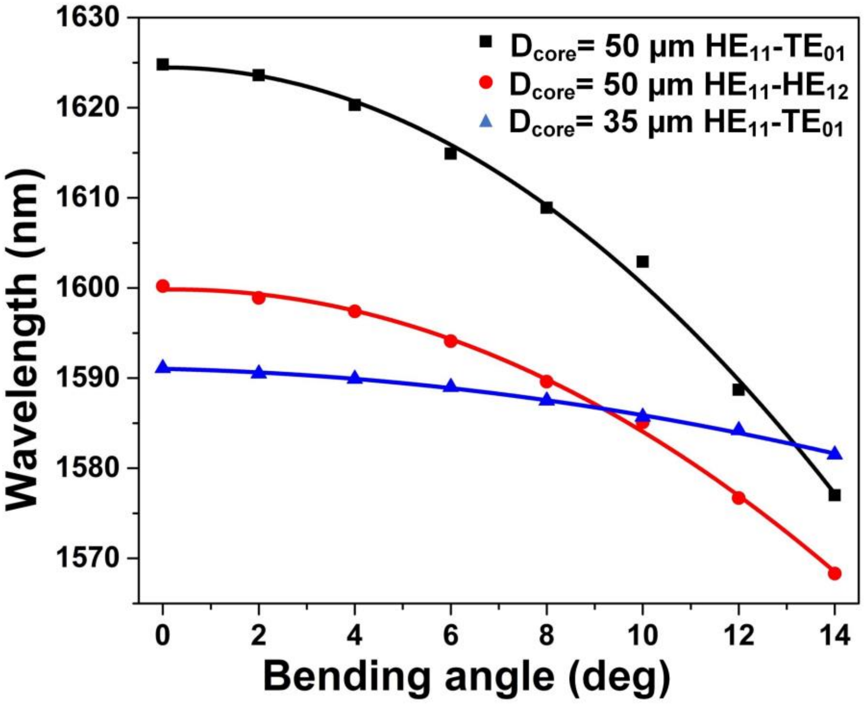

Figure 3.13 Simulated wavelength shift of three kinds of interferences.

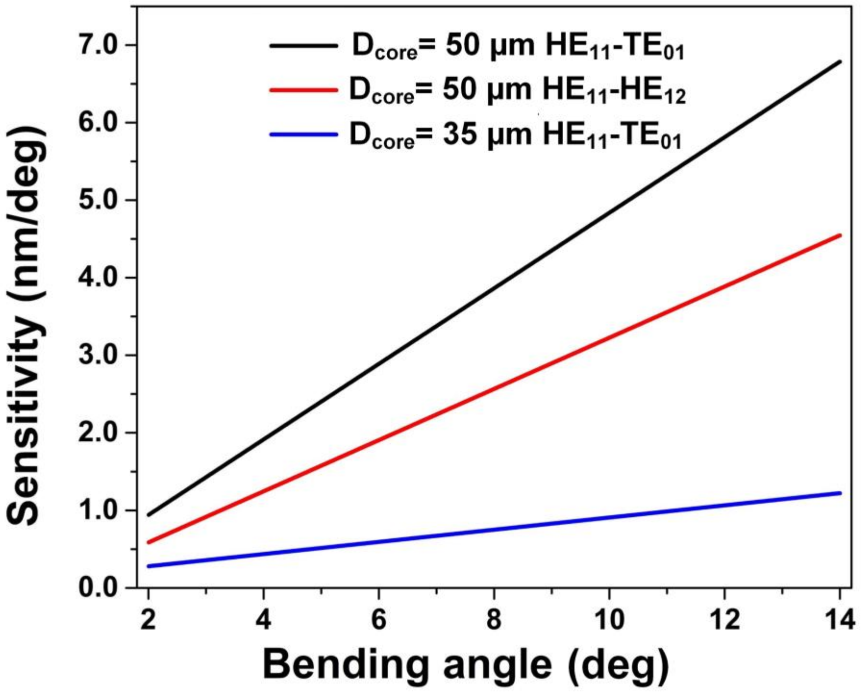

Figure 3.14 Simulated bending sensitivity of three kinds of interferences.

3.5 Experimental results and discussions

We fabricated three sensor samples composed of a section of HCMOF with L = 1.0 cm, L = 2.5 cm and L = 5.0 cm, respectively, spliced between two pieces of standard SMFs. The samples were spliced by a Fujikura 70S fusion splicer with central alignment. The arc power and arc time were set to -60 bits and 600 ms, respectively, for a robust splicing point without collapse and bubbles. The transmission spectra of these samples plotted in Fig. 3.15(a) were measured by utilizing a broadband light source (Infinon Research 1RBL-11111-F) and an Optical Spectrum Analyzer (OSA, Yokogawa AQ6370c). The FSRs of these spectra are $\Delta\lambda$ = 175.1 nm, 60.9 nm and 34.3 nm for L = 1.0 cm, L = 2.5 cm and L = 5.0 cm, respectively. From these values, we can calculate the ERI difference (Δn_{eff}) through the following equation [36]:

$$\Delta n_{eff} = \lambda^2/(\Delta\lambda \cdot L) \tag{3.8}$$

where λ is the central wavelength between two dips. The calculation results of Δn_{eff} are all around 1.4×10^{-3}. This value is close to the simulated $\Delta n_{eff} = 1.2 \times 10^{-3}$ of the coupling between HE_{11} and HE_{12} modes at 1550 nm (Fig. 3.6). To confirm the coupling, we further measured the near-field distribution of the light intensity at the output of the 5.0-cm-long HCMOF. A tunable laser (Ando AQ4321D) and a camera (Spiricon SP1550M) were used to measure the mode-field distribution at 1541 nm and 1556 nm, where these two wavelengths were located at the maximum and the minimum of transmission, respectively (as indicated in Fig. 3.15(a)). The mode distribution at 1541 nm corresponds to the HE_{11} mode (Fig. 3.15(b)), while the mode distribution at 1556 nm (at a transmission dip) is similar to the one of the HE_{12} mode (Fig. 3.15(c)). These results reveal that the multimode interference between HE_{11} and HE_{12} modes dominates the sensing mechanism of our fiber sensor. The asymmetric mode distribution in Fig. 3.15(c) should be induced by the V-groove fiber holder that is used to fix the end face of the fiber in front of the camera, where the pressure from the V-groove fiber holder leads to the deformation of the fiber and further results in the asymmetric mode distribution.

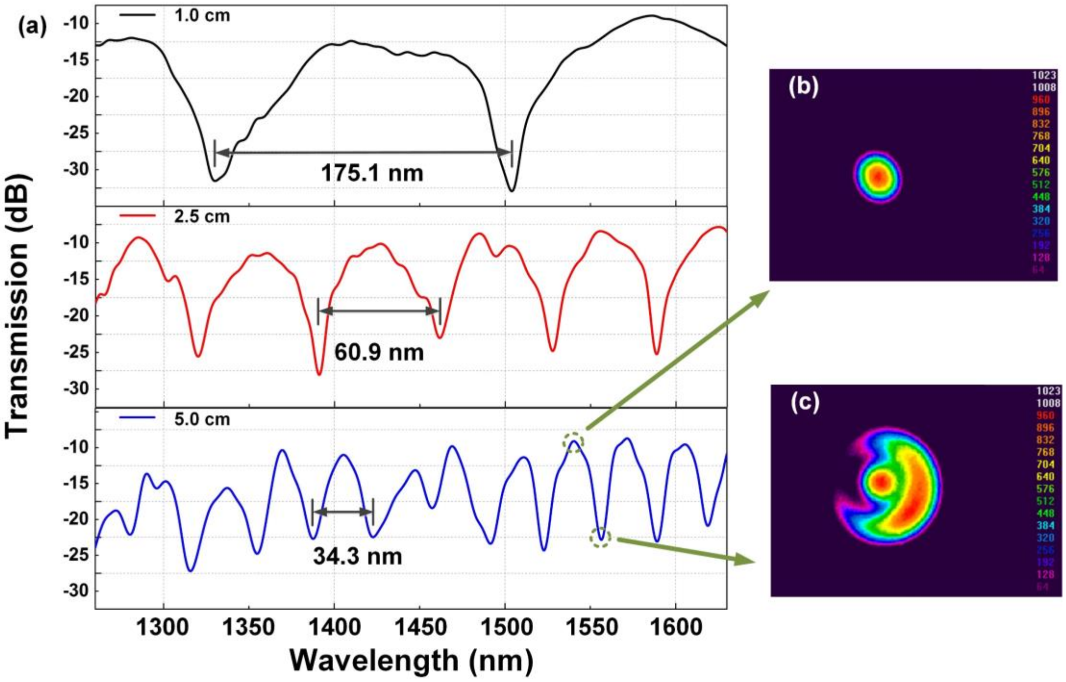

Figure 3.15 (a) Transmission spectra of the bending sensor with a 1.0-cm, 2.5-cm and 5.0-cm long HCMOF, respectively; mode field distribution with 5.0-cm-long HCMOF at (b) 1541 m and (c) 1556 nm, respectively.

The sensor with a 5.0-cm-long HCMOF was used for the bending sensitivity measurement. The center of the HCMOF was held on a fixed stage. The other part (including a portion of the SMF) was filled into a capillary tube. The capillary was attached on a holder that could be moved following a circle arc for applying a bending angle (Fig. 3.16). The capillary was used for leaving the fiber straight without mechanical strain when it was bent. A protractor ruler was used to measure the bending angle. The different bends were applied with a step of 2°, in the vertical plane (α) and then in the horizontal plane (β), as shown in Fig. 3.16. The transmission spectra of the fiber sensor were measured with the broadband light source and the OSA.

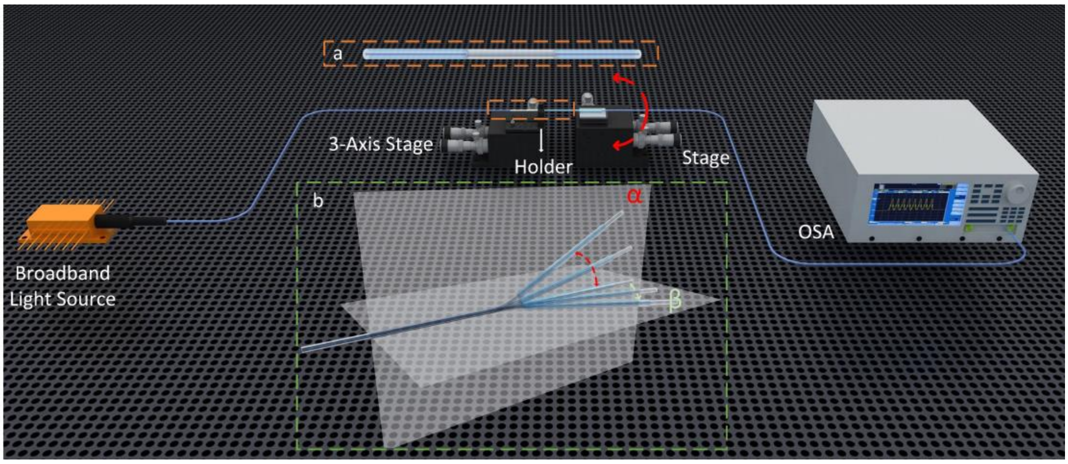

Figure 3.16 Schematic diagram of the experimental setup; (Inset a) schematic structure of the bending sensor; (Inset b) schematic illustration of the bending angle measurement.

As expected from the simulation results, the transmission spectrum shifts to shorter wavelengths when the bending angle increases, as shown in Fig. 3.17. The fiber sensor is bent from 0º to both -14º and +14º in the horizontal plane and then in the vertical plane. Indeed, the measurement range is limited by the special structure of our HCMOF. The large-hollow-core fiber is more fragile than a small-hollow-core fiber with an increasing bending angle. But, we can achieve an increased bending sensitivity by using the large-hollow-core fiber. Hence, there is a tradeoff between the bending sensitivity and the measurement dynamic range. For practical applications, we can optimize our fiber design to satisfy different requirements of the bending measurements. The wavelength of a dip is measured and plotted for each bending angle in the Fig. 3.18(a). For each bending angle, the position of the dip wavelength is almost identical in both orthogonal planes and also in both opposite directions. These results reveal the direction-independent performance of this bending sensor. This property is inherent due to the circular symmetry of the HE_{11} and HE_{12} modes.

The positions of the dip wavelength have been approximatively fitted with a two-orders polynomial fit (Fig. 3.18(a)). It is worth noting that both curves (for vertical and horizontal planes) are well superposed. The bending sensitivity of the wavelength dip in orthogonal planes is then obtained from the derivative of these curves (Fig. 3.18(b)), leading to linear curves with a directional coefficient of 0.204 nm/deg^2. The sensitivity of our bending sensor is around 0.8 nm/deg at a bending angle of ± 4°, and up to 2.8 nm/deg at a bending angle of ± 14°. This sensitivity is about 10 times higher than the one reported by Liu *et al*. in this range of bending angle [23]. The measurement resolution of the sensor, limited by the resolution (0.2 nm) of the OSA, is 0.25° at ±4°.

The deviation between the actual measured data and the fitting curve, especially at 6° and 10°, is mainly induced by the experimental error and fitting error. Since there is a relation between the bending angle and the bending radius as indicated in Eq. 3.6, the resonant wavelengths will not exactly follow the quadratic fit with the bending angle increasing. Even though the quadratic fit cannot perfectly match the measured data, a numerical compensation can be utilized to correct the bending angle in the practical measurement based on the good repeatability of our sensor.

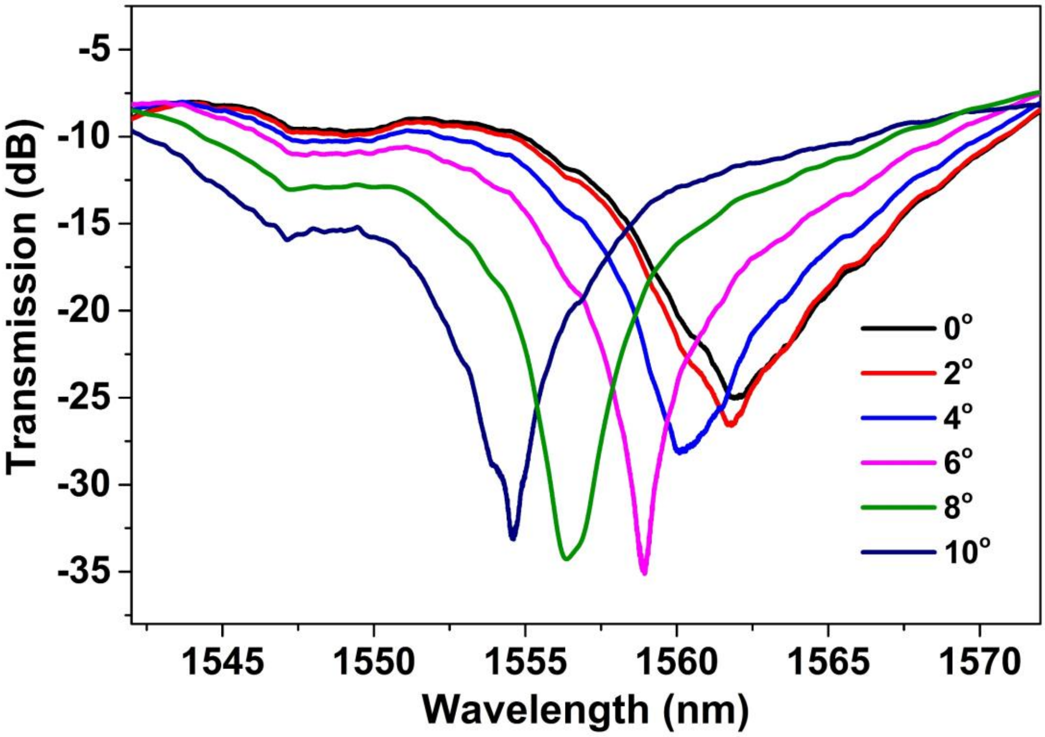

Figure 3.17 Spectral evolution with the bending angle increase from 0° to 10° at horizontal plane.

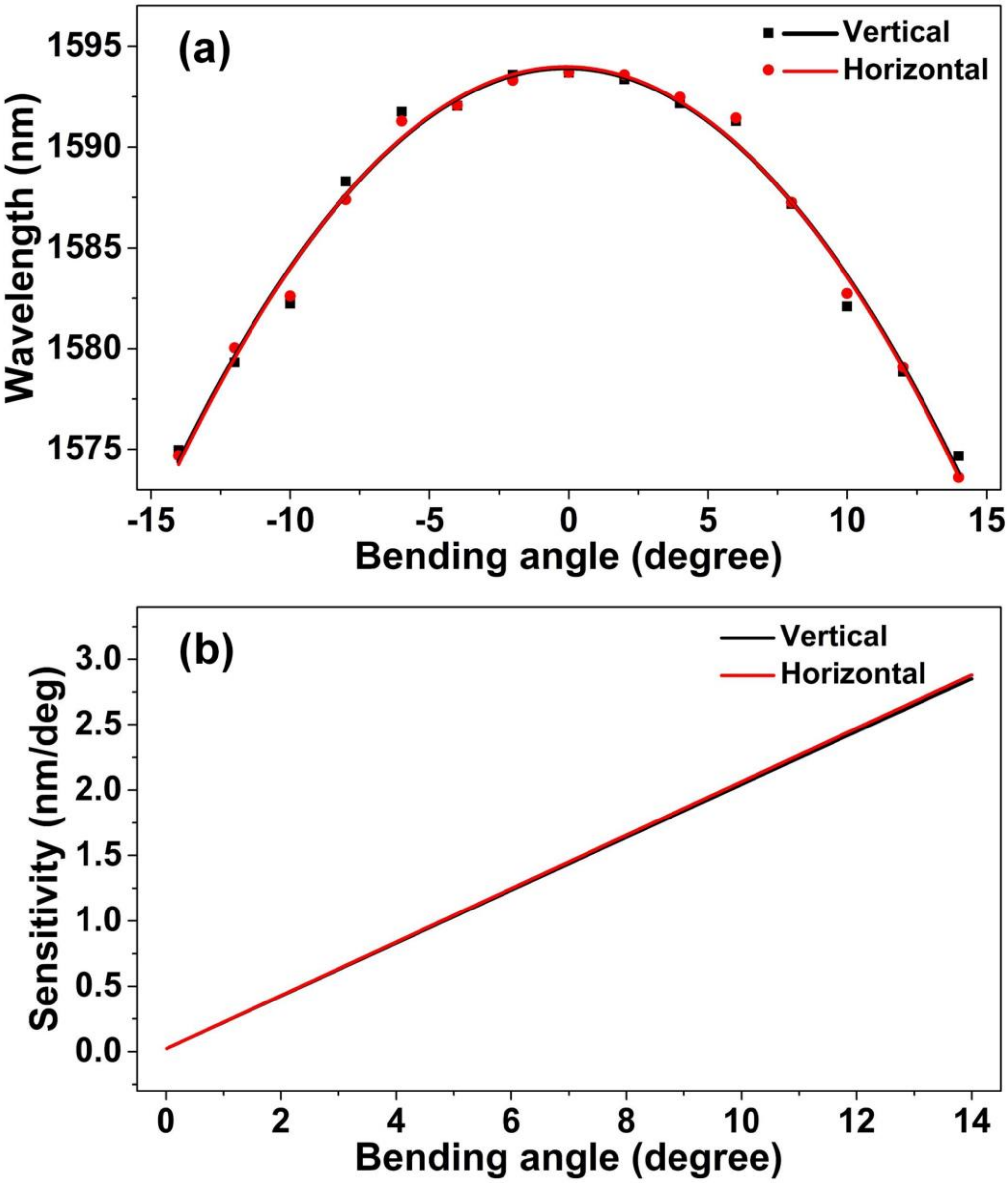

Figure 3.18 (a) Bending angle response at two orthogonal planes; (b) linear sensitivity variations from 0° to 14° at two orthogonal planes.

The reversibility of the sensor is also investigated by varying the bending angle from 0° to +14º and back to 0º. The positions of the dip wavelength are plotted in Fig. 3.19(a). These dips are almost located at identical wavelengths in both cases (when the bending angle increases or decreases), and the bending sensitivities of both cases are matched well as shown in Fig. 3.19(b), which demonstrates the good reversibility of our sensor. The shifting trend of the dip wavelengths versus bending angles (Fig. 3.18(a) and Fig. 3.19(a)) matches well with the simulated curve shown in Fig. 3.13.

The results indicate that the nonlinear variation of the mode interference in this HCMOF with different bending angles is inherent, and the reliability of experimental results is demonstrated. Compared with the electrical based bend sensor, our HCMOF based optical sensor possesses the advantages of electromagnetic immunity, high stability, compact size and low cost.

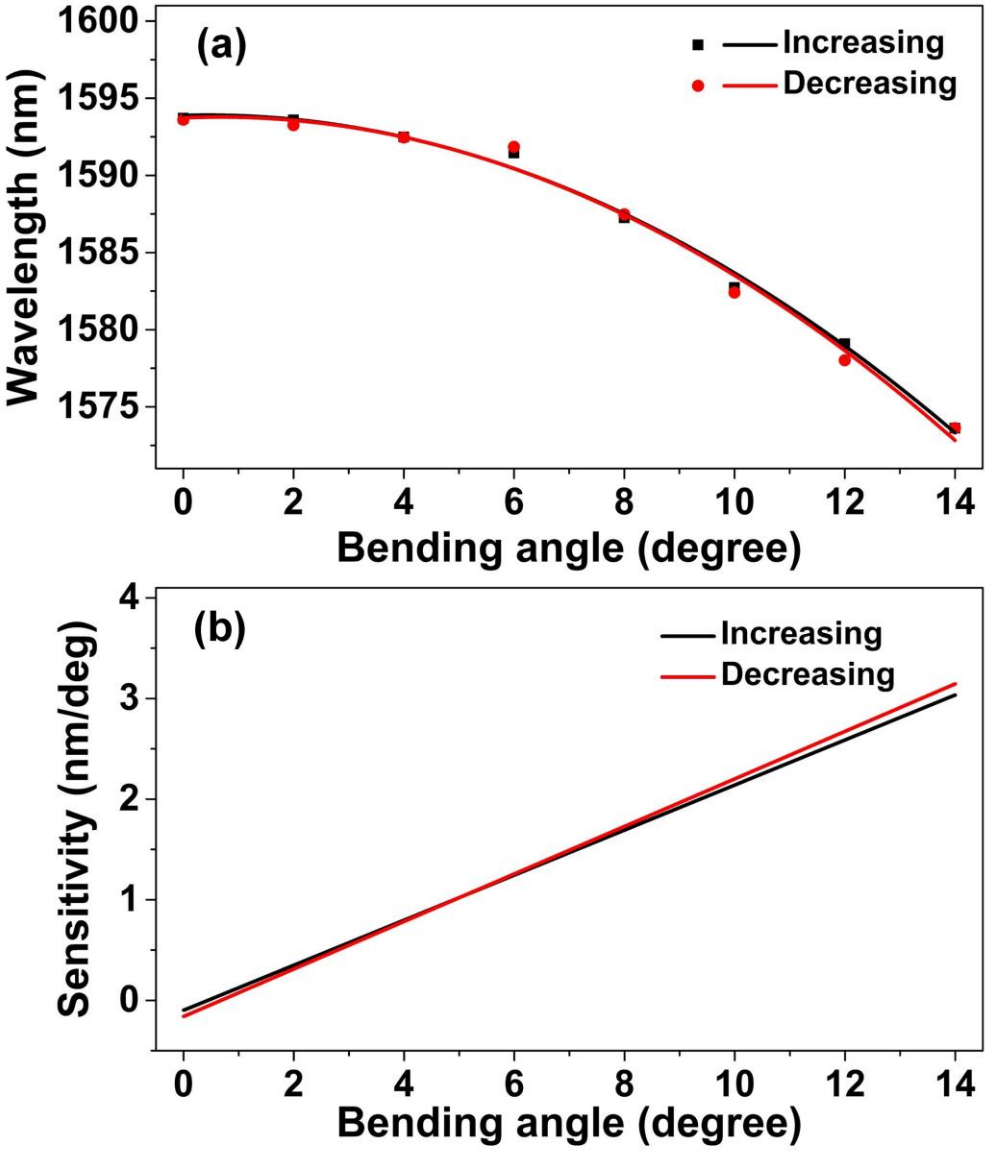

Figure 3.19 (a) Reversibility measurement of the bending sensor; (b) linear sensitivity variations for reversibility measurement.

The thermal sensitivity of our fiber sensor was measured by inserting it into a furnace (MTI GSL-1500x). The fiber was kept straight with a tiny tension in the furnace. The temperature of the furnace was increased from 18 ºC to 1000 ºC. The temperature precision of this furnace was 1 ºC. The shift of the transmission spectrum was recorded with the broadband source and the OSA. The spectrum slightly shifts to longer wavelengths with the temperature, as illustrated in Fig. 3.20 by the evolution of two wavelength dips. Both wavelength dips follow a linear shift with a directional coefficient of about 2.5 pm/ºC. From these measurements, we can calculate a temperature cross-sensitivity of 0.0031 deg/ºC and 0.0009 deg/ºC for a bending angle of ± 4° and ± 14°, respectively. The low temperature cross-sensitivity confirms the advantage of this HCMOF for developing bending sensors.

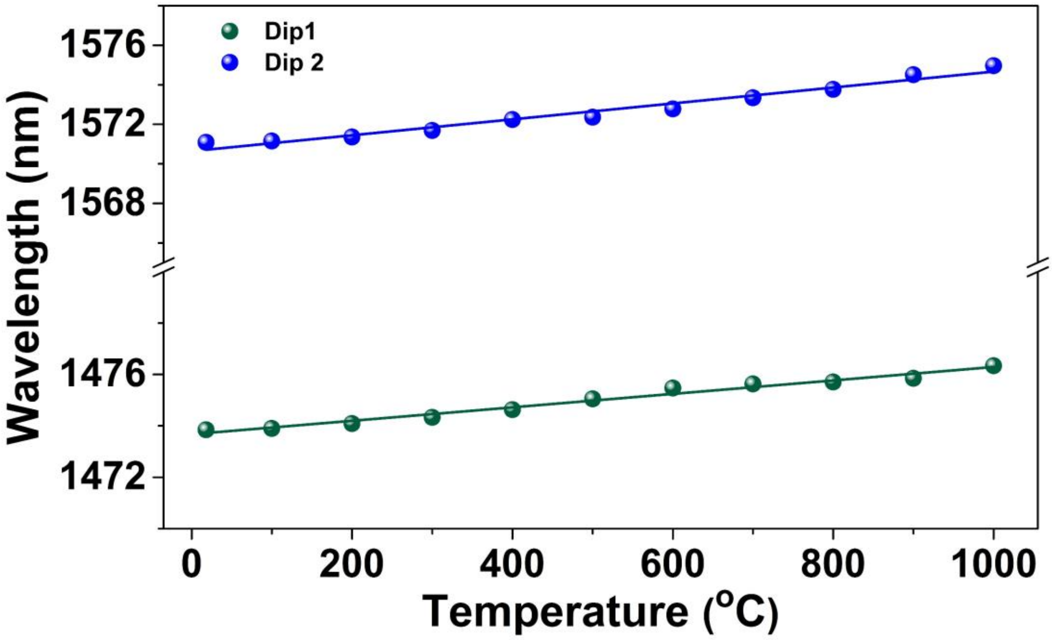

Figure 3.20 Thermal responses of dip 1 (green) and dip 2 (blue) with a 5.0-cm-length HCMOF.

3.6 Summary

In conclusion, we investigate the bending measurement based on a specially designed HCMOF with a large hollow core and small cladding air holes. This fiber design enables the fiber diameter around 125 μm for easier integration in fiber sensor configurations. Numerical simulation reveals that the bending sensitivity is mainly determined by the diameter of the hollow core and also depends on the coupled modes. Experimentally, the sensing device is fabricated by sandwiching the HCMOF between two segments of SMFs. Compared with the previous work in [23], the bending sensitivity (2.8 nm/deg at 14°) is improved 10 times without orientation dependency by enlarging the mode field of the HCMOF. Furthermore, based on the simulation results, the bending sensitivity can be improved by coupling HE_{11} mode to TE_{01} mode in our HCMOF with offset splicing, but at the expense of low robustness. Additionally, the low thermal sensitivity of 2.5 pm/°C from 18 °C to 1000 °C is also validated, which addresses the critical issue of thermal crosstalk for the highly sensitive bending measurement. Our research results unveil the performance optimization of the HCMOF bending sensors.

Chapter 4 Strain Sensitivity Enhancement Based on Periodic Deformation in HCMOF

Optical fiber MZIs has been widely studied in the field of sensing application. However, the strain sensitivity of optical fiber MZIs is generally low due to the small elasto-optical coefficient of silica. In this chapter, we propose and demonstrate a method to modulate the guided modes in the MZI based on our HCMOF by fabricating periodical deformations. Specifically, periodical deformations reduce the extinction ratio of the transmission spectrum. Further, the axial tension modulates these periodical deformations, leading to the enhanced strain sensitivity in comparison to the configuration without deformations. In our experiment, the strain response from 0-1000 με is obtained with a sensitivity of 0.00334 dB/με corresponding to an improvement of 5 times compared with a sensor based on the same HCMOF without deformations.

4.1 Background

Strain sensors have widespread applications in many fields, such as mechanical engineering, earthquake monitoring and structural health monitoring on aircraft, skyscrapers, bridges and railways. Compared with other types of strain sensors, optical fiber strain sensors possess a number of unique advantages, such as immunity to electromagnetic interference, small size, and remote monitoring. Several types of schemes have been utilized to demonstrate fiber based strain sensors, including FBG [146, 147], LPFG [148, 149], FPI [150, 151] and MZI [152-155]. However, most of FBGs suffer from temperature crosstalk, and the fabrication of FBG usually requires complex components such as a phase mask, a UV laser and an optical system. LPFG based strain sensors have a low strain sensitivity. Some FPIs based on an air cavity or cascaded air cavities own high strain sensitivity, but due to the specially fabricated air cavities, these sensors are fragile. Meanwhile, the size of the air cavities is difficult to control.

In past few years, optical fiber based MZIs have been widely studied for sensing applications via various configurations, for instance, a tapered fiber MZI for refractive index and temperature measurements [156], a microfiber MZI based on an air cavity for strain sensing [157], an in-line MZI based on a twin core photonic crystal fiber for bending measurement [109], an optical fiber MZI based on cascaded microcavities for high-temperature sensing [158] and an all-fiber MZI based on a singlemode-multimode-thinned-singlemode fiber structure for multi-parameter sensing [159]. The operation principle of all these sensors is to excite multiple modes through mode field mismatch in order to obtain in-line Mach–Zehnder interference. These sensors are robust and easy-to-fabricate. However, due to the small elasto-optical coefficient of silica, the strain sensitivity of MZI based optical fiber sensors is generally less than 0.003 dB/με.

4.2 Design and construction of strain sensor

The SEM cross-sectional images of our HCMOF are shown in Fig. 4.1(a)-(b). The periodical deformations were fabricated by electric arc discharge based on a commercial splicer (Fujikura, FSM-100P+) with manual mode. Firstly, a segment of 30-mm-long HCMOF was sandwiched into two segments of SMFs by the splicer for monitoring the output spectrum of the sensor in real-time during the fabrication process. Secondly, the segment of HCMOF in the sample was fixed straight by two holders of FSM-100P+. The distance between the two holders was 16 mm. Thirdly, two electric arcs were activated with a power of 300 bits and a duration time of 0.25 s, and then a small deformation was fabricated at the region of the arc discharge. After the fabrication of the first deformation, both holders were simultaneously moved 0.3 mm to the left. Finally, after the repetitions of discharges and translations, 30 periodical deformations were built in the HCMOF with a total length of 8.7 mm. The microscope image of several periodical deformations was shown in Fig. 4.1(c) and the SEM images at the cross-section A-A of the sample were illustrated in Fig. 4.1(d)-4.1(e). Red arrows in Fig. 4.1(c) revealed the discharge positions. The deformation induced by the discharge led to the contraction of the HCMOF, including hollow core and air holes, compared with the Fig. 4.1(b). Besides, the symmetry of air holes was slightly broken at the deformation area. In Fig. 4.1(e), air holes located in the bottom were larger than those at the top. Meanwhile, the small holes located at the outside of the air cladding almost disappeared.

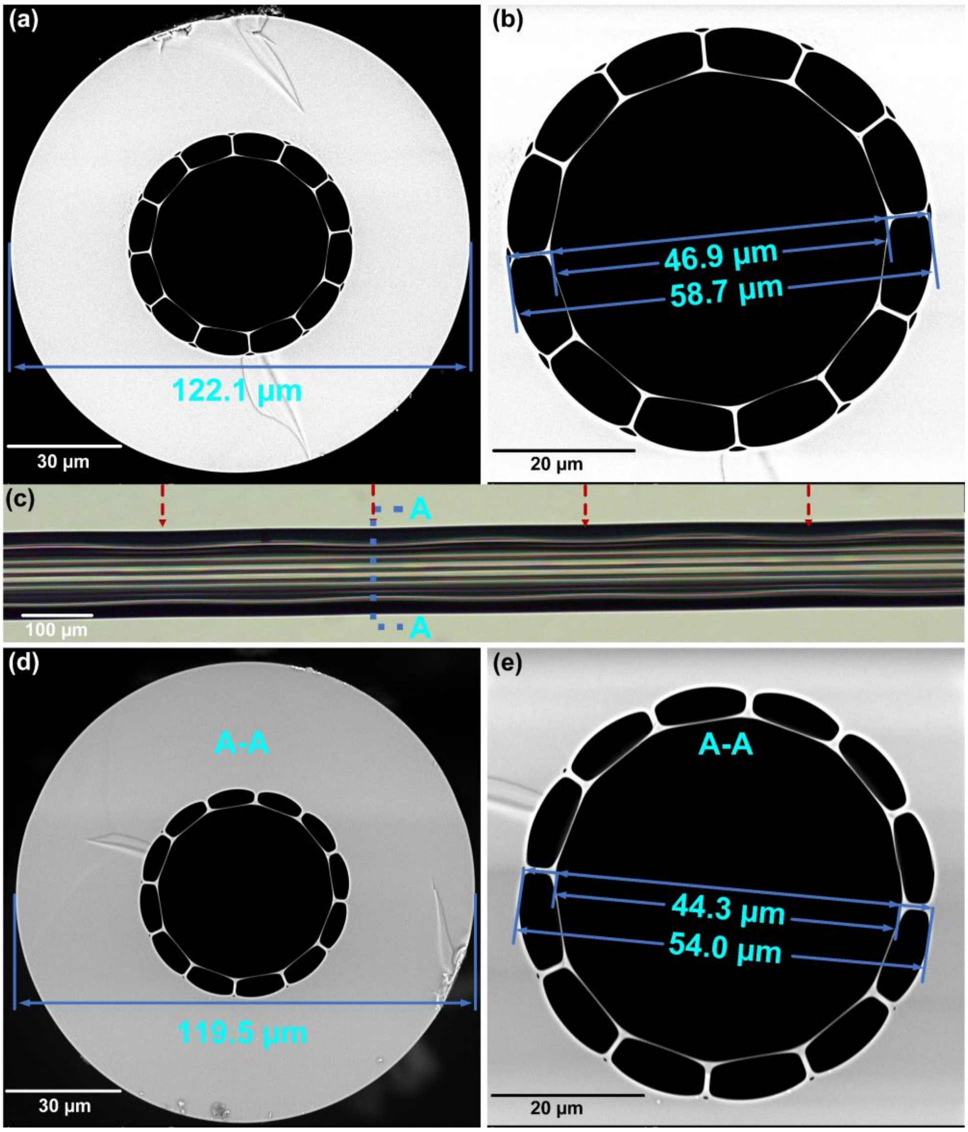

Figure 4.1 (a) SEM image of the cross-section of the HCMOF without deformation, (b) SEM image of the hollow core and air cladding of the HCMOF without deformation, (c) microscope image of four periodical deformations, (d) SEM image of the cross-section A-A of the HCMOF at deformation area, and (e) SEM image of the hollow core and air cladding of the HCMOF at deformation area.

When the two electric arcs discharge, the temperature gradually decreases from the tips to the midpoint along the axis of two electrodes. In addition, due to the relatively slow heat conduction in the air holes, the heat conduction from the outer silica cladding to the inner air hole region is slow. Hence, the temperature in the area of air holes is lower than that in the silica cladding during a very short discharge period. When the outer silica of the HCMOF is heated to more than 1670 ºC, the softening point of silica, the surface tension will lead to the slight contraction of the HCMOF. The lower temperature in the area of air holes, compared with the outer silica cladding, maintains the original structure of large air holes.

4.3 Operation principle and numerical analysis

In the previous work, we demonstrated that an in-line MZI could be realized by splicing the HCMOF into two segments of SMFs with central alignment [160]. The interference in the MZI was caused by HE_{11} and HE_{12} modes. For investigating the difference of guided modes at the deformation area and the non-deformation area, the fiber geometries at the cross-section A-A and the cross-section of non-deformation were imported into COMSOL simulation model from their SEM images, respectively. Sellmeier equation was applied to calculate the dispersion curve of silica material. Both HE_{11} mode and HE_{12} mode could propagate at the deformation area and non-deformation area, as shown by the distribution of their Poynting vectors in Figs. 4.2(a)–4.2(b). As the yellow lines were shown in Fig. 4.2(b), the symmetry of field distribution of HE_{12} mode at the deformation area was slightly broken compared with the field distribution of HE_{12} mode in Fig. 4.2(a), which was consistent with the symmetry variation in Fig. 4.1. Their ERI curves were illustrated in Fig. 4.3 within the wavelength range from 1250 nm to 1650 nm.

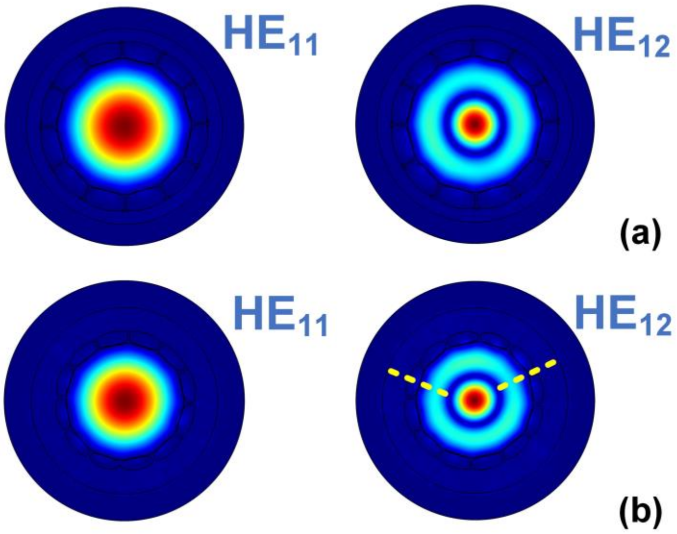

Figure 4.2 (a) Simulated mode field distribution of HE_{11} mode and HE_{12} mode without deformation, (b) simulated mode field distribution of HE_{11} mode and HE_{12} mode at a deformation area.

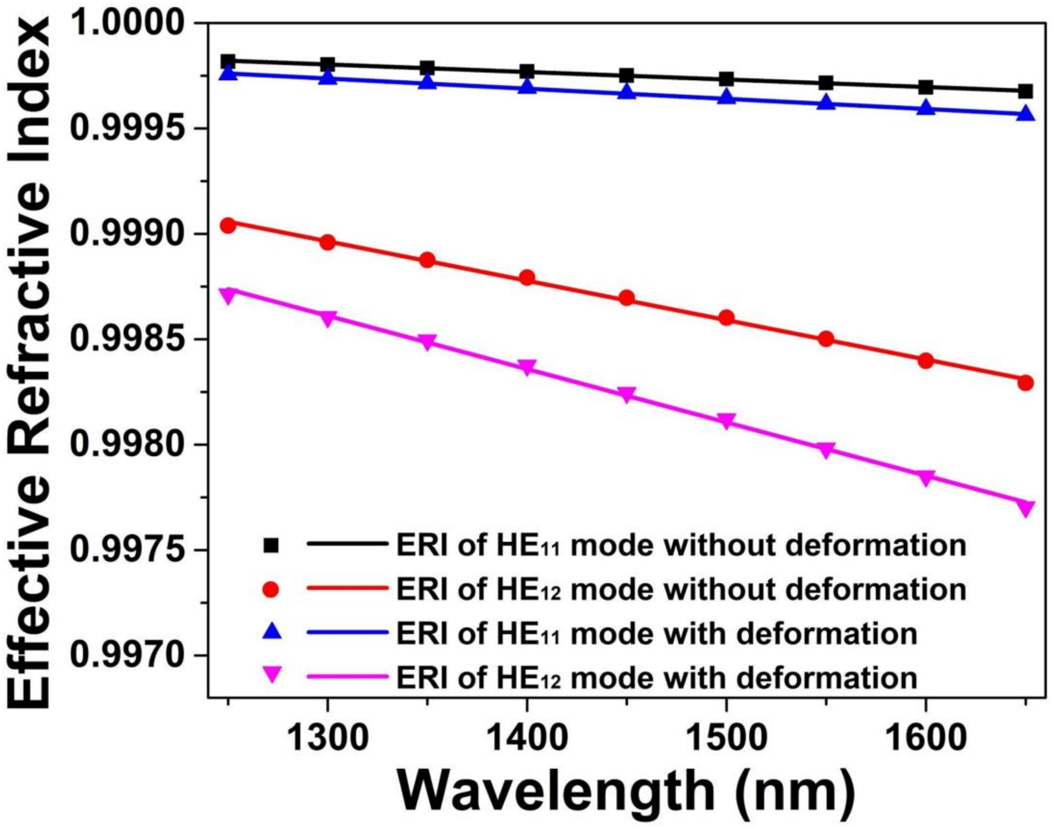

Figure 4.3 Simulated dispersion curves of HE_{11} mode and HE_{12} mode without deformation and with deformation, respectively.

As expected, the ERI of HE_{11} mode was higher than that of HE_{12} mode for both the deformation area and non-deformation area, and all ERIs became smaller with the wavelength increase. Furthermore, the ERIs of HE_{11} mode for both areas were close with each other, but the ERI of HE_{12} mode for the deformation area was obviously smaller than that for the non-deformation area. Meanwhile, the power ratios between HE_{12} mode and HE_{11} mode were obtained by calculating their Poynting vector S based on the simulation in COMSOL. Through exporting the electric field vector E and the magnetic field vector H from the simulation model, Poynting vector S was calculated according to the equation $S=E\times H$. Accordingly, the power ratios between HE_{12} and HE_{11} modes were around 0.147 and 0.268 for the deformation area and non-deformation area, respectively. When HE_{11} and HE_{12} modes were excited and propagated along the hollow core, the mode interference would occur. The transmission spectrum could be achieved by the following equation:

$$I(\lambda) = I_1(\lambda) + I_2(\lambda) + 2\sqrt{I_1(\lambda)I_2(\lambda)}\cos\left(2\pi\Delta nL/\lambda\right) \tag{4.1}$$

where $I_1(\lambda)$ and $I_2(\lambda)$ were the light intensities of two modes, λ was the wavelength, Δn was the ERI difference between HE_{11} mode and HE_{12} mode, L was the length of mode interference in the direction of propagation. We calculated two extreme cases, including a 30-mm-long HCMOF with the uniform structure same as the non-deformation area (as Fig. 4.1(b)) and a 30-mm-long HCMOF with the uniform structure same as the deformation area (as Fig. 4.1(e)). Based on the ERI illustrated in Fig. 4.3 and the power ratio, the transmission spectra of both cases were calculated and shown in Fig 4.4. The deformation led to a significant decrease of the extinction ratio and the reduction of the FSR in the transmission spectrum.

For calculating the spectrum of the sensor with 30 periodical deformations, we suppose that all deformation areas have the uniform structure same as the cross-section A-A with a total length of 4.5 mm for an approximate analysis. The rest length of the non-deformation HCMOF is 25.5 mm. The transmission spectrum can be calculated by the equation:

$$\begin{aligned} I(\lambda) = (1-p)\big(I_1(\lambda) + I_2(\lambda)\big) + p\big(I_1'(\lambda) + I_2'(\lambda)\big) \\ +2\sqrt{(1-p)I_1(\lambda)I_2(\lambda) + pI_1'(\lambda)I_2'(\lambda)} \\ *\cos\left(2\pi\Delta n_{12}(1-p)L/\lambda + 2\pi\Delta n_{12}'pL/\lambda\right) \end{aligned} \tag{4.2}$$

where p is the ratio between the length of the deformation area and the whole length of HCMOF. $I_1(\lambda)$, $I_2(\lambda)$ and $I'_1(\lambda)$, $I'_2(\lambda)$ are the light intensities of HE_{11} mode and HE_{12} mode at the non-deformation and deformation areas, respectively. Δn_{12} and $\Delta n'_{12}$ are the ERI difference between HE_{11} mode and HE_{12} mode at the non-deformation and deformation areas, respectively. L is the whole length of HCMOF. The calculated spectrum, shown in Fig. 4.4 (blue curve), exhibits a slightly smaller extinction ratio and FSR compared with the spectrum of HCMOF without deformation.

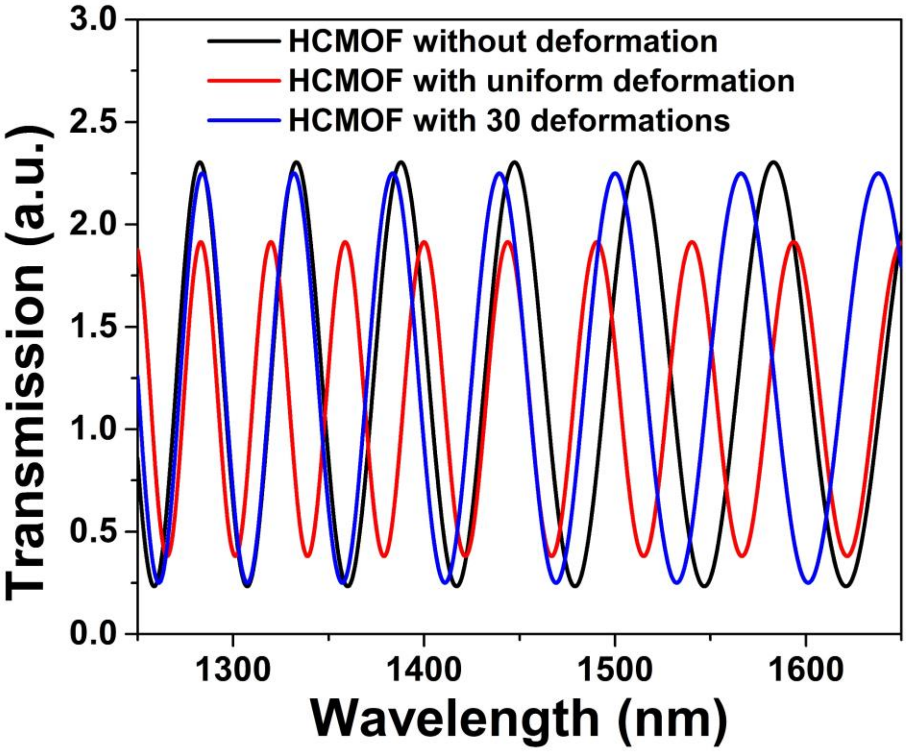

Figure 4.4 Simulated MZI spectra of a 30-mm-long HCMOF without deformation, a 30-mm-long HCMOF with uniform deformation along the whole fiber and a 30-mm-long HCMOF with 30 deformations.

When strain is applied to a segment of uniformly tapered fiber, the variation Δl of the fiber length can be calculated by the following equation [161]:

$$\Delta l = 4Fl/\pi E d_1 d_2 \tag{4.3}$$

where F is the axial force, l is the initial length of the fiber, E is Young's modulus, d_1 and d_2 are the minimum and maximum diameter of the tapered fiber. Based on this equation, the smaller value of $d_1 \times d_2$ leads to the larger Δl compared to a segment of non-tapered fiber (d_1 is equal to d_2). Hence, the deformation area of our sensor, composed of 30 small tapers, will have a bigger variation compared with the same length of the non-deformation area when strain is applied to the sensor. Further, p in Eq. 4.2 will become larger with the strain increase, which results in the extinction ratio decrease of dips in the transmission spectrum. The weight of the deformation area is enhanced in the sensing unit with the strain increase.

4.4 Results and discussions

Experimentally, we monitored the transmission spectrum of the sample in real-time when periodical deformations were fabricated, as illustrated in Fig. 4.5. The extinction ratio of the transmission spectrum decreased, and the dips of the transmission spectrum slightly shifted to shorter wavelengths. These variation trends were consistent with the simulation results in Fig. 4.4. To confirm the mode interference, we have measured the near-field distribution of the output light of the sample (after cleaving at one of the splice points) based on a tunable laser (Ando AQ4321D) and a camera (Spiricon SP1550M). The mode distribution at 1549.8 nm had the feature of HE_{11} mode, as shown in Fig. 4.6 (a), and the mode distribution at 1564.9 nm was similar to the one of HE_{12} mode, as indicated in Fig. 4.6(b). The asymmetry of HE_{12} mode was also experimentally observed. The saturation of HE_{12} mode distribution in Fig. 4.6(b) was because that the power difference between the central area and the outer area was larger than the dynamic range of the camera.

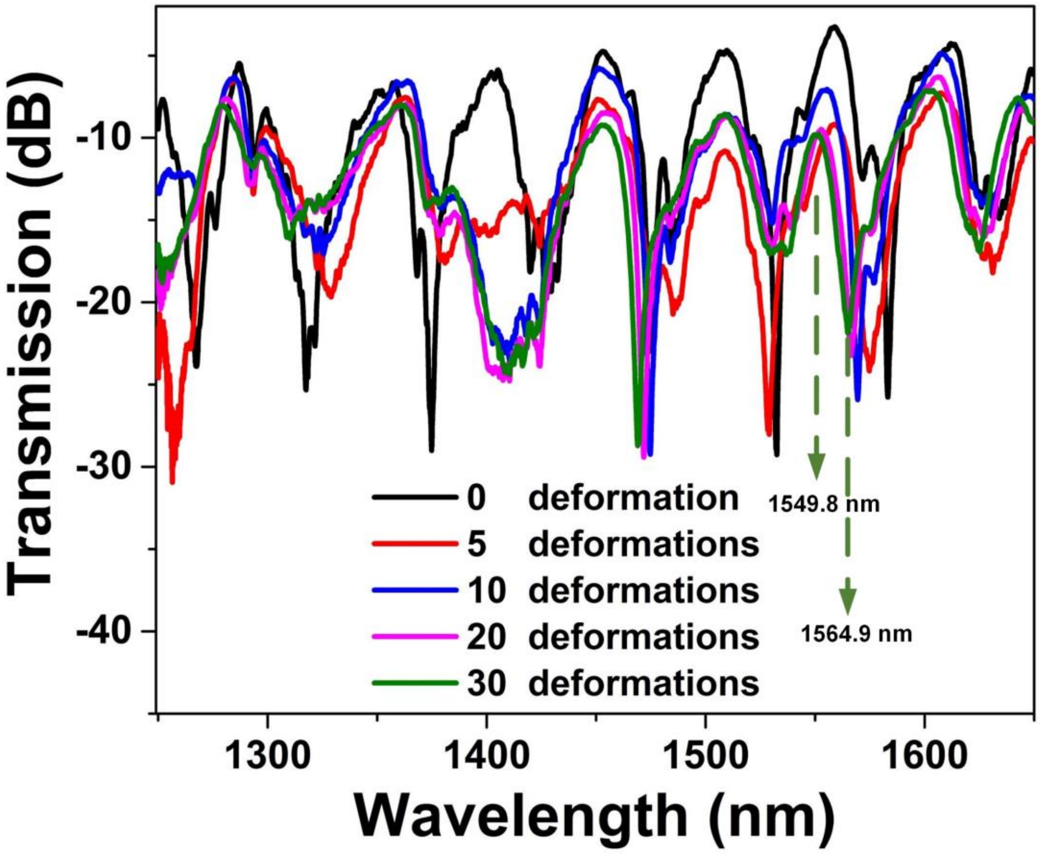

Figure 4.5 Transmission spectra during the fabrication process of the sensor.

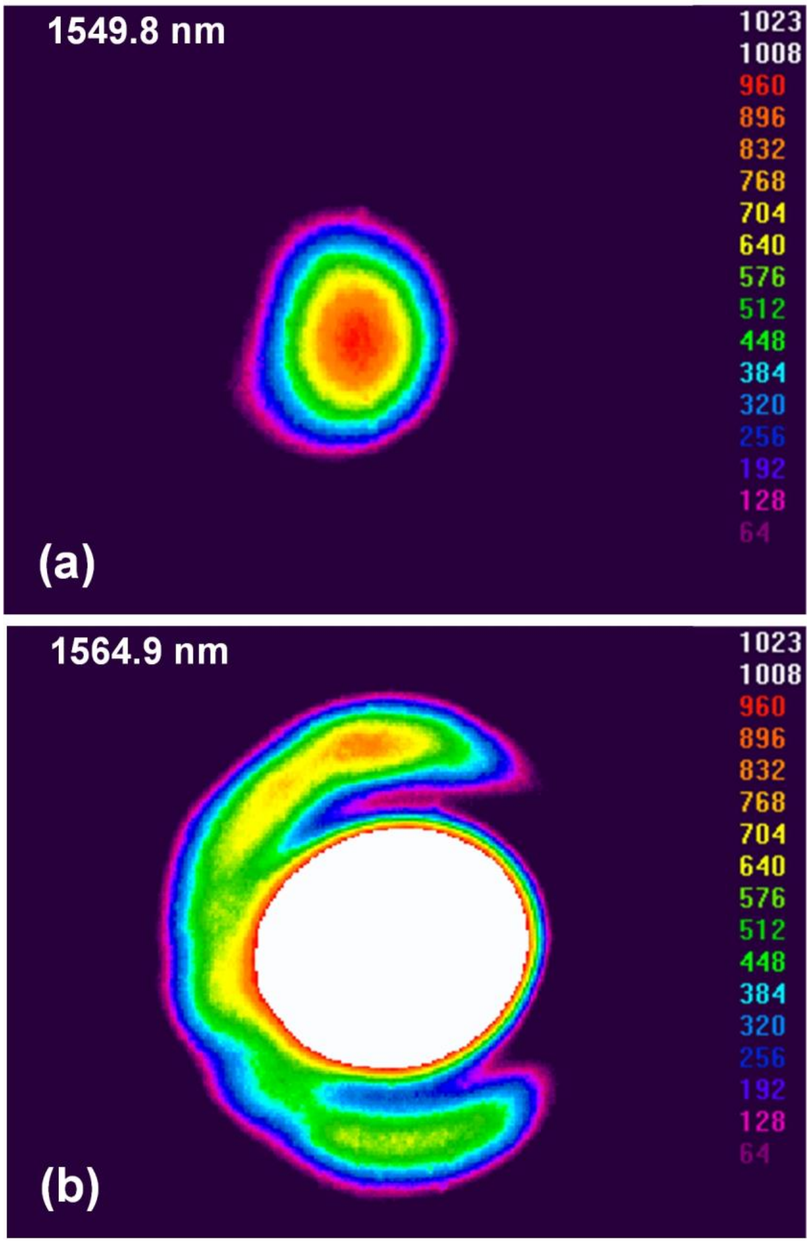

Figure 4.6 Mode field distribution of a 30-mm-long HCMOF with 30 deformations at (a) 1549.8 nm, and (b) 1564.9 nm.

The strain performance of the sensor with 30 periodical deformations in a 30-mm-long HCMOF was investigated from 0-1000 με. The sensor was straight fixed by two holders on two stages, respectively. The initial distance between the two holders was around 200 mm. Then, one holder was fixed, and the other one was moved with the stage to stretch the sensor. Two ends of the sensor were connected with a broadband light source (Infinon Research 1RBL-11111-F) and an OSA (Yokogawa AQ6370c), respectively. The spectral evolution of the sensor was illustrated in Fig. 4.7(a) with the strain increase. The normalized extinction ratio of the spectrum decreased following a two-order polynomial fit, as plotted in Fig. 4.7(b). The variation trend was matched well with the theoretical prediction. The strain sensitivity of the sensor reached to 0.00334 dB/με at 100 με.

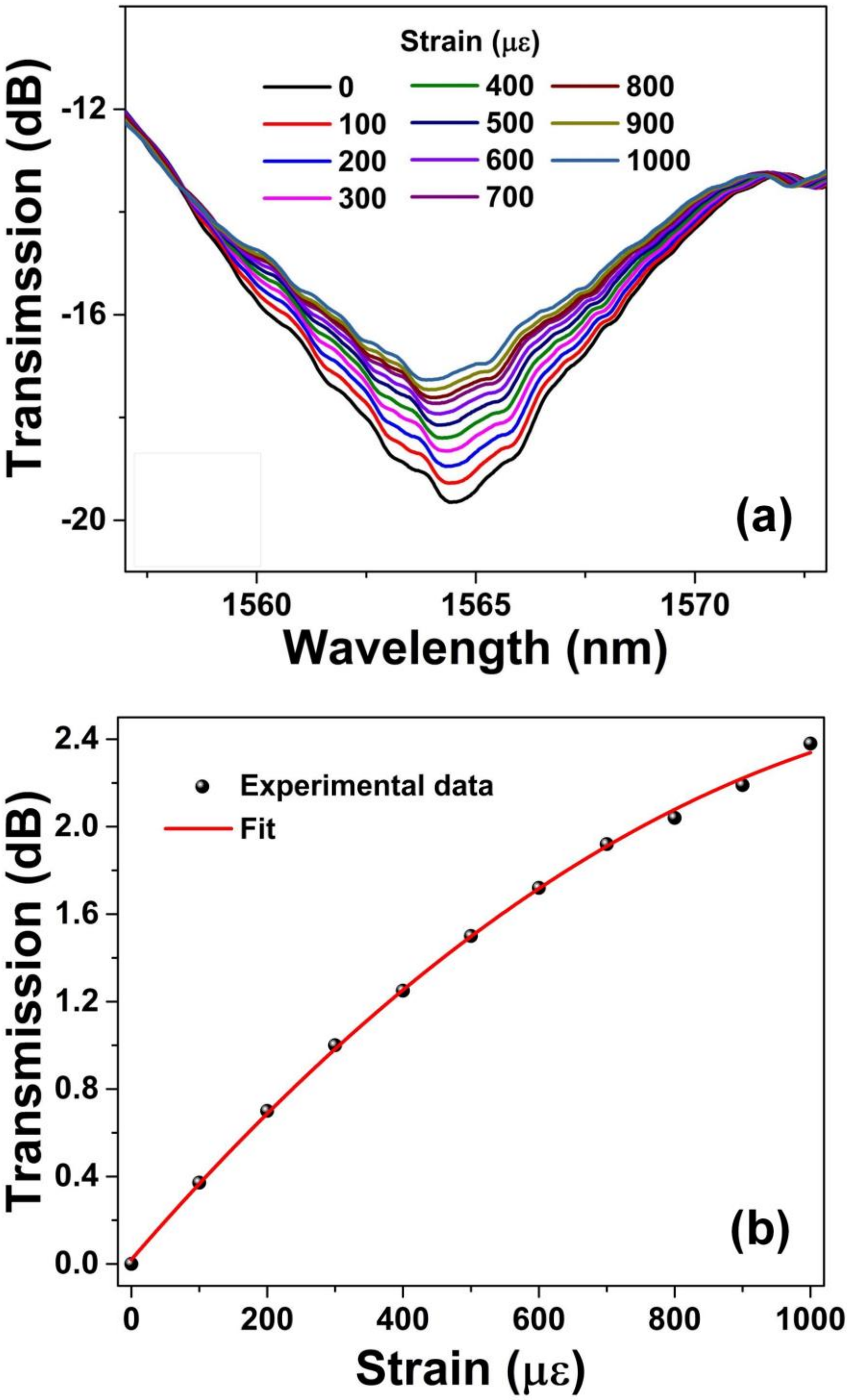

Figure 4.7 (a) Spectral evolution of the sensor with 30 deformations for strain sensing, (b) normalized intensity response of the sensor with 30 deformations to axial strain.

Besides, we also fabricated two more samples by splicing a 30-mm-long HCMOF with 20 periodical deformations and 10 periodical deformations into two segments of SMFs, respectively, for comparing the strain sensitivity improvement. The strain sensing performances of samples were measured and illustrated in Fig. 4.8(a) and Fig. 4.9(a). The normalized extinction ratio of the sensors with 20 periodical deformations and 10 periodical deformations also followed a two-order polynomial fit, as plotted in Fig. 4.8(b) and Fig. 4.9(b), respectively. The strain sensitivity of both sensors was 0.00227 dB/με and 0.00091 dB/με at the 100 με, respectively.

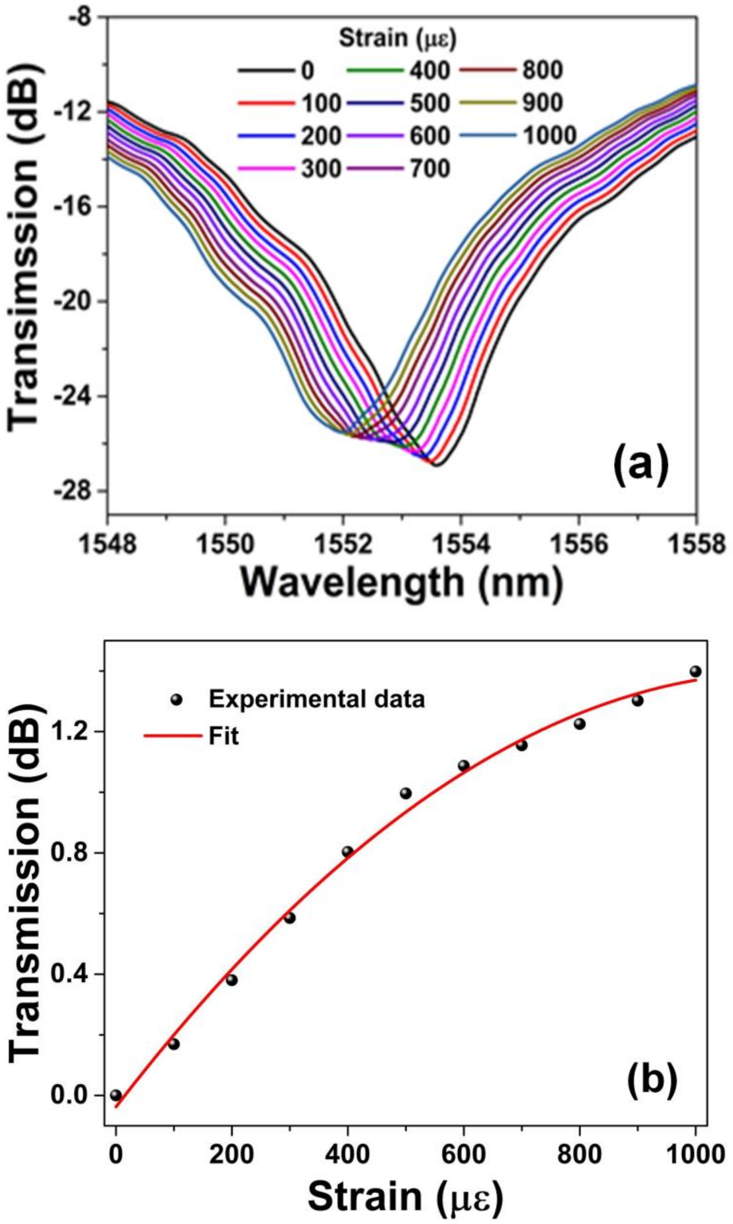

Figure 4.8 (a) Spectral evolution of the sensor with 20 deformations for strain sensing, (b) normalized intensity response of the sensor with 20 deformations to axial strain.

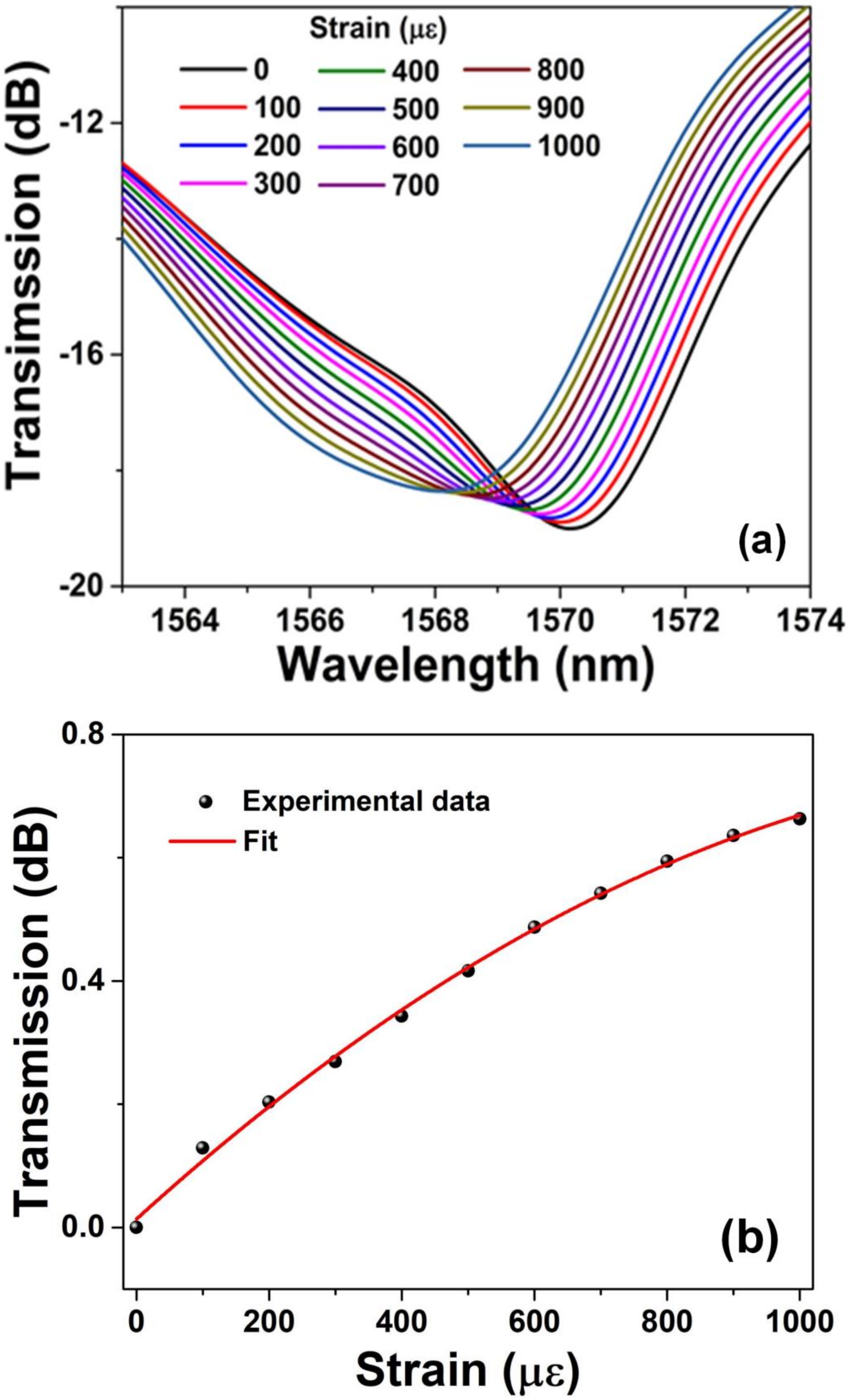

Figure 4.9 (a) Spectral evolution of the sensor with 10 deformations for strain sensing, (b) normalized intensity response of the sensor with 10 deformations to axial strain.

Further, based on the same measurement method of strain sensing, the spectral evolution of the sample without deformation was investigated and shown in Fig. 4.10(a). The normalized variation of the extinction ratio was only 0.68 dB from 0 to 1000 με, as indicated in Fig. 4.10(b), and the strain sensitivity was 0.00068 dB/με. These results demonstrated a strain sensitivity improvement by introducing the deformation, as shown in Table 4.1.

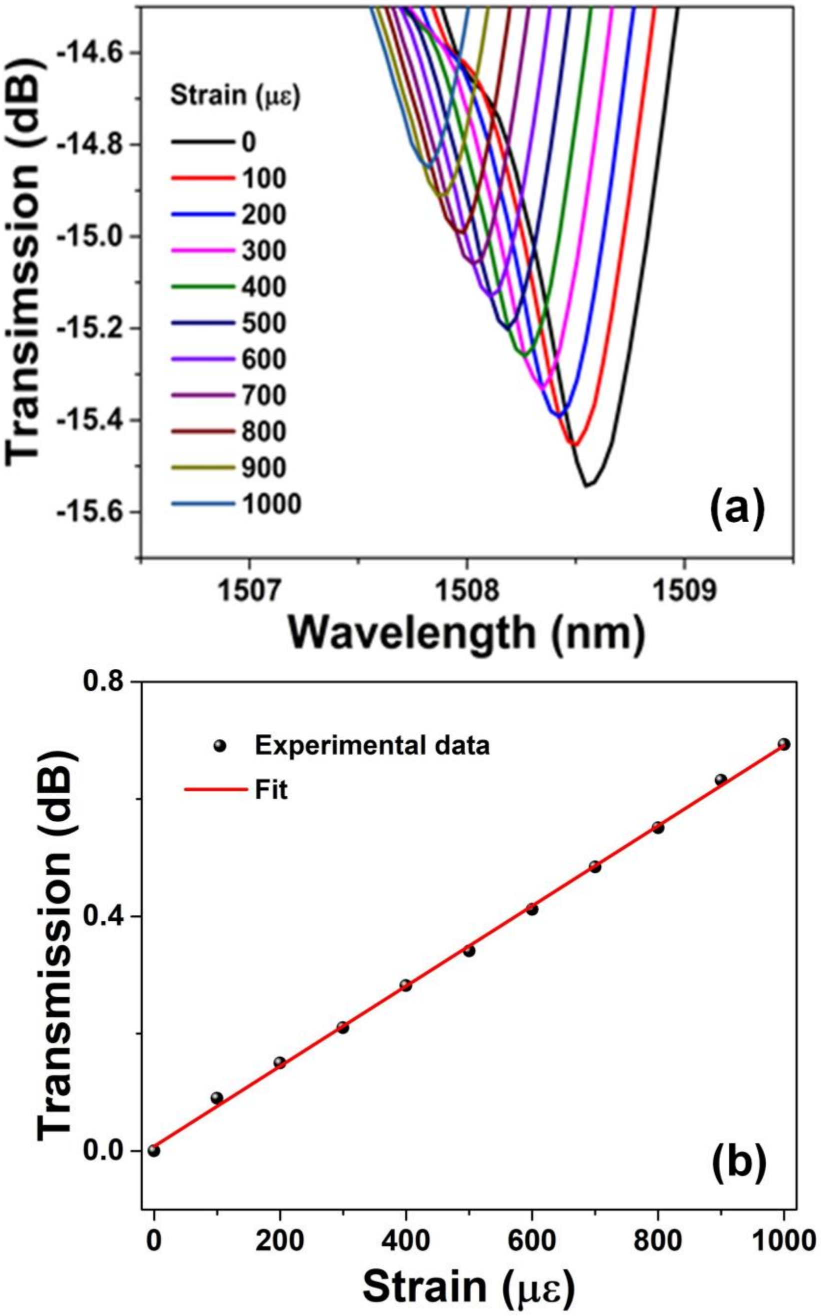

Figure 4.10 (a) Spectral evolution of the sensor without deformation for strain sensing, (b) normalized intensity response of the sensor without deformation to axial strain.

It is worth noting that the strain sensitivity increases with the number of deformations. However, as shown in the Fig. 4.5, when the number of deformations increases, the extinction ratio of the interference spectrum decreases. On the other hand, the increase in the number of deformations will reduce the fabrication repeatability. Hence, even if the strain sensitivity can be improved by further increasing the number of deformations, the extinction ration of the spectrum will degrade and the difficulty of fabrication will increase. There is a trade-off between these factors.

Table 4.1 Strain sensitivities of the sensors composed of a 30-mm-long HCMOF with 30 deformations, 20 deformations, 10 deformations and without deformation, respectively.

Sensors	Strain sensitivity (dB/με)
Sensor with 30 deformations	0.00334
Sensor with 20 deformations	0.00227
Sensor with 10 deformations	0.00091
Sensor without deformation	0.00068

4.5 Summary

In this chapter, an in-line MZI based on the HCMOF with periodical deformations has been proposed and demonstrated. The periodical deformations were simply fabricated by electric arc discharge. The power ratio of guided modes was modulated by these deformations, which led to the extinction ratio decrease of the transmission spectrum. Furthermore, since the axial tension could change the weight of deformations in the whole sensing unit, the strain sensitivity of intensity measurement was improved in comparison to the MZI based on the HCMOF without the periodical deformation. Experimentally, the MZIs with 30, 20, and 10 periodical deformations have been fabricated, respectively. The strain sensitivities of these MZIs were improved with the number of deformations increase. The MZI with 30 deformations

(0.00334 dB/με) possessed a 5 times higher sensitivity compared with the sensor without the deformation (0.00068 dB/με).

Table 4.2 shows the comparison of strain sensitivities with other optical fiber sensors based on the MZI. Our sensor possesses higher strain sensitivity than most of the previous sensors, and it is more robust and easy-to-fabricate than the MZI based on the T-shaped taper. Besides the improvement of strain sensitivity, we provide an effective and simple approach to modulate the modes in an optical fiber MZI, which may have a potential application in photonic neural networks [162]. Hughes *et al.* proposed and demonstrated a photonics neural networks based on several MZIs in a silicon photonic circuit. The XOR gate was realized by training the coupling direction of MZIs. Since the mode interference of our MZI sensor can be modulated by the periodical deformations and the strain, a simple neural networks could be formed by integrating our MZIs and 3-dB fiber couplers into an optical fiber networks, which is similar to the silicon photonic circuit. Our MZIs can be applied to modulate the output channels of 3-dB couplers based on the strain variation.

Table 4.2 Strain sensitivity comparison of optical fiber MZIs.

Types of MZI	Strain sensitivity
Gourd-shaped hybrid structure [163]	0.00290 dB/με
MZI based on no-core fiber [164]	-0.00061 dB/ με
MZI based on T-shaped taper [165]	0.00990 dB/ με
MZI based on hollow-core fiber [166]	-0.00207 dB/ με
Our sensor	0.00334 dB/με

Chapter 5 High-resolution and large-dynamic-range multimode interferometer sensor based on a SCMOF

Optical fiber sensors have been widely investigated in the past decades [167, 168]. However, the performance of these sensors is limited by either their dynamic range or resolution, which is a trade-off existing in almost all kinds of sensors. Liu *et al.* developed an optical fiber thermometer with double-cascaded silicon cavities, one thin and one thick, to tackle this problem [24]. The thin cavity provides the ability of large dynamic range measurement, and the thick cavity defines the high resolution. Nevertheless, the fabrication of ultra-thin cavities (10 and 200 μm) is complicated.

Strain sensors, as one critical application of optical fiber sensors, have widespread applications in many fields, such as geophysics research, mechanical engineering and particularly in the field of structural health monitoring for bridges, towers and railways etc. [169-171]. Various types of schemes have been used to demonstrate the optical fiber strain sensors, for instance, a polarization-maintaining PCF inserted in a Sagnac loop [94], an FBG in an MOF [146], Pound-Drever-Hall feedback loops based on an FBG and an FPI [172] and an in-line MZI in a twisted multicore fiber [153]. However, as we mentioned above, the performance of these sensors is restricted by the trade-off between the dynamic range and the resolution. For instance, the resolution of the sensor based on the SI is limited at 43 με with a dynamic range of 32 mε; the sensor fabricated by inscribing the FBG into the MOF only possesses a dynamic range of around 430 με with a resolution of 8.6 με; the sensor composed of the FBG and the FPI has ultrahigh resolution (0.01 nε), but the dynamic range of 300 με is narrow. Meanwhile, the secondary processing inside the specialty fibers, such as inscribing gratings or twisting fibers, will increase the complexity of the fabrication procedure and reduce the repeatability of the fiber sensors.

5.1 Geometry of SCMOF

SCMOF, as a typical MOF, is composed of a triangular core suspended with three thin struts and three air holes surrounding the fiber core. Due to the large refractive index difference between fiber core and cladding in the SCMOF, high order modes are easily excited in the small area of suspended triangular core [173]. Meanwhile, a high numerical aperture (NA) caused by the large refractive index difference leads to a low bending loss for high order modes. Hence, SCMOF can serve as an ideal platform for developing fiber sensors based on multimode interference.

The cross-sectional image of the SCMOF shown in Fig. 5.1 was obtained by utilizing an SEM. The fiber was fabricated with pure silica tubes by applying the stack-and-draw process. It is composed of a triangular fiber core surrounded by three crown-like air holes. The diameter of the circle inscribed in the triangular core is 3.3 µm. The diameter of the air cladding is 77 µm. The diameter of the fiber is 118 µm. The thickness of three struts is ~750 nm.

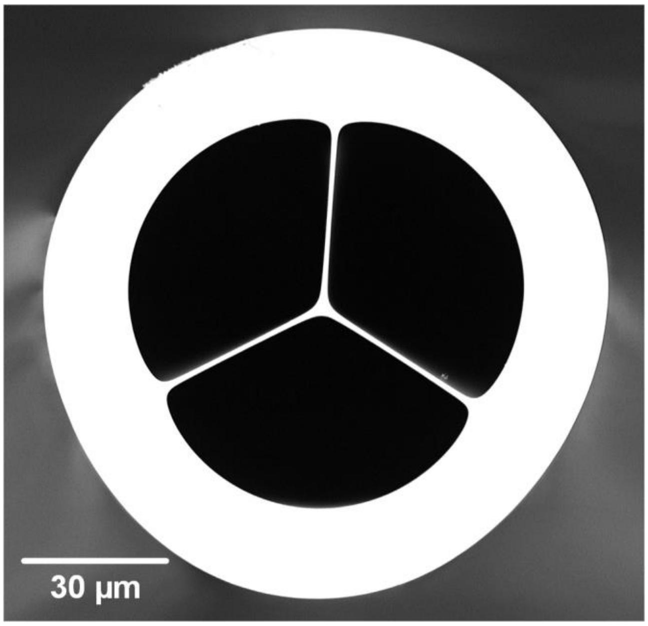

Figure 5.1 SEM image of the SCMOF cross section.

5.2 Fabrication of SCMOF

The SCMOF was also fabricated by the four-step stack-and-draw method in Xlim Research Institute, France. The drawing process was similar to that of the HCMOF. It could be briefly outlined as: firstly, the silica tubes with a suitable size were picked based on the fiber design. These silica tubes were pulled into ~1-m-length capillaries by the fiber tower. Secondly, three capillaries were stacked together and put into a large silica tube to construct the preform of the SCMOF. The schematic of the preform was illustrated in Fig. 5.2. The outer diameter and inner diameter of the large silica tube were 10 mm and 7 mm, respectively. Thirdly, the preform was drawn into several canes by the fiber tower. Finally, the cane was put into a silica jacket tube for increasing the thickness of the fiber cladding, then both the cane and the jacket tube were together drawn into the SCMOFs.

Similar to the drawing process of the HCMOF, in the third step, one end of the preform was placed into a metal chamber. Then the metal chamber was fixed on the top of the fiber tower. During the drawing process, a vacuum was applied in the large silica tube through the metal chamber for decreasing gaps between capillaries. In the last step, the cane and the jacket tube were put into two metal chambers, respectively. Each chamber had one air vent. During the drawing process, the vacuum was utilized to vanish the gap between the cane and the jacket tube through one air vent, and the pressure was applied into the cane for enlarging the size of three air holes and forming the triangular fiber core through the other air vent. Since the size of three air holes was larger than the size of gaps between capillaries, the pressure in the air holes was greater. By controlling the pressure, the sizes of the air holes and the fiber core could be adjusted.

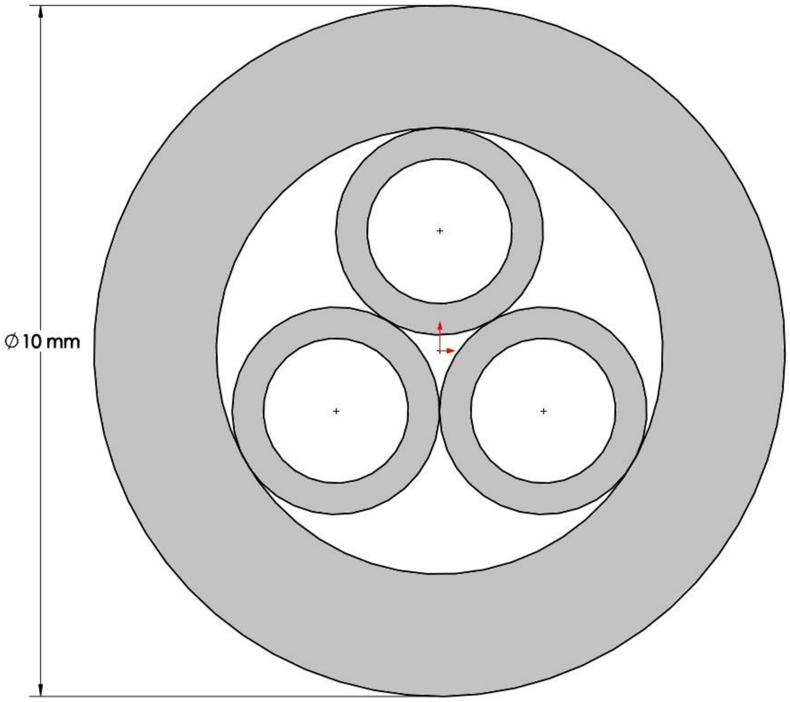

Figure 5.2 Schematic of SCMOF preform.

5.3 Numerical investigation on SCMOF

For theoretically studying the transmission spectrum of SCMOF, the transverse mode profiles of SCMOF were simulated by COMSOL Multiphysics 5.0. In the simulation model, the geometry of SCMOF was imported from its SEM image. The results indicated that the SCMOF steadily supported HE_{11} mode and two high order modes propagating in the suspended core, as shown in Fig. 5.3 (a)-5.3(c). When multiple modes were excited and propagated in the triangular fiber core, the mode interference would take place and lead to a transmission spectrum obtained by the fellow equation:

$$I(\lambda) = 2I_1(\lambda) + 2I_2(\lambda) + 2I_3(\lambda) + 2\sqrt{I_1(\lambda)I_2(\lambda)}\cos(2\pi\Delta n_{12}L/\lambda) \\ +2\sqrt{I_1(\lambda)I_3(\lambda)}\cos(2\pi\Delta n_{13}L/\lambda) + 2\sqrt{I_2(\lambda)I_3(\lambda)}\cos(2\pi\Delta n_{23}L/\lambda) \quad (5.1)$$

where $I_1(\lambda)$, $I_2(\lambda)$, $I_3(\lambda)$ are the light intensities of three modes, respectively. Δn_{12} is the difference between ERIs of the fundamental mode and first high order mode, Δn_{13} is the difference between ERIs of the fundamental mode and the second high order mode and Δn_{23} is the difference between ERIs of the first high order mode and the second high order mode. L is the length of SCMOF.

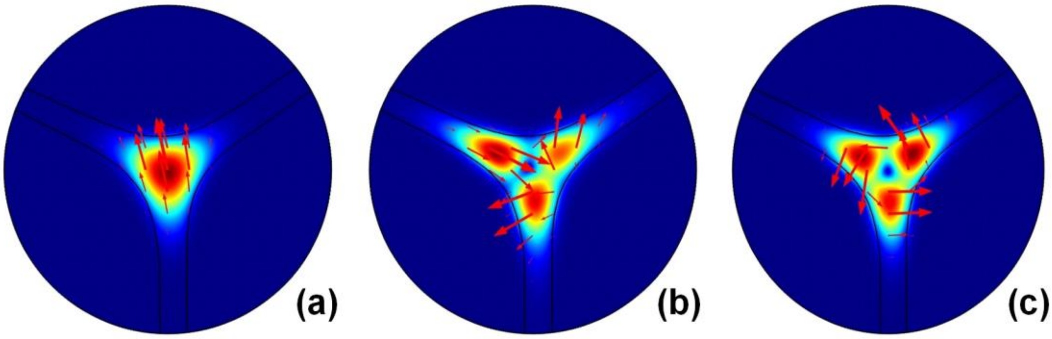

Figure 5.3 Simulated mode field distributions of the (a) HE_{11} mode, (b) first high-order mode, and (c) second high-order mode at the wavelength of 1550 nm.

The light intensities of three modes could be obtained by calculating their Poynting vectors according to the equation $S=E\times H$. E and H, the electric field vector and the magnetic field vector respectively, could be achieved under different wavelengths by the simulation in COMSOL. Based on light intensities and ERIs of three modes obtained from the simulation, the transmission spectra with different

SCMOF lengths of 4.0 cm, 6.5 cm and 15.0 cm were calculated and illustrated in Fig. 5.4, which were characterized by dense interference fringes modulated by one lower envelope. The dense interference fringes were from the mode interferences between the fundamental mode and two high order modes, and the lower envelope was induced by the superposition of three pairs of mode interferences. The FSRs of the dense interference fringes for the three samples were 2.67 nm, 1.65 and 0.74 nm around 1550 nm, respectively, and the FSRs of the lower envelopes were 32.8 nm, 20.4 nm and 8.9 nm, respectively.

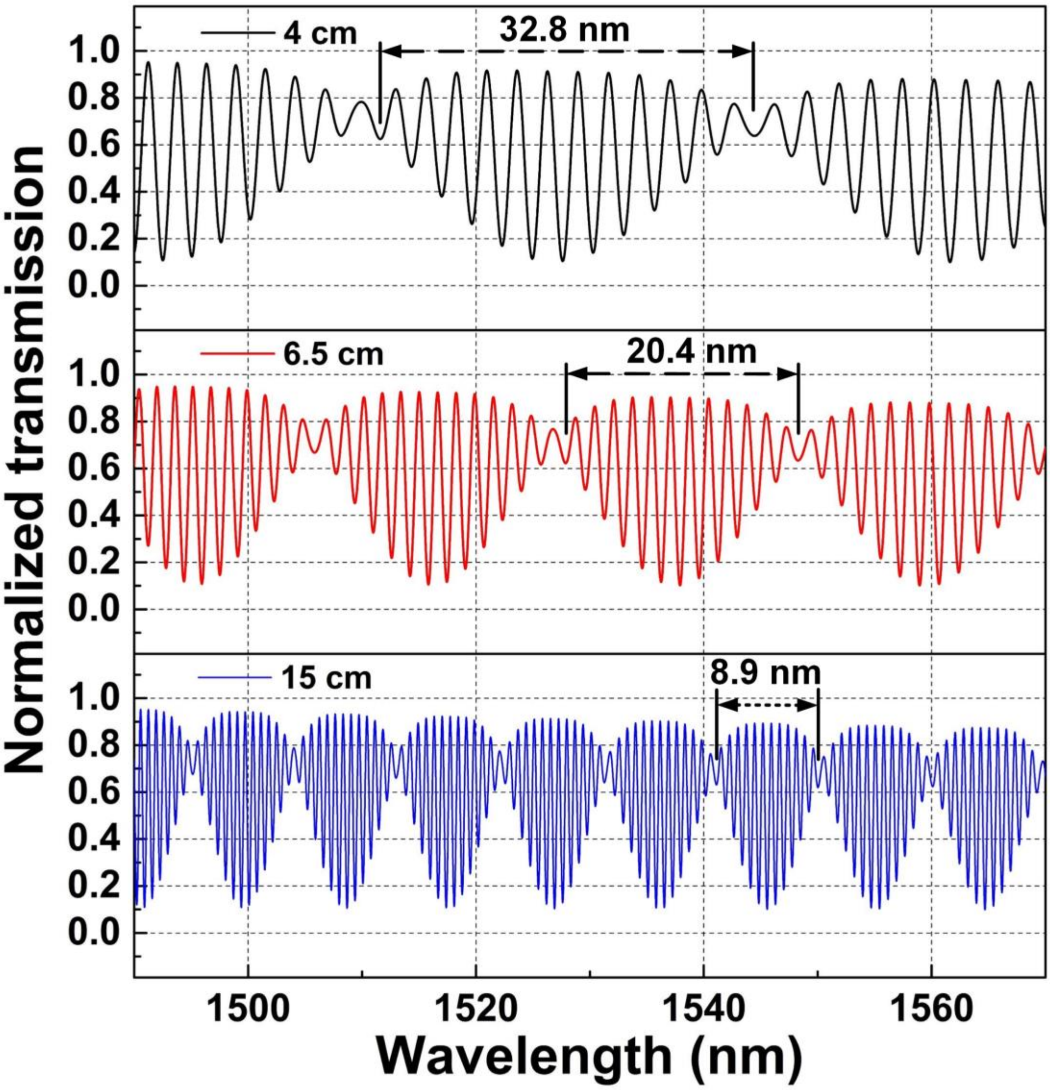

Figure 5.4 Simulated interference spectra of SCMOFs with a length of 4.0 cm (top panel), 6.5 cm (middle panel), and 15 cm (bottom panel), respectively.

When the SCMOF is stretched by an axial strain ε, the length of SCMOF and the ERI of guided modes will be changed. ε is defined as $\varepsilon = \Delta L / L_0$, where ΔL is the change of fiber length and L_0 is the initial length of fiber. Since the axial strain is isotropic and homogeneous along the fiber, the wavelength shift induced by the strain can be calculated by [32]:

$$\Delta\lambda = -(1 + 2\nu + p_\varepsilon)\varepsilon\lambda \tag{5.2}$$

where $p_\varepsilon = -n_0^2[(1-\nu)p_{12} - \nu p_{11}]/2$ is the effective photo-elastic coefficient, ν is the Poisson ratio of the SCMOF, p_{11} and p_{12} are the Pockel's coefficients, and n_0 is the original refractive index of fiber core before strain. The equation theoretically indicates that the strain response of the sensor is linear.

5.4 Results and discussions

The optical characterization of the multimode interferometer was investigated by sandwiching a section of SCMOF into two segments of SMFs. The alignments between the SCMOF and two SMFs were without offset. The splicing machine was Fujikura FSM-100P+, and the arc-time and the arc-power were 900 ms and 210 bits, respectively, which could ensure the repeatability of the device. The schematic of the sensing unit was shown in Fig. 5.5. Three samples have been fabricated with the length of SCMOF L_0 = *4.0 cm*, L_0 = *6.5 cm*, L_0 = *15.0* cm, respectively. The broadband light was launched into the sample from a light source (Infinon Research 1RBL-11111-F). Then the transmission spectra were detected at the sample output by an OSA (Yokogawa AQ6370c), as shown in Fig. 5.6.

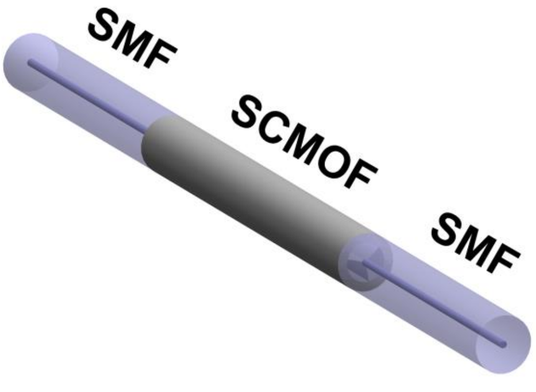

Figure 5.5 Schematic diagram of the sensing unit.

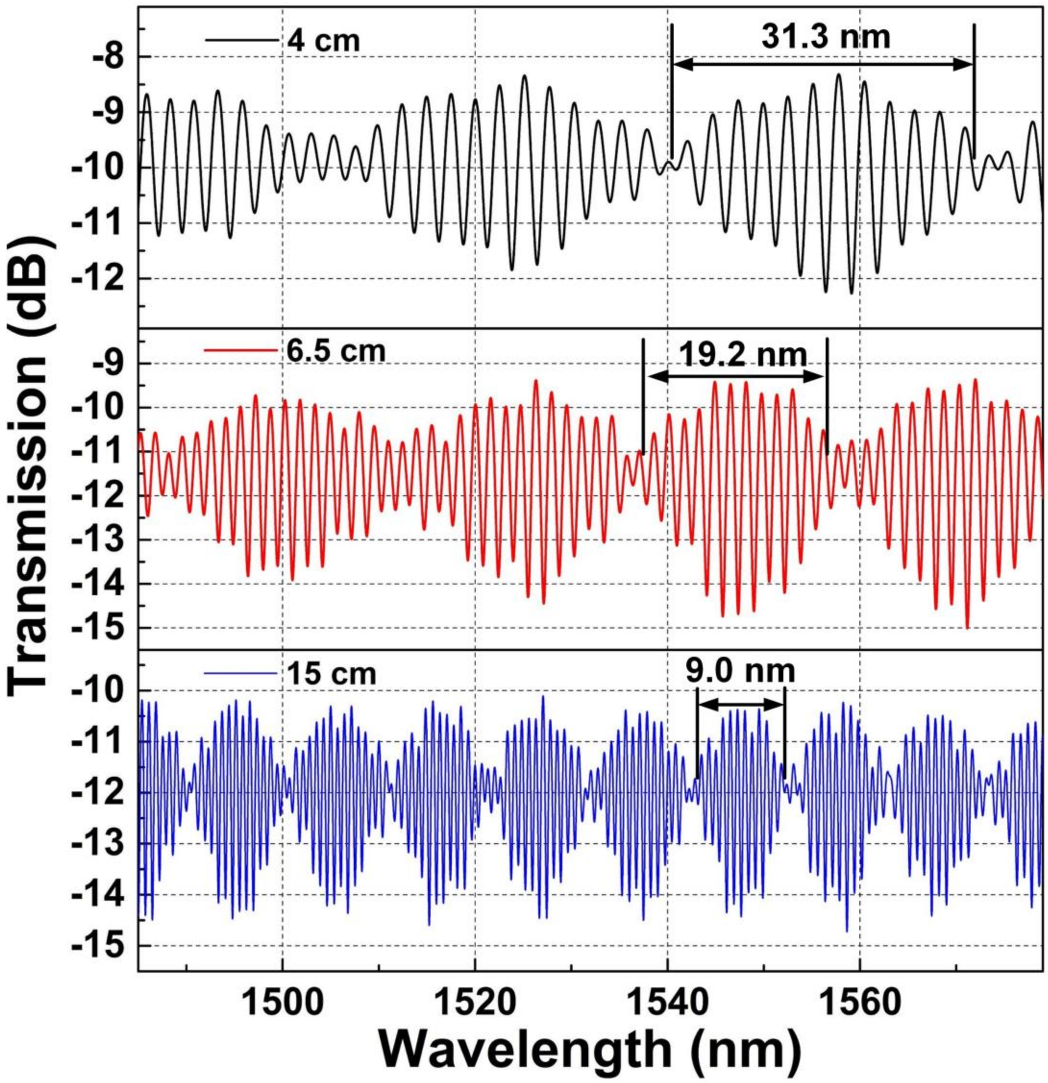

Figure 5.6 Experimental transmission spectra of sensing units with a 4.0-cm- (top panel), 6.5-cm- (middle panel), and 15.0-cm- (bottom panel) long SCMOF, respectively.

The FSRs of the dense interference fringes of the sensors with the 4-cm-long, 6.5-cm-long and 15-cm-long SCMOF are 2.57 nm, 1.63 nm and 0.76 nm around 1550 nm, respectively. The lower envelopes have a period of 31.3 nm, 19.2 nm and 9.0 nm, respectively. Both experimental FSRs of the dense fringes and the lower envelopes match well with the simulation result, which indicates that the multimode interference proposed in the simulation model dominates the light-guiding mechanism of our device.

For further validating the multimode interference in SCMOF, the FFT is adopted to obtain the spatial frequency spectra of the simulation and experiment transmission spectra of the sensor with a 6.5-cm-long SCMOF, respectively. As shown in Fig. 5.7(a), the spatial frequency spectrum of the simulation spectrum, three peaks located at 0.05 nm^{-1}, 0.59 nm^{-1} and 0.64 nm^{-1} are observed, corresponding to the FSR components of 20.00 nm, 1.69 nm and 1.56 nm, respectively. These FSR components are consistent with the FSRs of three pairs of mode interferences. The spatial frequency spectrum of the experiment spectrum is plotted in Fig. 5.7(b). Obviously, the experiment spectrum has the same frequency components (Peak 1 and Peak area 2) with the simulation spectrum. Although several other frequency peaks appear in Fig. 5.7(b), which should be induced by the mode interferences between higher modes, Peak area 2 dominates in the frequency spectrum. For further investigating the influence of Peak 1 and Peak area 2 on the transmission spectrum, the FFT bandpass filtering method is applied to obtain the spatial distribution of dominated mode interferences. Firstly, the other frequency peaks are filtered and Peak 1 and Peak area 2 are kept. Then by taking inverse FFT for the remaining frequency spectrum, the corresponding interference spectrum is displayed in the inset of Fig. 5.7(b). The interference spectrum reveals a neater spectrum distribution than the experiment spectrum in Fig. 5.6, and possesses similar distribution with the simulation spectrum in Fig. 5.4. Hence, the multimode interference in SCMOF induced by three pairs of mode interferences is confirmed.

To validate the large dynamic range and the high resolution of the proposed sensor, the devices with a 4.0-cm-long SCMOF and a 6.5-cm-long SCMOF were applied to measure the strain response, respectively. The device was straight fixed by two fiber holders on two stages, respectively. The distance between two fiber holders was ~250 mm. Then one stage was fixed, and the other one was moved away from the fixed one for stretching the device. The strain response performance of our devices was investigated and illustrated in Fig. 5.8(a) and 5.8(b). The dense interference fringes and the lower envelope shift to shorter wavelengths with the axial strain increase from 0 to 640 $\mu\varepsilon$. Compared with the transmission spectrum without strain, the number of dense fringes in one hump of the lower envelope is equivalent, which indicates that both the dense fringes and the lower envelope have the equal strain responsivity. This is because that three pairs of mode interferences simultaneously take place in the same fiber core. This spectrum characteristic of our device makes the dense fringes and the lower envelope without crosstalk.

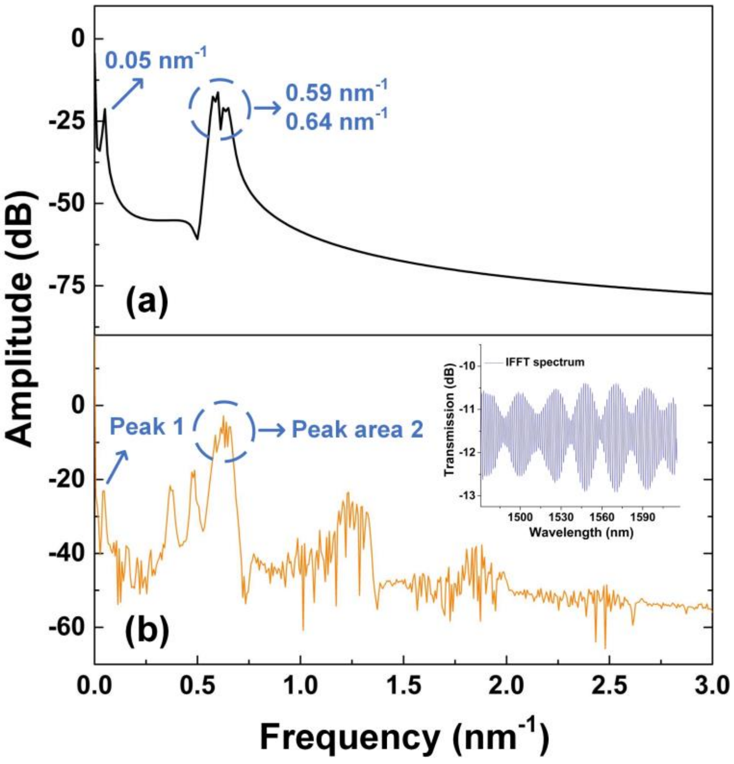

Figure 5.7 (a) FFT of the simulation spectrum of the sensor with a 6.5-cm-long SCMOF; (b) FFT of the experiment spectrum of the sensor with a 6.5-cm-long SCMOF, and the inset is the inverse FFT of the Peak 1 and Peak Area 2.

By using the method of averaging wavelengths of numerous dense peaks, the dynamic range of the sensor will rely on the dynamic range of the lower envelope that is much larger than the dynamic range of the dense fringes [174]. In the meantime, the resolution of the sensor will depend on the resolution of the dense fringe, which is also improved relative to the resolution of the lower envelope. For the sensor we fabricated, the average wavelength positions of 12 peaks are used to calibrate the strain response, and have been linearly fitted as shown in Fig 5.8(c) and 5.8(d). The linear response is consistent with the theoretical prediction. The corresponding strain sensitivities are calculated to be -3.4 pm/με and –2.0 pm/με for the device with the 4-cm-long SCMOF and the 6.5-cm-long SCMOF, respectively. Theoretically, for the sensor with the 4-cm-long SCMOF, the dynamic range of the strain sensor depends on the distance between two peaks of the lower envelope. It reaches 0-9200 με, which is 12 times larger than the dynamic range of the dense interference peak (0-750 με). Meanwhile, the resolution of the strain sensor with the 4-cm-long SCMOF relies on the full width at half maximum of the dense interference peak and is about 17.5 times higher than that of the lower envelope. The continuous spectral measurement is applied to ensure the method of tracking the set of 12 peaks without ambiguity. Compared with the strain sensors in [175-177], our device possesses both higher resolution and larger dynamic range.

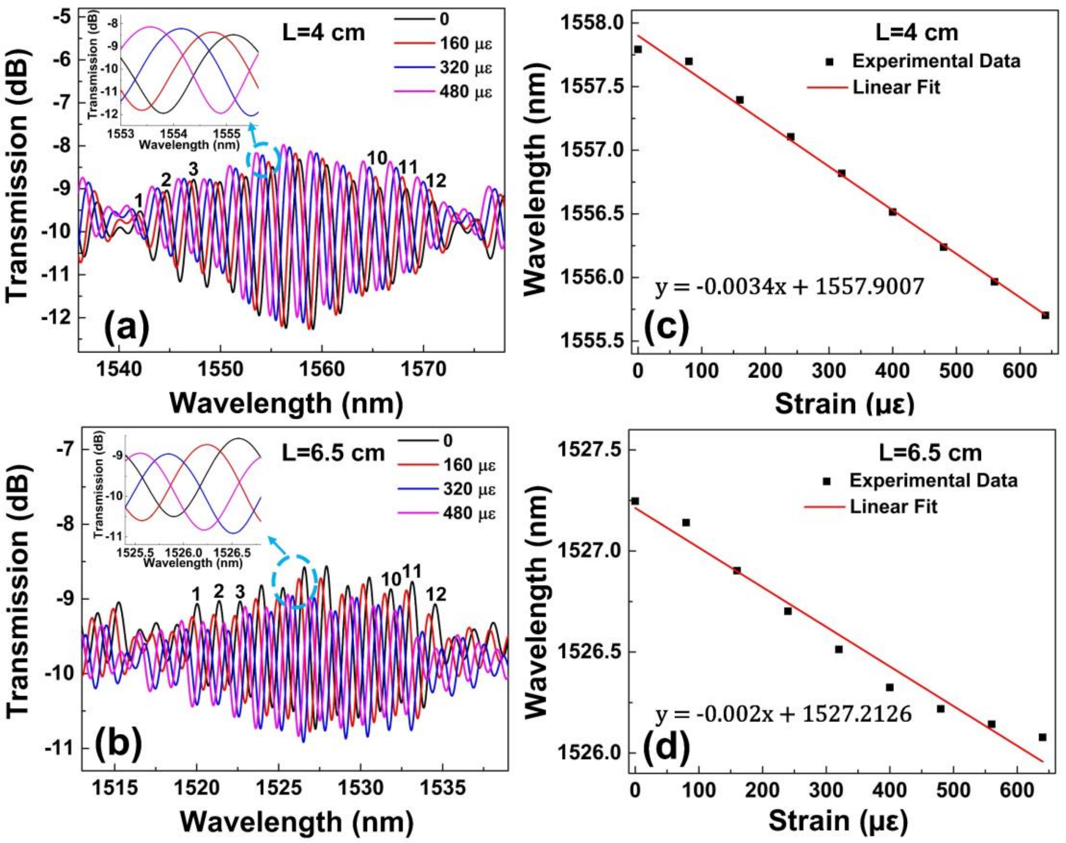

Figure 5.8 Spectral evolution of the sensing unit with a (a) 4.0-cm-long SCMOF and (b) 6.5-cm-long SCMOF for strain measurement, (c) and (d) strain response of two devices from 0 to 640 με respectively, and the insets are spectral evolution of one wavelength dip.

5.5 The birefringence of SCMOF

Due to the non-circular symmetry of the suspended core, SCMOFs have the intrinsic birefringence. In this section, by inserting an SCMOF into an SI, we fabricated a sensitive all-fiber device based on the birefringence effect, which could be used for multi-parameter sensing applications such as temperature, bending, torsion and refractive index measurements. The SCMOF steadily supported two HE_{11} modes with two polarizations and four high order modes with different polarizations to propagate in the suspended core from 1250 nm to 1650 nm. These mode profiles were simulated by using COMSOL Multiphysics 5.0, as shown in Fig. 5.9(a)-5.9(c), which theoretically demonstrated the birefringence property of this SCMOF. In our experiment, the SCMOF was spliced between two segments of SMFs by using a splicing machine (Fujikura FSM-100P+). The arc-power and arc-time were 210 bits and 900 ms, respectively, which could ensure the repeatability of the device.

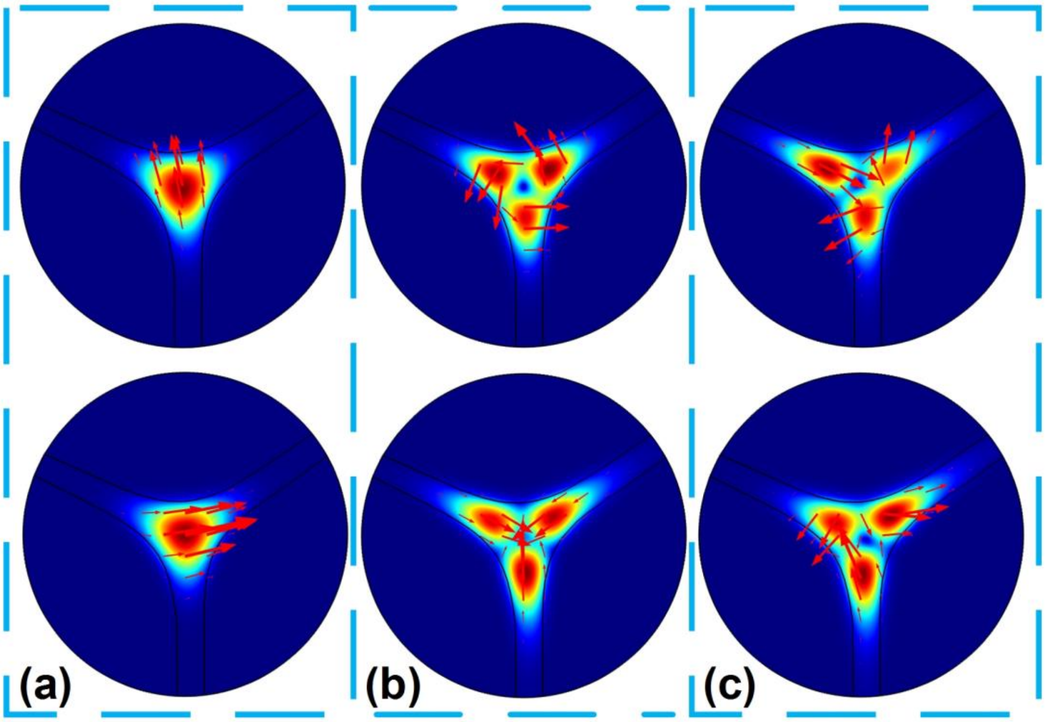

Figure 5.9 Simulated mode profiles of (a) HE_{11} modes for two polarization and (b), (c) high order modes for two polarization states at the wavelength of 1550 nm.

By inserting the SMF-SCMOF-SMF structure into the Sagnac loop, the SCMOF based SI device was obtained. The schematic diagram of our setup was shown in Fig. 5.10. A broadband light was split into two counter-propagating beams by a 3 dB fiber coupler with the same power. After propagating through the SCMOF, the two beams returned the 3 dB coupler, took place the interference and detected by the OSA (Yokogawa AQ6370c).

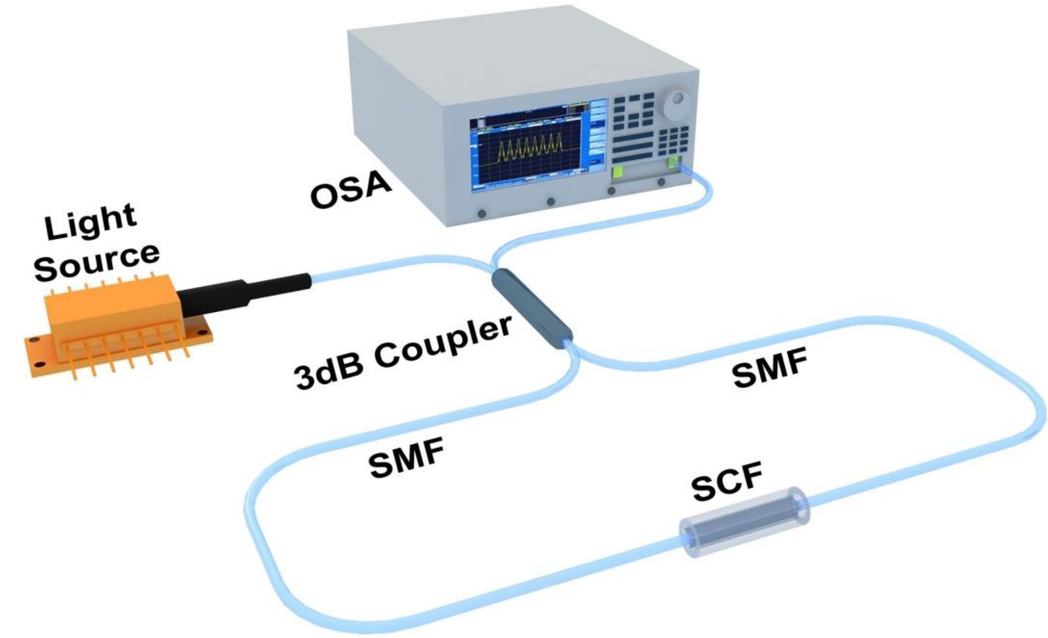

Figure 5.10 Schematic of the SCMOF based SI.

Sagnac interference spectra of the devices with a 20-cm-long SCMOF and 10-cm-long SCMOF were measured and illustrated in Fig. 5.11(a) and 5.11(b), respectively. As shown in these two spectra, the spectrum with the longer SCMOF has a narrower FSR. When the length of SCMOF is 20 cm, the FSR of the Sagnac spectrum is about 159 nm. The birefringence of the SCMOF is ~7.56×10^{-5} at 1550 nm calculated by the equation:

$$\mathrm{B} = \lambda^2/\Delta\lambda \cdot L \tag{5.3}$$

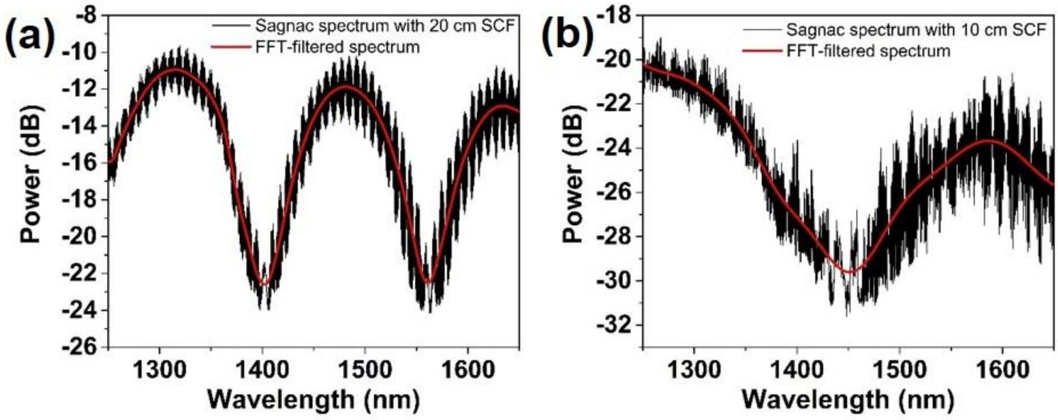

Figure 5.11 Sagnac interference spectra with different length SCMOFs, (a) 20 cm, (b) 10 cm.

Further, torsion measurement was conducted to characterize the sensing performance of the SI sensor. The SMF-SCMOF-SMF structure was straight held by two fiber rotators (Thorlabs, PRM1/M). The distance between the two rotators was ~250 mm. One rotator could be rotated and the other one was fixed. The torsion sensing spectra of this device were investigated by changing the rotation angle with a step of 10 degrees, as illustrated in Fig. 5.12(a). The wavelengths of peak B were blue-shifted and the intensities of peak B became smaller with the torsion angle increase, respectively, as shown in Fig. 5.12(b). By introducing a numerical fitting, the torsion sensitivity could be estimated to be 1.12 nm/°, which indicated that our device could be utilized as a highly sensitive torsion sensor.

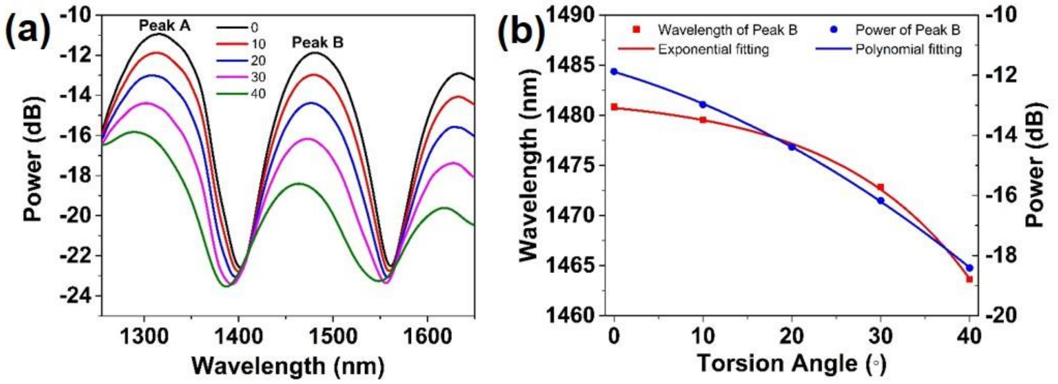

Figure 5.12 (a) FFT-filtered spectra of the proposed device under different torsion angles; (b) Wavelength and intensity responses of Peak B to the torsion angle.

5.6 Summary

In this chapter, an in-line multimode interferometer based on the SCMOF has been theoretically and experimentally demonstrated to obtain a large dynamic range and a high resolution simultaneously. The interference spectrum features dense fringes modulated by a lower envelope without ambiguity. The lower envelope determines the large dynamic range, while the dense fringes define the high resolution. Experimentally, the interferometers with a 4-cm-long, 6.5-cm-long and 15-cm-long SCMOF have been fabricated and characterized. For validating the large dynamic range and the high resolution of the interferometer, the strain responses of the sensors with a 4-cm-long and 6.5-cm-long SCMOF have been investigated, respectively. Particularly, the dynamic range of the strain sensor with a 4-cm-long SCMOF increases 12 times and the resolution improves 17.5 times. The proposed in-line multimode interferometer provides a simple method to tackle the trade-off between a large dynamic range and a high resolution. Besides, the birefringence of the SCMOF is theoretically and experimentally investigated. The group birefringence of the SCMOF is obtained as 7.56×10^{-5} at 1550 nm by inserting the fiber into an SI. The torsion sensing performance of the SI is measured.

Chapter 6 Conclusions and future work

6.1 Conclusions

MOFs have attracted widespread attention due to their intrinsic advantages, such as low guiding losses, versatile fiber cross-sectional structure and adjustability of optical and mechanical properties, etc. MOF sensors, as a critical research topic of MOFs, have been applied in the fields of physical parameter monitoring and biochemical sensing. The aims of this thesis are to study and improve the performance of MOF sensors based on the principle of MZI. The achievements of my Ph.D. project have stated in the thesis, which includes:

Firstly, a new HCMOF with a large and approximately circular hollow core surrounded by 12 crown-like air holes was developed. Pure silica tubes were applied to fabricate the fiber based on the stack-and-draw process. The diameter of the fiber was around 125 μm that was compatible with standard SMFs for easy and robust integration in fiber-sensor configurations. While, due to the large and approximately circular core, the fiber supported the multi-mode propagation in the core. Hence the HCMOF was an inherent platform for developing an in-line MZI.

Secondly, the HCMOF was utilized to construct a bending sensor. In this work, we theoretically simulated the relations of the bending sensitivity and the size of hollow core, and the bending sensitivity and the interference modes. Then, bending sensors was experimentally demonstrated by splicing our HCMOF into two segments of SMFs with central alignment. The transmission spectra of the different-length HCMOFs were investigated, which revealed that the HE_{11} and HE_{12} modes were predominantly excited in the hollow core. For verifying the bending sensitivity improvement, the transmission spectrum evolution of the sensor was recorded during the range of bending angle from -14° to 14°. The bending sensitivity of our sensor was 10 times larger than that of the bending sensor composed of an HCMOF with a smaller hollow core, which indicated that the bending sensitivity of HCMOF was positively dependent on the size of hollow core. Besides, a low thermal sensitivity of 2.5 pm/°C was also investigated.

Thirdly, we proposed and demonstrated a novel approach to modulate the mode interference of an HCMOF-based sensor and improve the strain sensitivity. The HCMOF-based sensor was fabricated by sandwiching our HCMOF into two segments of SMFs. Due to the multi-mode propagation characteristic of the HCMOF, the sensor was an MZI structure. As a result of a small elasto-optical coefficient of silica, the MZI-based sensor had a low strain sensitivity. A method that was to build periodical deformations on the HCMOF was utilized to improve the strain sensitivity of the sensor. We built a theoretical model to clarify the principle of the strain sensitivity improvement. Experimentally, the strain responses of the sensors with 30 periodical deformations, 20 periodical deformations and 10 periodical deformations in a 30-mm-length HCMOFs were obtained from 0-1000 με. Besides, the strain sensitivity of the sensor based on the HCMOF without deformation was also measured. The results indicated that the periodical deformations improved the strain sensitivity of the sensor and the sensitivity was enhanced with the number of deformations increase.

Fourthly, we constructed an in-line MZI based on our designed and fabricated SCMOF. The MZI sensor simultaneously owned the properties of a large dynamic range and a high resolution. The SCMOF composed of a triangular core and three fan-shaped air holes was fabricated by the stack-and-draw process. The in-line MZI was made by splicing the SCMOF into two segments of SMFs with central alignment. The transmission spectra of the MZIs with different-length SCMOFs were theoretically and experimentally investigated, respectively. The spectrum characteristic of dense fringes modulated by a lower envelope was observed, which revealed that the mode interference was induced by three modes. The lower envelope provided the large dynamic range, while the dense fringes resulted in the high resolution. Besides, the birefringence of the SCMOF was also studied. The MZI based on the three-mode interference provided a scheme to solve the trade-off between the dynamic range and resolution in the optical fiber sensors.

6.2 Future work

In the future work, a few experiments can be studied:

1. *HCMOF-based magnetic field sensor*. Optical fiber magnetic field sensor based on magnetic fluid can pave the way to demonstrate a highly integrated optomagnetic system. Through infiltrating the magnetic fluid into the outer air holes of our HCMOF, a magnetic field sensor can be constructed based on the anti-resonant reflecting effect. Further, due to the feature of 12 outer air holes, a highly integrated multi-point magnetic field sensor can be fabricated by infiltrating different-concentration magnetic fluids into different air holes. The magnetic field sensor can lay the foundation for developing an optomagnetic biosensor.

2. *HCMOF-based gas sensor*. Gas sensing is of great significant in many fields, such as environment monitoring, chemical industry, and gas lasing system. Optical fiber based gas sensors have advantages of immunity to electromagnetic interference, small size and remote measurement, etc. The HCMOF-based gas sensor operates under the theory of the anti-resonant reflecting effect, which is sensitive to the refractive index change of surrounding medium. Hence, the HCMOF provides a robust platform to immobilize 2D materials onto the fiber side surface for gas sensing, for example, ZnO-Bi_2O_3 nanosheet for acetone sensing.

3. *Whispering gallery microcavity integrated fiber platform*. The remarkable properties of light-matter interactions in whispering gallery mode (WGM) resonators have been widely studied and led to myriads of applications in optical filters, biochemical sensors, microlasers, and nonlinear optics. Most of these achievements are realized only in the laboratory with setups that require very careful alignments and positioning. For example, in the reported papers, one of the methods for obtaining high coupling efficiency requires a tapered fiber with a waist diameter less than 2 μm and a sub-micrometer scale precision positioning. However, it is difficult to maintain the robustness of a tapered fiber with such a small size and precision positioning. Hence, we plan to integrate the WGM resonators into the air holes of our HCMOF or SCMOF for developing a robust in-fiber WGM platform. The air holes are also inherent channels for biochemical trace detection.

List of Publications

Journal papers

[1] **Y. Zheng**, P. P. Shum, S. Liu, B. Li, J. Auguste, G. Humbert and Y. Luo. "Strain Sensitivity Enhancement Based on Periodic Deformation in Hollow Core Fiber," *Opt. Lett.* **45**(14): 3997-4000 (2020).

[2] **Y. Zheng**, P. P. Shum, Y. Luo, Y. Zhang, W. Ni, G. Wang, Z. Wu, X. Q. Dinh, J. Auguste and G. Humbert. "High-resolution, large-dynamic-range multimode interferometer sensor based on a suspended-core microstructured optical fiber," *Opt. Lett.* **45**(4): 1017-1020 (2020).

[3] **Y. Zheng**, P. P. Shum, S. Liu, B. Li, Y. Xiang, Y. Luo, Y. Zhang, W. Ni, Z. Wu, X. Q. Dinh, S. Zeng, J. Auguste and G. Humbert. "Experimental and numerical investigation on hollow core photonic crystal fiber based bending sensor," *Opt. Express* **27**(21): 30629-30638 (2019).

[4] **Y. Zheng**, Z. Wu, P. P. Shum, Z. Xu, G. Humbert, H. Zhang, S. Zeng and X. Q. Dinh. "Sensing and lasing applications of whispering gallery mode microresonators," *Opto-Electron. Adv.* **1**(9): 18001501–18001510 (2018).

[5] W. Ni, R. Xia, P. P. Shum, Y. Luo, **Y. Zheng**, Z. Lian. "Bragg labeled wavelength calibrates interferometric sensors in hollow core fiber," *Opt. Lett.* **44**(21): 5382-5385 (2019).

[6] Y. Zhang, N. Zhu, T. Zhou, **Y. Zheng**, P. P. Shum, "Research on Fabrication and Sensing Properties of Fiber-Coupled Whispering Gallery Mode Microsphere Resonator," *IEEE Sens. J.* **20**(2): 833-841 (2019).

[7] N. M. Y. Zhang, K. Li, N. Zhang, **Y. Zheng**, T. Zhang, M. Qi, P. Shum, L. Wei, "Highly sensitive gas refractometers based on optical microfiber modal interferometers operating at dispersion turning point," *Opt. Express* **26**(22): 29148-29158 (2018).

Conference papers

[1] **Y. Zheng**, P. P. Shum, S. Liu, W. Ni, Y. Luo, G. Wang, B. Li, C. Wang, Z. Wu, J. Auguste and G. Humbert. "Highly sensitive bending sensor based on a tapered hollow core microstructured optical fiber," In *CLEO: Science and Innovations (JTu2G.26)*, 2020.

[2] **Y. Zheng**, P. P. Shum, Y. Luo, Y. Zhang, Z. Wu, J. Auguste and G. Humbert. "Suspended-core fiber based Sagnac interferometer device and sensing applications," In *CLEO: Science and Innovations (JW2A.108),* 2019.

[3] **Y. Zheng**, P. P. Shum, S. Liu, Y. Luo, B. Li, Y. Zhang, J. Auguste and G. Humbert. "Temperature-independent bending sensor based on hollow core microstructured optical fiber," In *IEEE Photonics Conference (IPC)*, 2019.

[4] **Y. Zheng**, P. P. Shum, S. Liu, W. Ni, Y. Luo, Z. Wu, X. Q. Dinh, J. Auguste and G. Humbert. "Anti-resonant reflecting effect in large-core hollow-core photonic crystal fiber for temperature sensing," In *International Conference on Optical Communications and Networks (ICOCN)*, 2019. (Best Student Paper Award)

[5] **Y. Zheng**, Z. Wu, H. Zhang, P. P. Shum, G. Humbert and X. Q. Dinh. "Design of Fabry-Perot refractometer based on a simplified hollow-core PCF with a CFBG pair," In *Conference on Lasers and Electro-Optics/Pacific Rim (CLEO-PR),* 2017.

[6] B. Li, Z. Tan, P. P. Shum, D. J. J. Hu, C. Wang, **Y. Zheng** and S. Liu. "Robust Convolutional Neural Network Model for Wavelength Detection in Overlapping Fiber Bragg Grating Sensor Network," In *Optical Fiber Communication Conference (OFC)*, 2020.

Bibliography

1. J. Hecht, *City of light: the story of fiber optics* (Oxford University Press on Demand, 2004).

2. P. Comtois, "John Tyndall and the floating matter of the air," Aerobiologia **17**(3), 193-202 (2001).

3. J. Tyndall, "Total Reflexion," Notes about Light (1870).

4. A. C. van Heel, "A new method of transporting optical images without aberrations," Nature **173**(4392), 39-39 (1954).

5. H. H. Hopkins, and N. S. Kapany, "A flexible fibrescope, using static scanning," Nature **173**(4392), 39-41 (1954).

6. E. Snitzer, "Cylindrical dielectric waveguide modes," JOSA **51**(5), 491-498 (1961).

7. K. Kao, and G. A. Hockham, "Dielectric-fibre surface waveguides for optical frequencies," in *Proceedings of the Institution of Electrical Engineers*, pp. 1151-1158 (1966).

8. T. Miya, Y. Terunuma, T. Hosaka, and T. Miyashita, "Ultimate low-loss single-mode fibre at 1.55 μm," Electron. Lett. **15**(4), 106-108 (1979).

9. F. Mitschke, and F. Mitschke, *Fiber Optics* (Springer, 2016).

10. P. Kaiser, E. Marcatili, and S. Miller, "A new optical fiber," Bell Syst. Tech. J. **52**(2), 265-269 (1973).

11. J. Knight, T. Birks, P. S. J. Russell, and D. Atkin, "All-silica single-mode optical fiber with photonic crystal cladding," Opt. Lett. **21**(19), 1547-1549 (1996).

12. O. Frazão, J. L. Santos, F. M. Araújo, and L. A. Ferreira, "Optical sensing with photonic crystal fibers," Laser Photonics Rev. **2**(6), 449-459 (2008).

13. M. Duguay, Y. Kokubun, T. L. Koch, and L. Pfeiffer, "Antiresonant reflecting optical waveguides in SiO2 - Si multilayer structures," Appl. Phys. Lett. **49**(1), 13-15 (1986).

14. F. Benabid, J. C. Knight, G. Antonopoulos, and P. S. J. Russell, "Stimulated Raman scattering in hydrogen-filled hollow-core photonic crystal fiber," Science **298**(5592), 399-402 (2002).

15. K. Schuster, V. Reichel, J. Kobelke, A. Schwuchow, J. Kirchhof, and A. B. Wojcik, "Effects of optical power and thermal impacts on microstructured and low index coated fibers–a comparison," in *55th International Wired and Cable Symposium*, pp. 480-483 (2006).

16. S. Kobayashi, T. Katagiri, and Y. Matsuura, "Microstructured tube-leaky glass waveguide for delivery of high-powered Er: YAG laser," J. Lightwave Technol. **32**(5), 986-990 (2014).

17. J. Limpert, A. Liem, M. Reich, T. Schreiber, S. Nolte, H. Zellmer, A. Tünnermann, J. Broeng, A. Petersson, and C. Jakobsen, "Low-nonlinearity single-transverse-mode ytterbium-doped photonic crystal fiber amplifier," Opt. Express **12**(7), 1313-1319 (2004).

18. F. Luan, J. Knight, P. S. J. Russell, S. Campbell, D. Xiao, D. Reid, B. Mangan, D. Williams, and P. Roberts, "Femtosecond soliton pulse delivery at 800nm wavelength in hollow-core photonic bandgap fibers," Opt. Express **12**(5), 835-840 (2004).

19. M. A. van Eijkelenborg, A. Argyros, G. Barton, I. M. Bassett, M. Fellew, G. Henry, N. A. Issa, M. C. Large, S. Manos, and W. Padden, "Recent progress in microstructured polymer optical fibre fabrication and characterisation," Opt. Fiber Technol. **9**(4), 199-209 (2003).

20. P. S. J. Russell, "Photonic-Crystal Fibers," J. Lightwave Technol. **24**(12), 4729-4749 (2006).

21. P. Roberts, F. Couny, H. Sabert, B. Mangan, D. Williams, L. Farr, M. Mason, A. Tomlinson, T. Birks, and J. Knight, "Ultimate low loss of hollow-core photonic crystal fibres," Opt. Express **13**(1), 236-244 (2005).

22. G. T. Jasion, T. D. Bradley, K. Harrington, H. Sakr, Y. Chen, E. N. Fokoua, I. A. Davidson, A. Taranta, J. R. Hayes, and D. J. Richardson, "Hollow core NANF with 0.28 dB/km attenuation in the C and L bands," in *Optical Fiber Communication Conference*(Optical Society of America), Th4B.4 (2020).

23. S. Liu, N. Liu, M. Hou, J. Guo, Z. Li, and P. Lu, "Direction-independent fiber inclinometer based on simplified hollow core photonic crystal fiber," Opt. Lett. **38**(4), 449-451 (2013).

24. G. Liu, Q. Sheng, W. Hou, and M. Han, "High-resolution, large dynamic range fiber-optic thermometer with cascaded Fabry-Perot cavities," Opt. Lett. **41**(21), 5134-5137 (2016).

25. K. Hill, Y. Fujii, D. C. Johnson, and B. Kawasaki, "Photosensitivity in optical fiber waveguides: Application to reflection filter fabrication," Appl. Phys. Lett. **32**(10), 647-649 (1978).

26. G. Meltz, W. W. Morey, and W. Glenn, "Formation of Bragg gratings in optical fibers by a transverse holographic method," Opt. Lett. **14**(15), 823-825 (1989).

27. Z. Liu, H.-Y. Tam, L. Htein, M.-L. V. Tse, and C. Lu, "Microstructured Optical Fiber Sensors," J. Lightwave Technol. **35**(16), 3425-3439 (2017).

28. T. Erdogan, "Fiber grating spectra," J. Lightwave Technol. **15**(8), 1277-1294 (1997).

29. R. Kashyap, *Fiber bragg gratings* (Academic press, 2009).

30. I. Abdulhalim, and C. Pannell, "Photoelastic in-fiber birefringence modulator operating at the fundamental transverse acoustic resonance," IEEE Photonics Technol. Lett. **5**(10), 1197-1199 (1993).

31. S. Magne, S. Rougeault, M. Vilela, and P. Ferdinand, "State-of-strain evaluation with fiber Bragg grating rosettes: application to discrimination between strain and temperature effects in fiber sensors," Appl. Opt. **36**(36), 9437-9447 (1997).

32. E. Li, "Temperature compensation of multimode-interference-based fiber devices," Opt. Lett. **32**(14), 2064-2066 (2007).

33. Y. Wang, H. Bartelt, W. Ecke, R. Willsch, J. Kobelke, M. Kautz, S. Brueckner, and M. Rothhardt, "Sensing properties of fiber Bragg gratings in small-core Ge-doped photonic crystal fibers," Opt. Commun. **282**(6), 1129-1134 (2009).

34. J. Kong, X. Ouyang, A. Zhou, H. Yu, and L. Yuan, "Pure Directional Bending Measurement With a Fiber Bragg Grating at the Connection Joint of Eccentric-Core and Single-Mode Fibers," J. Lightwave Technol. **34**(14), 3288-3292 (2016).

35. Y. Liu, A. Zhou, Q. Xia, Y. Zhao, H. Deng, S. Yang, and L. Yuan, "Quasi-Distributed Directional Bending Sensor Based on Fiber Bragg Gratings Array in Triangle-Four Core Fiber," IEEE Sens. J. **19**(22), 10728-10735 (2019).

36. M. Gander, W. MacPherson, R. McBride, J. Jones, L. Zhang, I. Bennion, P. Blanchard, J. Burnett, and A. Greenaway, "Bend measurement using Bragg gratings in multicore fibre," Electron. Lett. **36**(2), 120-121 (2000).

37. I. H. Malitson, "Interspecimen comparison of the refractive index of fused silica," Josa **55**(10), 1205-1209 (1965).

38. "Fused silica," https://en.wikipedia.org/wiki/Fused_quartz.

39. B. Eggleton, P. Westbrook, R. Windeler, S. Spälter, and T. Strasser, "Grating resonances in air–silica microstructured optical fibers," Opt. Lett. **24**(21), 1460-1462 (1999).

40. C. Martelli, J. Canning, N. Groothoff, and K. Lyytikainen, "Strain and temperature characterization of photonic crystal fiber Bragg gratings," Opt. Lett. **30**(14), 1785-1787 (2005).

41. O. Frazao, J. Carvalho, L. Ferreira, F. Araújo, and J. Santos, "Discrimination of strain and temperature using Bragg gratings in microstructured and standard optical fibres," Meas. Sci. Technol. **16**(10), 2109 (2005).

42. M. P. Huy, G. Laffont, Y. Frignac, V. Dewynter-Marty, P. Ferdinand, P. Roy, J.-M. Blondy, D. Pagnoux, W. Blanc, and B. Dussardier, "Fibre Bragg grating photowriting in microstructured optical fibres for refractive index measurement," Meas. Sci. Technol. **17**(5), 992 (2006).

43. M. C. P. Huy, G. Laffont, V. Dewynter, P. Ferdinand, P. Roy, J.-L. Auguste, D. Pagnoux, W. Blanc, and B. Dussardier, "Three-hole microstructured optical fiber for efficient fiber Bragg grating refractometer," Opt. Lett. **32**(16), 2390-2392 (2007).

44. N. Groothoff, J. Canning, E. Buckley, K. Lyttikainen, and J. Zagari, "Bragg gratings in air–silica structured fibers," Opt. Lett. **28**(4), 233-235 (2003).

45. C. M. Jewart, Q. Wang, J. Canning, D. Grobnic, S. J. Mihailov, and K. P. Chen, "Ultrafast femtosecond-laser-induced fiber Bragg gratings in air-hole microstructured fibers for high-temperature pressure sensing," Opt. Lett. **35**(9), 1443-1445 (2010).

46. D. Grobnic, C. W. Smelser, S. J. Mihailov, and R. B. Walker, "Long-term thermal stability tests at 1000° C of silica fibre Bragg gratings made with ultrafast laser radiation," Meas. Sci. Technol. **17**(5), 1009 (2006).

47. J. Y. Huang, J. Van Roosbroeck, J. Vlekken, A. B. Martinez, T. Geernaert, F. Berghmans, B. Van Hoe, E. Lindner, and C. Caucheteur, "FBGs written in specialty fiber for high pressure/high temperature measurement," Opt. Express **25**(15), 17936-17947 (2017).

48. C. M. Jewart, T. Chen, E. Lindner, J. Fiebrandt, M. Rothhardt, K. Schuster, J. Kobelke, H. Bartelt, and K. P. Chen, "Bending insensitivity of fiber Bragg gratings in suspended-core optical fibers," Opt. Lett. **36**(23), 4491-4493 (2011).

49. J. Thomas, C. Voigtländer, R. G. Becker, D. Richter, A. Tünnermann, and S. Nolte, "Femtosecond pulse written fiber gratings: a new avenue to integrated fiber technology," Laser Photonics Rev. **6**(6), 709-723 (2012).

50. S. W. James, and R. P. Tatam, "Optical fibre long-period grating sensors: characteristics and application," Meas. Sci. Technol. **14**(5), R49 (2003).

51. A. Taghipour, A. Rostami, M. Bahrami, H. Baghban, and M. Dolatyari, "Comparative study between LPFG- and FBG-based bending sensors," Opt. Commun. **312**99-105 (2014).

52. V. Bhatia, D. K. Campbell, D. Sherr, T. D'Alberto, N. Zabaronick, G. A. Ten Eyck, K. A. Murphy, and R. O. Claus, "Temperature-insensitive and strain-insensitive long-period grating sensors for smart structures," Opt. Eng. **36**(7), 1872-1877 (1997).

53. O. Duhem, J.-F. Henninot, M. Warenghem, and M. Douay, "Demonstration of long-period-grating efficient couplings with an external medium of a refractive index higher than that of silica," Appl. Opt. **37**(31), 7223-7228 (1998).

54. S. Khaliq, S. W. James, and R. P. Tatam, "Fiber-optic liquid-level sensor using a long-period grating," Opt. Lett. **26**(16), 1224-1226 (2001).

55. P. Westbrook, B. Eggleton, R. Windeler, A. Hale, T. Strasser, and G. Burdge, "Cladding-mode resonances in hybrid polymer-silica microstructured optical fiber gratings," IEEE Photonics Technol. Lett. **12**(5), 495-497 (2000).

56. Y.-G. Han, G. Kim, K. Lee, S. B. Lee, C. H. Jeong, C. H. Oh, and H. J. Kang, "Bending sensitivity of long-period fiber gratings inscribed in holey fibers depending on an axial rotation angle," Opt. Express **15**(20), 12866-12871 (2007).

57. J. Xu, Y.-g. Liu, Z. Wang, and B. Tai, "Simultaneous force and temperature measurement using long-period grating written on the joint of a microstructured optical fiber and a single mode fiber," Appl. Opt. **49**(3), 492-496 (2010).

58. Y. Zhu, P. Shum, H.-J. Chong, M. Rao, and C. Lu, "Strong resonance and a highly compact long-period grating in a large-mode-area photonic crystal fiber," Opt. Express **11**(16), 1900-1905 (2003).

59. Y. Zhu, P. Shum, H.-W. Bay, M. Yan, X. Yu, J. Hu, J. Hao, and C. Lu, "Strain-insensitive and high-temperature long-period gratings inscribed in photonic crystal fiber," Opt. Lett. **30**(4), 367-369 (2005).

60. H. Dobb, K. Kalli, and D. J. Webb, "Temperature-insensitive long period grating sensors in photonic crystal fibre," Electron. Lett. **40**(11), 657-658 (2004).

61. J. S. Petrovic, H. Dobb, V. K. Mezentsev, K. Kalli, D. J. Webb, and I. Bennion, "Sensitivity of LPGs in PCFs fabricated by an electric arc to temperature, strain, and external refractive index," J. Lightwave Technol. **25**(5), 1306-1312 (2007).

62. Y.-G. Han, S. Song, G. H. Kim, K. Lee, S. B. Lee, J. H. Lee, C. H. Jeong, C. H. Oh, and H. J. Kang, "Simultaneous independent measurement of strain and temperature based on long-period fiber gratings inscribed in holey fibers depending on air-hole size," Opt. Lett. **32**(15), 2245-2247 (2007).

63. L. Rindorf, and O. Bang, "Highly sensitive refractometer with a photonic-crystal-fiber long-period grating," Opt. Lett. **33**(6), 563-565 (2008).

64. N. Zhang, G. Humbert, Z. Wu, K. Li, P. P. Shum, N. M. Zhang, Y. Cui, J. L. Auguste, X. Q. Dinh, and L. Wei, "In-line optofluidic refractive index sensing

in a side-channel photonic crystal fiber," Opt. Express **24**(24), 27674-27682 (2016).

65. J. H. Lim, K. S. Lee, J. C. Kim, and B. H. Lee, "Tunable fiber gratings fabricated in photonic crystal fiber by use of mechanical pressure," Opt. Lett. **29**(4), 331-333 (2004).

66. W. Bock, J. Chen, P. Mikulic, T. Eftimov, and M. Korwin-Pawlowski, "Pressure sensing using periodically tapered long-period gratings written in photonic crystal fibres," Meas. Sci. Technol. **18**(10), 3098 (2007).

67. J. Sun, C. Chan, X. Dong, and P. Shum, "Application of an artificial neural network for simultaneous measurement of temperature and strain by using a photonic crystal fiber long-period grating," Meas. Sci. Technol. **18**(9), 2943 (2007).

68. C. Fabry, and A. Perot, "Theorie et applications d'une nouvelle methods de spectroscopie intereferentielle," Ann. Chim. Ser. 7 **16**115-144 (1899).

69. B. H. Lee, Y. H. Kim, K. S. Park, J. B. Eom, M. J. Kim, B. S. Rho, and H. Y. Choi, "Interferometric fiber optic sensors," Sensors **12**(3), 2467-2486 (2012).

70. C.-L. Lee, Y.-C. Zheng, C.-L. Ma, H.-J. Chang, and C.-F. Lee, "Dynamic micro-air-bubble drifted in a liquid core fiber Fabry-Pérot interferometer for directional fiber-optic level meter," Appl. Phys. Lett. **102**(19), 193504 (2013).

71. Y. Rao, T. Zhu, X. Yang, and D. Duan, "In-line fiber-optic etalon formed by hollow-core photonic crystal fiber," Opt. Lett. **32**(18), 2662-2664 (2007).

72. C. Wu, H. Fu, K. K. Qureshi, B.-O. Guan, and H.-Y. Tam, "High-pressure and high-temperature characteristics of a Fabry–Perot interferometer based on photonic crystal fiber," Opt. Lett. **36**(3), 412-414 (2011).

73. S. Aref, M. Zibaii, M. Kheiri, H. Porbeyram, H. Latifi, F. Araujo, L. Ferreira, J. Santos, J. Kobelke, and K. Schuster, "Pressure and temperature

characterization of two interferometric configurations based on suspended-core fibers," Opt. Commun. **285**(3), 269-273 (2012).

74. L. Jin, B.-O. Guan, and H. Wei, "Sensitivity characteristics of Fabry-Perot pressure sensors based on hollow-core microstructured fibers," J. Lightwave Technol. **31**(15), 2526-2532 (2013).

75. D. Jauregui-Vazquez, L. M. Morales-Villagomez, J. M. Estudillo-Ayala, D. Tiwari, M. Bianchetti, J. M. Sierra-Hernandez, J. C. Hernandez-Garcia, and R. Rojas-Laguna, "Determination of magnetic field using a Fabry–Perot cavity containing novel nanoparticles," Instrum. Sci. Technol. **45**(4), 392-403 (2017).

76. X. Liu, M. Jiang, Q. Sui, S. Luo, and X. Geng, "Optical fiber Fabry–Perot interferometer for microorganism growth detection," Opt. Fiber Technol. **30**, 32-37 (2016).

77. H. Yu, Z. Luo, Y. Zheng, J. Ma, Z. Li, and X. Jiang, "Temperature-Insensitive Vibration Sensor With Kagomé Hollow-Core Fiber Based Fabry–Perot Interferometer," J. Lightwave Technol. **37**(10), 2261-2269 (2019).

78. J. Villatoro, V. Finazzi, G. Coviello, and V. Pruneri, "Photonic-crystal-fiber-enabled micro-Fabry–Perot interferometer," Opt. Lett. **34**(16), 2441-2443 (2009).

79. C. Wu, Z. Liu, A. P. Zhang, B.-O. Guan, and H.-Y. Tam, "In-line open-cavity Fabry–Pérot interferometer formed by C-shaped fiber fortemperature-insensitive refractive index sensing," Opt. Express **22**(18), 21757-21766 (2014).

80. J. Tian, Z. Lu, M. Quan, Y. Jiao, and Y. Yao, "Fast response Fabry–Perot interferometer microfluidic refractive index fiber sensor based on concave-core photonic crystal fiber," Opt. Express **24**(18), 20132-20142 (2016).

81. R. Wang, and X. Qiao, "Intrinsic fabry-perot interferometeric sensor based on microfiber created by chemical etching," Sensors **14**(9), 16808-16815 (2014).

82. F. Yang, Y. Tan, W. Jin, Y. Lin, Y. Qi, and H. L. Ho, "Hollow-core fiber Fabry–Perot photothermal gas sensor," Opt. Lett. **41**(13), 3025-3028 (2016).

83. R. Wang, Z. Liu, and X. Qiao, "Fringe visibility enhanced Fabry-Perot interferometer and its application as gas refractometer," Sensor Actuat. B Chem. **234**, 498-502 (2016).

84. D. López-Torres, A. Lopez-Aldaba, C. E. Aguado, J.-L. Auguste, R. Jamier, P. Roy, M. López-Amo, and F. J. Arregui, "Sensitivity optimization of a microstructured optical fiber ammonia gas sensor by means of tuning the thickness of a metal oxide nano-coating," IEEE Sens. J. **19**(13), 4982-4991 (2019).

85. A. L. Aldaba, D. Lopez-Torres, C. Elosua, J.-L. Auguste, R. Jamier, P. Roy, F. J. Arregui, and M. López-Amo, "SnO2-MOF-Fabry-Perot optical sensor for relative humidity measurements," Sensor Actuat. B Chem. **257**, 189-199 (2018).

86. H. Y. Choi, K. S. Park, S. J. Park, U.-C. Paek, B. H. Lee, and E. S. Choi, "Miniature fiber-optic high temperature sensor based on a hybrid structured Fabry–Perot interferometer," Opt. Lett. **33**(21), 2455-2457 (2008).

87. G. Sagnac, "L'éther lumineux démontré par l'effet du vent relatif d'éther dans un interféromètre en rotation uniforme," CR Acad. Sci. **157**708-710 (1913).

88. V. Vali, and R. Shorthill, "Fiber ring interferometer," Appl. Opt. **15**(5), 1099-1100 (1976).

89. H. Fu, H. Tam, L.-Y. Shao, X. Dong, P. Wai, C. Lu, and S. K. Khijwania, "Pressure sensor realized with polarization-maintaining photonic crystal fiber-based Sagnac interferometer," Appl. Opt. **47**(15), 2835-2839 (2008).

90. D. S. Moon, B. H. Kim, A. Lin, G. Sun, Y.-G. Han, W.-T. Han, and Y. Chung, "The temperature sensitivity of Sagnac loop interferometer based on

polarization maintaining side-hole fiber," Opt. Express **15**(13), 7962-7967 (2007).

91. T. Han, Y.-g. Liu, Z. Wang, J. Guo, Z. Wu, S. Wang, Z. Li, and W. Zhou, "Unique characteristics of a selective-filling photonic crystal fiber Sagnac interferometer and its application as high sensitivity sensor," Opt. Express **21**(1), 122-128 (2013).

92. E. Reyes-Vera, C. M. Cordeiro, and P. Torres, "Highly sensitive temperature sensor using a Sagnac loop interferometer based on a side-hole photonic crystal fiber filled with metal," Appl. Opt. **56**(2), 156-162 (2017).

93. O. Frazao, J. Baptista, J. Santos, J. Kobelke, and K. Schuster, "Strain and temperature characterisation of sensing head based on suspended-core fibre in Sagnac interferometer," Electron. Lett. **44**(25), 1455-1456 (2008).

94. X. Dong, H. Y. Tam, and P. Shum, "Temperature-insensitive strain sensor with polarization-maintaining photonic crystal fiber based Sagnac interferometer," Appl. Phys. Lett. **90**(15), (2007).

95. Z. Liu, C. Wu, M.-L. V. Tse, and H.-Y. Tam, "Fabrication, characterization, and sensing applications of a high-birefringence suspended-core fiber," J. Lightwave Technol. **32**(11), 2113-2122 (2014).

96. Z. Liu, L. Htein, K.-K. Lee, K.-T. Lau, and H.-Y. Tam, "Large dynamic range pressure sensor based on two semicircle-holes microstructured fiber," Sci. Rep. **8**(1), 1-9 (2018).

97. O. Frazão, J. M. Baptista, J. L. Santos, and P. Roy, "Curvature sensor using a highly birefringent photonic crystal fiber with two asymmetric hole regions in a Sagnac interferometer," Appl. Opt. **47**(13), 2520-2523 (2008).

98. P. Zu, C. C. Chan, Y. Jin, Y. Zhang, and X. Dong, "Fabrication of a temperature-insensitive transverse mechanical load sensor by using a photonic crystal fiber-based Sagnac loop," Meas. Sci. Technol. **22**(2), 025204 (2011).

99. M. Bravo, A. Pinto, M. Lopez-Amo, J. Kobelke, and K. Schuster, "High precision micro-displacement fiber sensor through a suspended-core Sagnac interferometer," Opt. Lett. **37**(2), 202-204 (2012).

100. Y. Zhao, D. Wu, R.-Q. Lv, and J. Li, "Magnetic field measurement based on the Sagnac interferometer with a ferrofluid-filled high-birefringence photonic crystal fiber," IEEE Trans. Instrum. Meas. **65**(6), 1503-1507 (2016).

101. X. Li, L. V. Nguyen, Y. Zhao, H. Ebendorff-Heidepriem, and S. C. Warren-Smith, "High-sensitivity Sagnac-interferometer biosensor based on exposed core microstructured optical fiber," Sensor Actuat. B Chem. **269**, 103-109 (2018).

102. L. Zehnder, "Ein neuer interferenzrefraktor," (Springer, 1891).

103. L. Mach, "Ueber einen interferenzrefraktor," Zeitschrift für Instrumentenkunde **12**(3), 89 (1892).

104. R. M. Gerosa, D. H. Spadoti, L. d. S. Menezes, and C. J. de Matos, "In-fiber modal Mach-Zehnder interferometer based on the locally post-processed core of a photonic crystal fiber," Opt. Express **19**(4), 3124-3129 (2011).

105. M. Yang, D. Wang, Y. Wang, and C. Liao, "Fiber in-line Mach–Zehnder interferometer constructed by selective infiltration of two air holes in photonic crystal fiber," Opt. Lett. **36**(5), 636-638 (2011).

106. M. Deng, L. Liu, Y. Zhao, G. Yin, and T. Zhu, "Highly sensitive temperature sensor based on an ultra-compact Mach–Zehnder interferometer with side-opened channels," Opt. Lett. **42**(18), 3549-3552 (2017).

107. Y. Geng, X. Li, X. Tan, Y. Deng, and X. Hong, "Compact and ultrasensitive temperature sensor with a fully liquid-filled photonic crystal fiber Mach–Zehnder interferometer," IEEE Sens. J. **14**(1), 167-170 (2013).

108. H. Liang, W. Zhang, H. Wang, P. Geng, S. Zhang, S. Gao, C. Yang, and J. Li, "Fiber in-line Mach–Zehnder interferometer based on near-elliptical core photonic crystal fiber for temperature and strain sensing," Opt. Lett. **38**(20), 4019-4022 (2013).

109. B. Kim, T.-H. Kim, L. Cui, and Y. Chung, "Twin core photonic crystal fiber for in-line Mach-Zehnder interferometric sensing applications," Opt. Express **17**(18), 15502-15507 (2009).

110. L. Hu, C. Chan, X. Dong, Y. Wang, P. Zu, W. C. Wong, W. Qian, and T. Li, "Photonic crystal fiber strain sensor based on modified Mach–Zehnder interferometer," IEEE Photonics J. **4**(1), 114-118 (2011).

111. J. Zheng, P. Yan, Y. Yu, Z. Ou, J. Wang, X. Chen, and C. Du, "Temperature and index insensitive strain sensor based on a photonic crystal fiber in line Mach–Zehnder interferometer," Opt. Commun. **297**7-11 (2013).

112. X. Bai, D. Fan, S. Wang, S. Pu, and X. Zeng, "Strain sensor based on fiber ring cavity laser with photonic crystal fiber in-line Mach–Zehnder interferometer," IEEE Photonics J. **6**(4), 1-8 (2014).

113. W. C. Wong, W. Zhou, C. C. Chan, X. Dong, and K. C. Leong, "Cavity ringdown refractive index sensor using photonic crystal fiber interferometer," Sensor Actuat. B Chem. **161**(1), 108-113 (2012).

114. I. Shavrin, S. Novotny, A. Shevchenko, and H. Ludvigsen, "Gas refractometry using a hollow-core photonic bandgap fiber in a Mach-Zehnder-type interferometer," Appl. Phys. Lett. **100**(5), 051106 (2012).

115. N. L. Andrews, R. Ross, D. Munzke, C. van Hoorn, A. Brzezinski, J. A. Barnes, O. Reich, and H. P. Loock, "In-fiber Mach-Zehnder interferometer for gas refractive index measurements based on a hollow-core photonic crystal fiber," Opt. Express **24**(13), 14086-14099 (2016).

116. V. P. Minkovich, D. Monzón-Hernández, J. Villatoro, and G. Badenes, "Microstructured optical fiber coated with thin films for gas and chemical sensing," Opt. Express **14**(18), 8413-8418 (2006).

117. L. V. Nguyen, K. Hill, S. Warren-Smith, and T. Monro, "Interferometric-type optical biosensor based on exposed core microstructured optical fiber," Sensor Actuat. B Chem. **221**, 320-327 (2015).

118. O. Frazão, S. Silva, J. Viegas, J. M. Baptista, J. L. Santos, J. Kobelke, and K. Schuster, "All fiber Mach–Zehnder interferometer based on suspended twin-core fiber," IEEE Photonics Technol. Lett. **22**(17), 1300-1302 (2010).

119. L. Sójka, L. Pajewski, M. Śliwa, P. Mergo, T. Benson, S. Sujecki, and E. Bereś-Pawlik, "Multicore microstructured optical fibre for sensing applications," Opt. Commun. **344**71-76 (2015).

120. M. Deng, C.-P. Tang, T. Zhu, and Y.-J. Rao, "Highly sensitive bend sensor based on Mach–Zehnder interferometer using photonic crystal fiber," Opt. Commun. **284**(12), 2849-2853 (2011).

121. W. Shin, Y. L. Lee, B.-A. Yu, Y.-C. Noh, and T. J. Ahn, "Highly sensitive strain and bending sensor based on in-line fiber Mach–Zehnder interferometer in solid core large mode area photonic crystal fiber," Opt. Commun. **283**(10), 2097-2101 (2010).

122. J. Wang, F. Ai, Q. Sun, T. Liu, H. Li, Z. Yan, and D. Liu, "Diaphragm-based optical fiber sensor array for multipoint acoustic detection," Opt. Express **26**(19), 25293-25304 (2018).

123. N. M. Y. Zhang, K. Li, T. Zhang, P. Shum, Z. Wang, Z. Wang, N. Zhang, J. Zhang, T. Wu, and L. Wei, "Electron-rich two-dimensional molybdenum trioxides for highly integrated plasmonic biosensing," ACS Photonics **5**(2), 347-352 (2018).

124. K. Li, N. Zhang, N. M. Y. Zhang, G. Liu, T. Zhang, and L. Wei, "Ultrasensitive measurement of gas refractive index using an optical nanofiber coupler," Opt. Lett. **43**(4), 679-682 (2018).

125. N. Zhang, G. Humbert, T. Gong, P. P. Shum, K. Li, J.-L. Auguste, Z. Wu, D. J. J. Hu, F. Luan, Q. X. Dinh, M. Olivo, and L. Wei, "Side-channel photonic crystal fiber for surface enhanced Raman scattering sensing," Sensor Actuat. B Chem. **223**, 195-201 (2016).

126. B. Shuai, L. Xia, and D. Liu, "Coexistence of positive and negative refractive index sensitivity in the liquid-core photonic crystal fiber based plasmonic sensor," Opt. Express **20**(23), 25858-25866 (2012).

127. S. Zhang, W. Zhang, S. Gao, P. Geng, and X. Xue, "Fiber-optic bending vector sensor based on Mach–Zehnder interferometer exploiting lateral-offset and up-taper," Opt. Lett. **37**(21), 4480-4482 (2012).

128. W. Cui, J. Si, T. Chen, and X. Hou, "Compact bending sensor based on a fiber Bragg grating in an abrupt biconical taper," Opt. Express **23**(9), 11031-11036 (2015).

129. K. Ni, T. Li, L. Hu, W. Qian, Q. Zhang, and S. Jin, "Temperature-independent curvature sensor based on tapered photonic crystal fiber interferometer," Opt. Commun. **285**(24), 5148-5150 (2012).

130. Y. Wang, D. Richardson, G. Brambilla, X. Feng, M. Petrovich, M. Ding, and Z. Song, "Intensity measurement bend sensors based on periodically tapered soft glass fibers," Opt. Lett. **36**(4), 558-560 (2011).

131. S. Dass, and R. Jha, "Microfiber-Wrapped Bi-Conical-Tapered SMF for Curvature Sensing," IEEE Sens. J. **16**(10), 3649-3652 (2016).

132. J. N. Dash, S. Dass, and R. Jha, "Photonic crystal fiber microcavity based bend and temperature sensor using micro fiber," Sensor Actuat. A Phys. **244**, 24-29 (2016).

133. G. Flockhart, W. MacPherson, J. Barton, J. Jones, L. Zhang, and I. Bennion, "Two-axis bend measurement with Bragg gratings in multicore optical fiber," Opt. Lett. **28**(6), 387-389 (2003).

134. P. Saffari, T. Allsop, A. Adebayo, D. Webb, R. Haynes, and M. M. Roth, "Long period grating in multicore optical fiber: an ultra-sensitive vector bending sensor for low curvatures," Opt. Lett. **39**(12), 3508-3511 (2014).

135. J. Kong, A. Zhou, C. Cheng, J. Yang, and L. Yuan, "Two-Axis Bending Sensor Based on Cascaded Eccentric Core Fiber Bragg Gratings," IEEE Photonics Technol. Lett. **28**(11), 1237-1240 (2016).

136. H. J. Patrick, "Self-aligning bipolar bend transducer based on long period grating written in eccentric core fibre," Electron. Lett. **36**(21), 1763-1764 (2000).

137. X. Chen, C. Zhang, D. J. Webb, K. Kalli, and G.-D. Peng, "Highly Sensitive Bend Sensor Based on Bragg Grating in Eccentric Core Polymer Fiber," IEEE Photonics Technol. Lett. **22**(11), 850-852 (2010).

138. X. Chen, C. Zhang, D. J. Webb, G. D. Peng, and K. Kalli, "Bragg grating in a polymer optical fibre for strain, bend and temperature sensing," Meas. Sci. Technol. **21**(9), (2010).

139. J. Villatoro, V. P. Minkovich, and J. Zubia, "Photonic crystal fiber interferometric vector bending sensor," Opt. Lett. **40**(13), 3113-3116 (2015).

140. H. Zhang, Z. Wu, P. P. Shum, R. Wang, X. Q. Dinh, S. Fu, W. Tong, and M. Tang, "Fiber Bragg gratings in heterogeneous multicore fiber for directional bending sensing," J. Opt. **18**(8), 085705 (2016).

141. A. Grillet, D. Kinet, J. Witt, M. Schukar, K. Krebber, F. Pirotte, and A. Depre, "Optical Fiber Sensors Embedded Into Medical Textiles for Healthcare Monitoring," IEEE Sens. J. **8**(7), 1215-1222 (2008).

142. C. Zhan, Y. Zhu, S. Yin, and P. Ruffin, "Multi-parameter harsh environment sensing using asymmetric Bragg gratings inscribed by IR femtosecond irradiation," Opt. Fiber Technol. **13**(2), 98-107 (2007).

143. R. T. Schermer, and J. H. Cole, "Improved Bend Loss Formula Verified for Optical Fiber by Simulation and Experiment," IEEE J. Quantum Electron. **43**(10), 899-909 (2007).

144. J. Su, X. Dong, and C. Lu, "Characteristics of Few Mode Fiber Under Bending," IEEE J. Sel. Top. Quant. **22**(2), 139-145 (2016).

145. M. H. Frosz, P. Roth, M. C. Günendi, and P. S. J. Russell, "Analytical formulation for the bend loss in single-ring hollow-core photonic crystal fibers," Photonics Res. **5**(2), (2017).

146. Z. Wu, Y. G. Liu, Z. Wang, M. Jiang, W. Ji, T. Han, S. Li, X. Shao, X. Q. Dinh, S. C. Tjin, and P. P. Shum, "Simultaneous measurement of curvature and strain based on fiber Bragg grating in two-dimensional waveguide array fiber," Opt. Lett. **38**(20), 4070-4073 (2013).

147. K. Markowski, K. Jedrzejewski, M. Marzecki, and T. Osuch, "Linearly chirped tapered fiber-Bragg-grating-based Fabry-Perot cavity and its application in simultaneous strain and temperature measurement," Opt. Lett. **42**(7), 1464-1467 (2017).

148. Y. Wang, L. Xiao, D. Wang, and W. Jin, "Highly sensitive long-period fiber-grating strain sensor with low temperature sensitivity," Opt. Lett. **31**(23), 3414-3416 (2006).

149. Y. Wang, W. Jin, J. Ju, H. Xuan, H. L. Ho, L. Xiao, and D. Wang, "Long period gratings in air-core photonic bandgap fibers," Opt. Express **16**(4), 2784-2790 (2008).

150. G. K. Costa, P. M. Gouvea, L. M. Soares, J. M. Pereira, F. Favero, A. M. Braga, P. Palffy-Muhoray, A. C. Bruno, and I. C. Carvalho, "In-fiber Fabry-Perot

interferometer for strain and magnetic field sensing," Opt. Express **24**(13), 14690-14696 (2016).

151. P. Zhang, M. Tang, F. Gao, B. Zhu, S. Fu, J. Ouyang, P. P. Shum, and D. Liu, "Cascaded fiber-optic Fabry-Perot interferometers with Vernier effect for highly sensitive measurement of axial strain and magnetic field," Opt. Express **22**(16), 19581-19588 (2014).

152. Y. Zheng, P. P. Shum, Y. Luo, Y. Zhang, W. Ni, G. Wang, Z. Wu, X. Q. Dinh, J. L. Auguste, and G. Humbert, "High-resolution, large-dynamic-range multimode interferometer sensor based on a suspended-core microstructured optical fiber," Opt. Lett. **45**(4), 1017-1020 (2020).

153. H. Zhang, Z. Wu, P. P. Shum, X. Q. Dinh, C. W. Low, Z. Xu, R. Wang, X. Shao, S. Fu, and W. Tong, "Highly sensitive strain sensor based on helical structure combined with Mach-Zehnder interferometer in multicore fiber," Sci. Rep. **7**46633 (2017).

154. J. C. Shin, W. G. Kwak, and Y.-G. Han, "Temperature-Insensitive Microfiber Mach–Zehnder Interferometer for Absolute Strain Measurement," J. Lightwave Technol. **34**(19), 4579-4583 (2016).

155. C. Zhang, T. Ning, J. Li, J. Zheng, X. Gao, and L. Pei, "Refractive index and strain sensor based on twin-core fiber with a novel T-shaped taper," Opt. Laser Technol. **102**, 12-16 (2018).

156. P. Lu, L. Men, K. Sooley, and Q. Chen, "Tapered fiber Mach–Zehnder interferometer for simultaneous measurement of refractive index and temperature," Appl. Phys. Lett. **94**(13), (2009).

157. C. Liao, D. Wang, and Y. Wang, "Microfiber in-line Mach–Zehnder interferometer for strain sensing," Opt. Lett. **38**(5), 757-759 (2013).

158. L. Jiang, J. Yang, S. Wang, B. Li, and M. Wang, "Fiber Mach–Zehnder interferometer based on microcavities for high-temperature sensing with high sensitivity," Opt. Lett. **36**(19), 3753-3755 (2011).

159. L. Li, L. Xia, Z. Xie, and D. Liu, "All-fiber Mach-Zehnder interferometers for sensing applications," Opt. Express **20**(10), 11109-11120 (2012).

160. Y. Zheng, P. P. Shum, S. Liu, B. Li, Y. Xiang, Y. Luo, Y. Zhang, W. Ni, Z. Wu, and X. Q. Dinh, "Experimental and numerical investigation on hollow core photonic crystal fiber based bending sensor," Opt. Express **27**(21), 30629-30638 (2019).

161. B. S. Shariat, Y. Liu, and G. Rio, "Mathematical modelling of pseudoelastic behaviour of tapered NiTi bars," J. Alloys Compd. **577**, S76-S82 (2013).

162. T. W. Hughes, M. Minkov, Y. Shi, and S. Fan, "Training of photonic neural networks through in situ backpropagation and gradient measurement," Optica **5**(7), (2018).

163. K. Tian, G. Farrell, X. Wang, W. Yang, Y. Xin, H. Liang, E. Lewis, and P. Wang, "Strain sensor based on gourd-shaped single-mode-multimode-single-mode hybrid optical fibre structure," Opt. Express **25**(16), 18885-18896 (2017).

164. W. W. Li, and D. N. Wang, "Femtosecond laser inscribed straight waveguide in no-core fiber for in-line Mach-Zehnder interferometer construction," Opt. Lett. **43**(14), 3405-3408 (2018).

165. C. Zhang, T. Ning, J. Zheng, J. Xu, X. Gao, H. Lin, J. Li, and L. Pei, "An optical fiber strain sensor by using of taper based TCF structure," Opt. Laser Technol. **120**, 105687 (2019).

166. S. Marrujo-Garcia, I. Hernandez-Romano, M. Torres-Cisneros, D. A. May-Arrioja, V. P. Minkovich, and D. Monzon-Hernandez, "Temperature-independent curvature sensor based on in-fiber Mach-Zehnder interferometer using hollow-core fiber," J. Lightwave Technol. **38**(15), 4166-4173 (2020).

167. Y. Zheng, Z. Wu, P. Ping Shum, Z. Xu, G. Keiser, G. Humbert, H. Zhang, S. Zeng, and X. Quyen Dinh, "Sensing and lasing applications of whispering gallery mode microresonators," Opto-Electron. Adv. **1**(9), 180015 (2018).

168. H. Luo, Q. Sun, X. Li, Z. Yan, Y. Li, D. Liu, and L. Zhang, "Refractive index sensitivity characteristics near the dispersion turning point of the multimode microfiber-based Mach-Zehnder interferometer," Opt. Lett. **40**(21), 5042-5045 (2015).

169. Q. Liu, T. Tokunaga, and Z. He, "Ultra-high-resolution large-dynamic-range optical fiber static strain sensor using Pound–Drever–Hall technique," Opt. Lett. **36**(20), 4044-4046 (2011).

170. Y. Zhu, P. Shum, X. Chen, C.-H. Tan, and C. Lu, "Resonance-temperature-insensitive phase-shifted long-period fiber gratings induced by surface deformation with anomalous strain characteristics," Opt. Lett. **30**(14), 1788-1790 (2005).

171. T. H. Chan, L. Yu, H.-Y. Tam, Y.-Q. Ni, S. Liu, W. Chung, and L. Cheng, "Fiber Bragg grating sensors for structural health monitoring of Tsing Ma bridge: Background and experimental observation," Eng. Struct. **28**(5), 648-659 (2006).

172. J. Chen, Q. Liu, X. Fan, and Z. He, "Ultrahigh resolution optical fiber strain sensor using dual Pound-Drever-Hall feedback loops," Opt. Lett. **41**(5), 1066-1069 (2016).

173. M. Grabk, B. Wajnchold, S. Pustelny, W. Gawlik, K. Skorupski, and P. Mergo, "Experimental and Theoretical Study of Light Propagation in Suspended-Core Optical Fiber," Acta Phys. Pol. A, **118**(6), (2010).

174. G. Liu, M. Han, and W. Hou, "High-resolution and fast-response fiber-optic temperature sensor using silicon Fabry-Pérot cavity," Opt. Express **23**(6), 7237-7247 (2015).

175. B. Dong, J. Hao, C. Y. Liaw, B. Lin, and S. C. Tjin, "Simultaneous strain and temperature measurement using a compact photonic crystal fiber inter-modal interferometer and a fiber Bragg grating," Appl. Opt. **49**(32), 6232-6235 (2010).

176. D. P. Zhou, L. Wei, W. K. Liu, and J. W. Y. Lit, "Simultaneous measurement of strain and temperature based on a fiber Bragg grating combined with a high-birefringence fiber loop mirror," Opt. Commun. **281**(18), 4640-4643 (2008).

177. D. P. Zhou, L. Wei, W. K. Liu, Y. Liu, and J. W. Lit, "Simultaneous measurement for strain and temperature using fiber Bragg gratings and multimode fibers," Appl. Opt. **47**(10), 1668-1672 (2008).